Extremely Low Cycle Fatigue Assessment of Corner Crack in Concrete-Filled Steel Piers with Box Section

A dissertation submitted to the Graduate School of Engineering of
Nagoya University
in partial fulfillment of the requirements for
the Degree of Doctor of Engineering

By
PARK　Jineun
July 2014

ACKNOWLEDGEMENTS

ABSTRACT

After the Hyogo-ken Nanbu earthquake, concrete-filled steel bridge piers were often used to prevent local buckling and to improve seismic performance of existing steel bridge piers. The concrete-filled steel piers have high ductility and load carrying capacity due to confinement of filling concrete. Therefore, the concrete-filled steel piers are able to show certain resistance against large cyclic plastic deformations. When the piers endure the large cyclic plastic deformation, low cycle fatigue damage will become a key issue. This dissertation develops the extremely low cycle fatigue assessment method of concrete-filled steel piers with box section through several fatigue tests and elasto-plastic finite element analyses.

In the first part of the work, extremely low cycle behavior of the steel pier in which concrete was filled for retrofitting against local buckling was investigated experimentally. Besides, strain behaviors around the cracking sites in the pier were obtained by elasto-plastic finite element analyses. It was revealed that the low cycle fatigue crack from the corner weld is one of the main failure modes of concrete-filled steel piers with box section.

As the second part of the work, low cycle fatigue tests were conducted on small-scale corner welded joints with single bevel groove welding. The test results indicated that the low cycle fatigue strength of the corner welded joints strongly depends on the weld root size. Then, the fatigue strength of the corner joints was evaluated based on the effective notch strain at the weld root tip which was calculated by elasto-plastic finite element analyses. A unique relationship between the effective notch strain and the fatigue life of the joint was observed regardless of the weld root size. And the fatigue strength curve for corner welded joints was proposed based on the relationship.

In the final part of the work, the applicability of the proposed method to concrete-filled steel piers was confirmed. The effective notch strain was calculated by finite element analyses with sub-modeling technique. By comparing the effective notch strain to the proposed fatigue strengths curve, cumulative damage indexes were calculated.

The predicted fatigue lives by the method show relatively conservative results compared with the experiment. However, the proposed assessment method can give relatively accurate predictions of fatigue life of concrete-filled steel piers in the extremely low cycle fatigue region. In order to reduce the difference of fatigue lives between the prediction and the experiment, new fatigue strength curve was suggested by considering crack propagation. As a result, it was revealed that the fatigue lives of the specimens can be predicted more accurately by considering the crack propagation into the proposed method.

TABLE OF CONTENT

LIST OF TABLES

LIST OF FIGURES

CHAPTER 1

INTRODUCTION

1.1 Background

Steel bridge piers are widely used for elevated highways and flyover bridges mainly in urban areas, because of their small cross sectional areas. During the Hyogo-ken Nanbu earthquake in 1995, two types of failure modes were observed in steel bridge piers; one is local buckling and the other is brittle fracture triggered by low cycle fatigue (Usami, 2006). Photographs shown in **Fig. 1.1** are typical failure modes in steel bridge piers observed in the earthquake (Miki, 1996). **Fig 1.1(a)** shows an example of the local buckling on flange and web plates in a steel pier with box section. **Fig 1.1(b)** shows a steel bridge pier that was completely ruptured by cracks of corner welds due to local buckling. **Fig 1.1(c), (d)** show low cycle fatigue failures were observed in welded joints of steel piers, such as a connection between beam and column and also triangular ribs on base joint.

Fig 1.2 shows the comparison of velocity profile about the Iwate-Miyagi Nairiku earthquake, the Miyagi earthquake and the Tohoku earthquake (Japan Society of Civil Engineers, 2012). In the Tohoku earthquake in 2011, it was revealed that extremely strong shaking persists over a long time in plate borderline type earthquake. It means that during the huge earthquakes, such as the Tokai, Tonankai and Nankai earthquake, the low cycle fatigue will become more of a possible damage in steel bridge piers because the long-duration seismic waves originates a large number of cyclic plastic deformations at the pier.
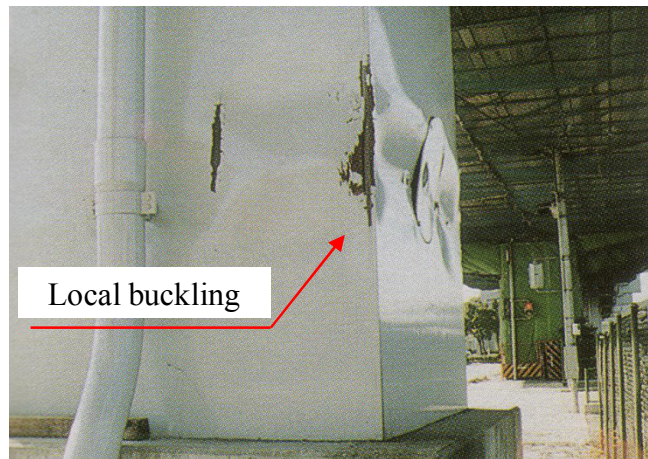
a) Flange and web plates

b) Ruptured steel bridge pier by cracks of corner weld
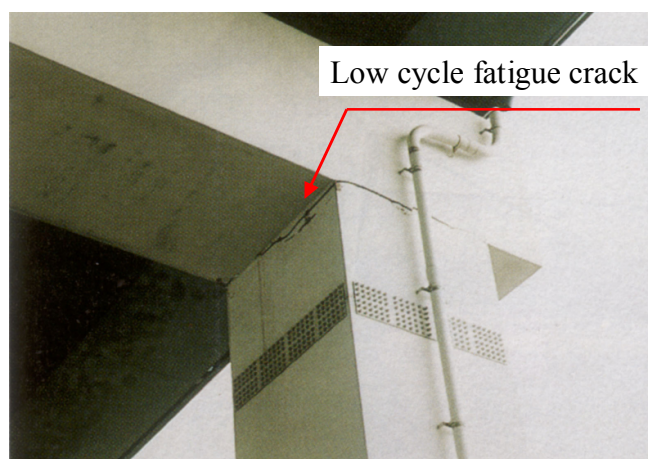
c) Beam-to-column connection

Fig. 1.1 Typical failure modes on steel bridge piers in the Hyogo-ken Nanbu earthquake
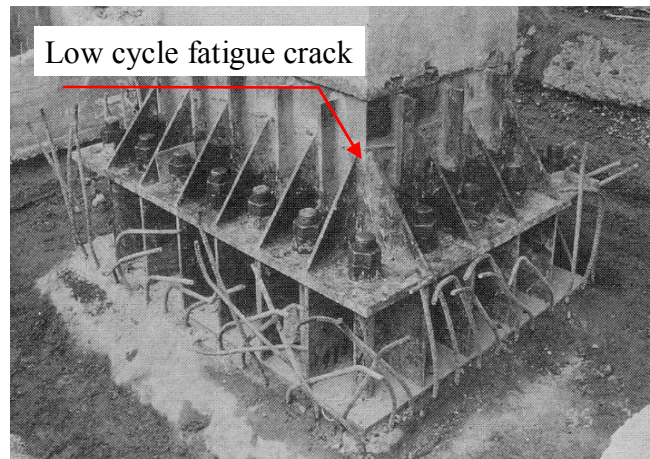
d) Base joints of steel bridge pier

Fig. 1.1 Typical failure modes on steel bridge piers in the Hyogo-ken Nanbu earthquake
(Continued)
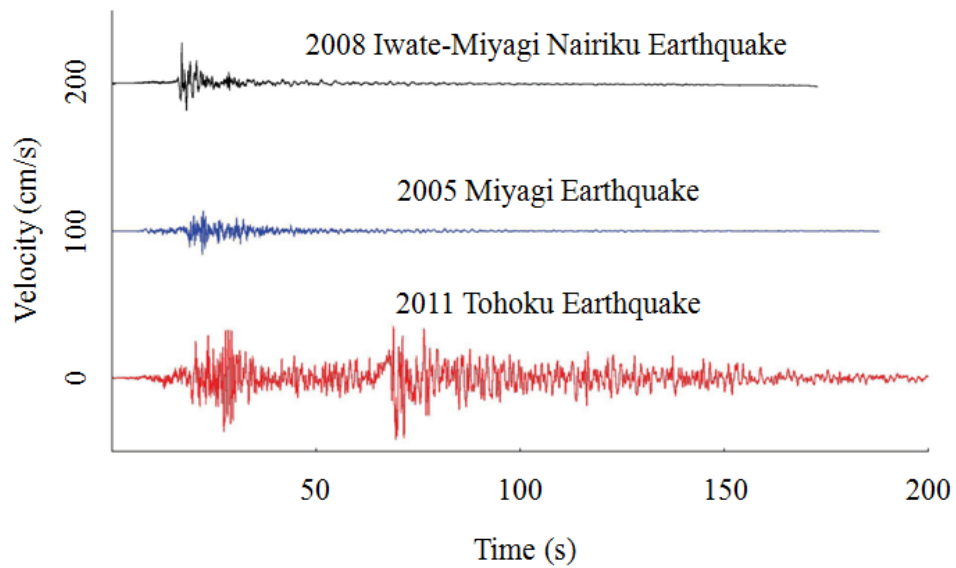
Fig. 1.2 Comparison of velocity profile about the Iwate-Miyagi Nairiku earthquake,
Miyagi earthquake and Tohoku earthquake (East-West direction)

The low cycle fatigue failure had been hardly reported in actual steel bridges before the Hyogo-ken Nanbu earthquake. The low cycle fatigue is caused by cyclic plastic deformation and its number of cycles to failure is relatively small. During earthquake on the steel bridge piers, the number of cycles corresponds to a fatigue life less than tens of cycles. In this study, the fatigue region is especially called "extremely low cycle fatigue region" to distinguish from the conventional low cycle fatigue region, corresponding to a fatigue life of more than hundreds cycles. Research on the extremely low cycle fatigue for steel piers is limited and design guidelines have not been established yet. Therefore, it is important to investigate the seismic performance of steel bridge piers from viewpoint of extremely low cycle fatigue.

On the other hands, a lot of research have been conducted on the local buckling, leading up to the guidelines for seismic design of steel bridges (Usami, 2005). Furthermore, a series of research on local buckling have been conducted to prevent the occurrence in existing steel piers, and then proposed several seismic retrofitting methods, such as filling steel piers with concrete and thickening of flange and web plates. The concrete-filled steel piers have high deformation capacity and load carrying capacity. Therefore, the concrete-filled steel piers can resist large cyclic plastic deformation. Meanwhile, when large plastic deformation repeatedly occurs in the pier, low cycle fatigue will become a key issue.

Furthermore, as mentioned above, cracks in corner weld are serious problem which can lead completely rupture in steel bridge piers. For preventing the failures of corner welds, especially, current design code (Japan Road Association, 2012) has recommended a welding method with enough penetration in corner joints. However, in the existing steel piers retrofitted against local buckling by such as filling with concrete, relatively large weld root face still remains in the corner joints. In these steel piers, there is a possibility that extremely low cycle fatigue cracks will occur in corner welds which may cause collapse of piers. For these reasons, the objective of this research is to develop the extremely low cycle fatigue assessment method of corner crack in concrete-filled steel piers.

1.2 Previous research

1.2.1 General remark on low cycle fatigue

Generally, low cycle fatigue is caused by a relatively small number of cycles and accompanied by significant amounts of plastic deformation, whereas high cycle fatigue is associated with relatively small deformations that are primarily elastic. Where the stress is high enough for plastic deformation to occur, the accounting of the loading in terms of stress is less useful and the strain in material offers a simpler and more accurate description.

Researching independently on thermal fatigue problem, Manson (1953) and Coffin (1954) proposed the relationship between plastic strain amplitude and fatigue life, so-called the "Manson-Coffin's law";

$$\varepsilon \cdot N^k = C \qquad (1\text{-}1)$$

where ε is the plastic strain amplitude, N is the number of cycles to failure, k is an empirical constant known as the fatigue ductility exponent, and C is a proportionality factor.

The relationship has been applied to a variety of fields, such as materials (Wong et al., 2001), turbine (Michael et al., 1990), ship industry (Urm et al., 2004) and pipelines (Zhong et al., 2005) etc.

On the other hand, several other attempts have also been conducted using the relationship between the dissipation energy and the number of cycles in steel components (Park et al., 2004), and also using the formulation and calibration of damage index (Usami et al., 1996). However, for the behavior of cracking site on low cycle fatigue, any research has not been addressed.

Recently, total strain amplitude was used by Mander et al. (1994), Liu et al. (2005a, 2005b) and Tateishi et al. (2005, 2007), as one variant instead of plastic strain amplitude in the Manson-Coffin's law.

1.2.2 Low cycle fatigue of steel structures

A lot of research on low cycle fatigue has been conducted for plain material in the fields of the marine and the mechanical engineering for years. The experiences in the Hyogo-ken Nanbu earthquake, however, revealed that almost all the low cycle fatigue damages in civil steel structures initiated from welded joints. Therefore, the low cycle fatigue strength of welded joints as well as plain material should be investigated.

Intensity studies have been conducted on coupon tests of different steel materials. Conventional low cycle fatigue tests commonly uses an hourglass shaped specimen in order to avoid the bucking of the specimen and are performed by controlling the axial strain in the specimen. Most of previous tests have been conducted with the hourglass specimen cut out from a steel plate and obtained the low cycle fatigue strengths according to the Manson-Coffin's equation. (Iida, 1968; Nishimura et al., 1978; Shimada et al., 1987; Komotori et al., 1991; Nakajima et al., 2000; Masatoshi, 2001).

Some researchers (Iida, 1973; Miki et al., 1981) carried out low cycle fatigue tests on notched specimens. They found that the fatigue strength of the specimens can be evaluated by strains at a notch root where cracks occurred.

Mander et al. (1994) investigated low cycle fatigue behavior of reinforcing steel. They used total strain amplitude, which can be resolved into elastic and plastic components, instead of plastic strain alone.

Liu et al. (2005a, 2005b) conducted studies on behaviors of low cycle fatigue of A36 square and rectangular steel bars under bending loadings. It was observed that using the test results of constant cyclic loading to predict the low cycle fatigue strength under random bending loadings may introduce large error. They found that using the test results of a damage accumulation index formula is more appropriate.

It is difficult to apply hourglass shaped specimens to low cycle fatigue tests for welded portion. Some other tests have been performed by Kaneta et al. (1982) and Machida et al. (1991), in which, instead of hourglass shaped specimens, round bar specimens cut out from welded joints were used. It was found that weld deposit metal

had lower fatigue strength than base metal. The strain level tested in their researches, however, was relatively low because buckling problem was unavoidable in the case that the round bar specimen was used.

Tateishi and Hanji (2004, 2007) developed the image measurement based fatigue testing system to investigate extremely low cycle fatigue strength of welded portion and obtained extremely low cycle fatigue strength curves of base metal, weld deposit and heat affected zone.

Recently, with the development of numerical analysis technique, some fatigue assessment methodologies have been proposed which are based on the local strain at cracking site regions where the strain is most severe.

Sakano et al. (2001) carried out extremely low cycle fatigue tests on beam-to-column and column-to-base connections in steel piers to investigate the influence of fillet at web-corner in the beam-to-column connection and triangular ribs of the base connection. Elasto-plastic finite element analyses were employed to calculate the local strain of the crack initiation point. It was demonstrated that the cycle fatigue crack initiation life of both beam-to-column and column-to-base connections in steel piers could be estimated by the Manson-Coffin's law.

Hanji et al. (2006) conducted extremely low cycle fatigue tests on T-shaped welded joints, where fatigue cracks were initiated from a weld toe. Local strain at the cracking point was analyzed by elasto-plastic finite element method. It was revealed that the local strain at the cracking point can be used to evaluate the fatigue strength of the welded joints with weld toe cracks.

Chen (2007) investigated the extremely low cycle fatigue failure of thick-walled steel piers through numerical analysis with complementary tests, and then proposed a strain approach assessment methodology for the thick-walled piers.

Hanji et al. (2011) demonstrated that the fatigue strength of load-carrying cruciform welded joints with root cracks can be evaluated by the local strain with effective notch concept regardless of weld root size and main plate thickness.

1.2.3 Seismic behavior of concrete-filled steel piers

The seismic behavior of steel bridge piers has been investigated by mainly using quasi-static cyclic loading and pseudo-dynamic loading tests. Most of these tests were conducted under cyclic lateral loading with constant axial force.

Ge et al. (1994) investigated ductility of concrete-filled steel piers with box section under cyclic loading. Eleven unstiffened and stiffened box columns specimens were tested under constant compressive axial loads and cyclic lateral loads. The test results were evaluated using both energy-absorption capacity and a newly defined ductility factor. In some of the test specimens, low cycle fatigue failures were observed.

Iura et al. (2001) conducted a study to investigate elasto-plastic behavior on fourteen concrete-filled steel tubular pier specimens, using some parameters such as radius and thickness of test specimens, concrete strength, concrete height, and position of diaphragms and loading conditions. They found that the position of the local buckling depended on the concrete height.

Some researchers (Sakino and Tomii, 1981; Nakahara et al., 2003; Xiao et al., 2004) also investigated the seismic behavior of concrete-filled steel pier, experimentally. However, all of researches focused on the cyclic behavior of concrete-filled steel pier, without considering the effects of amplitude and the number of cycles on damage accumulation.

Zhang et al. (2009) conducted a study to develop a cumulative damage model for concrete-filled steel piers with circular section subjected to simulated earthquake loading. The low cycle fatigue behaviors of the concrete-filled steel piers were investigated and a relationship between fatigue life and normalized displacement amplitude was established. They found that useful fatigue life expressions for application in damage-based seismic design are developed and used to predict the damage index for additional concrete-filled steel piers based on the experimental data.

On the other hands, analytical researches of concrete-filled steel pier are mostly based on the composite beam theory (Hajjar et al., 1998; Susantha et al., 2002; Varma et al.,

2002). These are the so-called "moment-curvature models". The analytical models based on the beam theory cannot directly take into account the cyclic buckling behavior of steel pier, the interface action between internal concrete and steel pier, and the confinement of internal concrete.

Goto et al (2009, 2010, and 2012) developed the nonlinear finite element analysis method for cyclic behavior of thin-walled circular and thin-walled stiffened rectangular steel piers with in-filled concrete. Based on the results of tests, the hysteretic behaviors of the concrete-filled steel piers were numerically simulated. The hysteresis loop, as shown in **Fig. 1.3**, shows the tendency of stiffness degradation and stiffness recovery in the cyclic loading process, so-called "pinching hysteresis loop". Moreover, the behavior of the concrete-filled steel pier was expressed by the concrete damaged plastic model combined with the discrete crack model. The accuracy of the proposed FE model was confirmed by the test results.
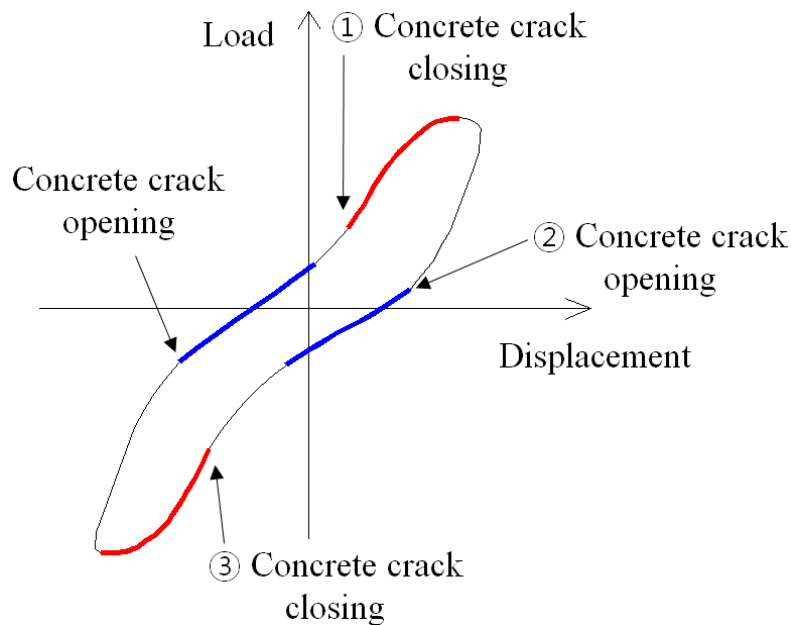
a) Horizontal force - horizontal displacement relation

Fig. 1.3 Typical pinching behavior of concrete steel piers (Goto, 2012)
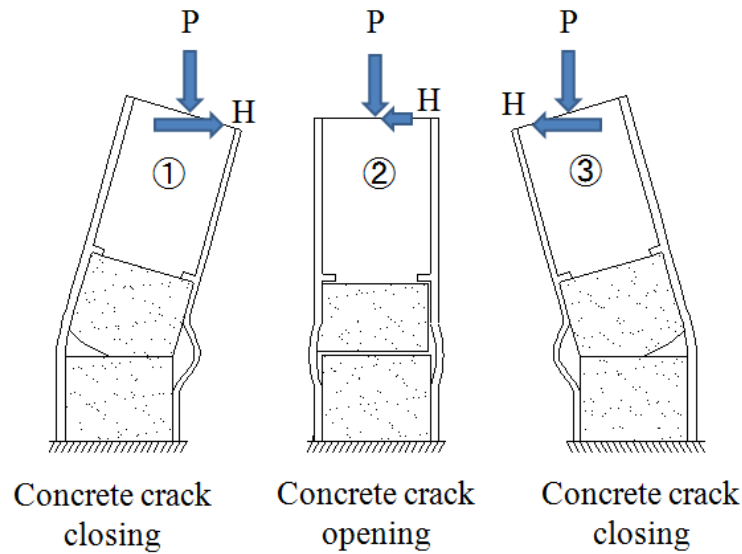
b) Verified mechanism of concrete-filled steel piers under cyclic loading

Fig. 1.3 Typical pinching behavior of concrete steel piers (Goto, 2012) (Continued)

1.2.4 Discussions

Extensive research has been conducted on the low cycle fatigue in structural material and welded joints. However, there are still remained several important issues that must be solved. Some comments and discussions are as follows;

1. Extremely low cycle fatigue behaviors of concrete-filled steel piers

Concrete-filled steel piers are often used as a countermeasure to prevent local bucking because of their high deformation capacity and load carrying capacity. When the pier endures high cyclic plastic deformation, low cycle fatigue will become a key issue. Most of researches on the concrete-filled steel piers focused on their ductility and seismic behavior using several parameters such as in-filled concrete strength and height, position of diaphragms and loading conditions. However, research on the extremely low cycle fatigue behavior of concrete-filled steel pier has been hardly performed yet. Therefore, it is needed to clearly investigate the failure mechanism of concrete-filled steel piers from the viewpoint of the extremely low cycle fatigue.

2. Extremely low cycle fatigue strength of welded joint in concrete-filled steel piers

Almost all of extremely low cycle fatigue damages in civil steel structure are initiated from welded joints, which results in fractures during earthquake. Generally, large plastic strain occurs at a weld toe or a weld root tip in welded joints. Moreover the strain concentration can be one of the main factors contributing to crack initiation. In the previous study (Ge et al., 1994) on ductility of concrete-filled steel pier, low cycle fatigue cracks were observed at welded joints during some tests. However, fatigue strength of the welded joint in concrete-filled steel piers has not been carefully and thoroughly investigated.

3. Extremely low cycle fatigue assessment method for concrete-filled steel piers

As stated above, there is a possibility that extremely low cycle fatigue failures will occur in concrete-filled steel piers. However, as for the concrete-filled steel pier, research has been hardly performed from the viewpoint of the extremely low cycle fatigue. It is needed to develop an extremely low cycle fatigue assessment method for concrete-filled steel piers.

1.3 Research objectives

Based on the discussions in the previous section, the purpose of this research is to develop the extremely low cycle fatigue assessment method of corner crack in concrete-filled steel piers with box section. **Fig. 1.4** shows the flowchart of this research.

The contents for discussion of this study are summarized as follows:

1) To investigate extremely low cycle fatigue fracture mechanism of concrete-filled steel piers with box section, concrete-filled pier specimens were fabricated and tested under large cyclic deformations. Based on the test results, the low cycle fatigue behaviors of the concrete-filled steel pier were experimentally investigated. Moreover, elasto-plastic finite element analyses were conducted to investigate deformation

behaviors around fatigue cracking sites in the specimen.

2) To develop the fatigue assessment method for welded joints in concrete-filled steel piers, welded joint specimens, which models the cracking part in the specimen mentioned in 1), were fabricated and tested under cyclic plastic deformation. Then, the fatigue strength of the joints was assessed by the proposed method in this study which is based on the effective notch concept.

3) To find out the validity of the effective notch strain based assessment method proposed in 2), the fatigue tests mentioned in 1) were assessed by using the method.

Extremely low cycle fatigue behavior of concrete-filled steel piers
Large-scale specimen and FE model

Extremely low cycle fatigue strength of corner welded joints
Small-scale specimen and FE model

Proposal of extremely low cycle fatigue assessment method
of corner crack in concrete-filled steel piers with box section
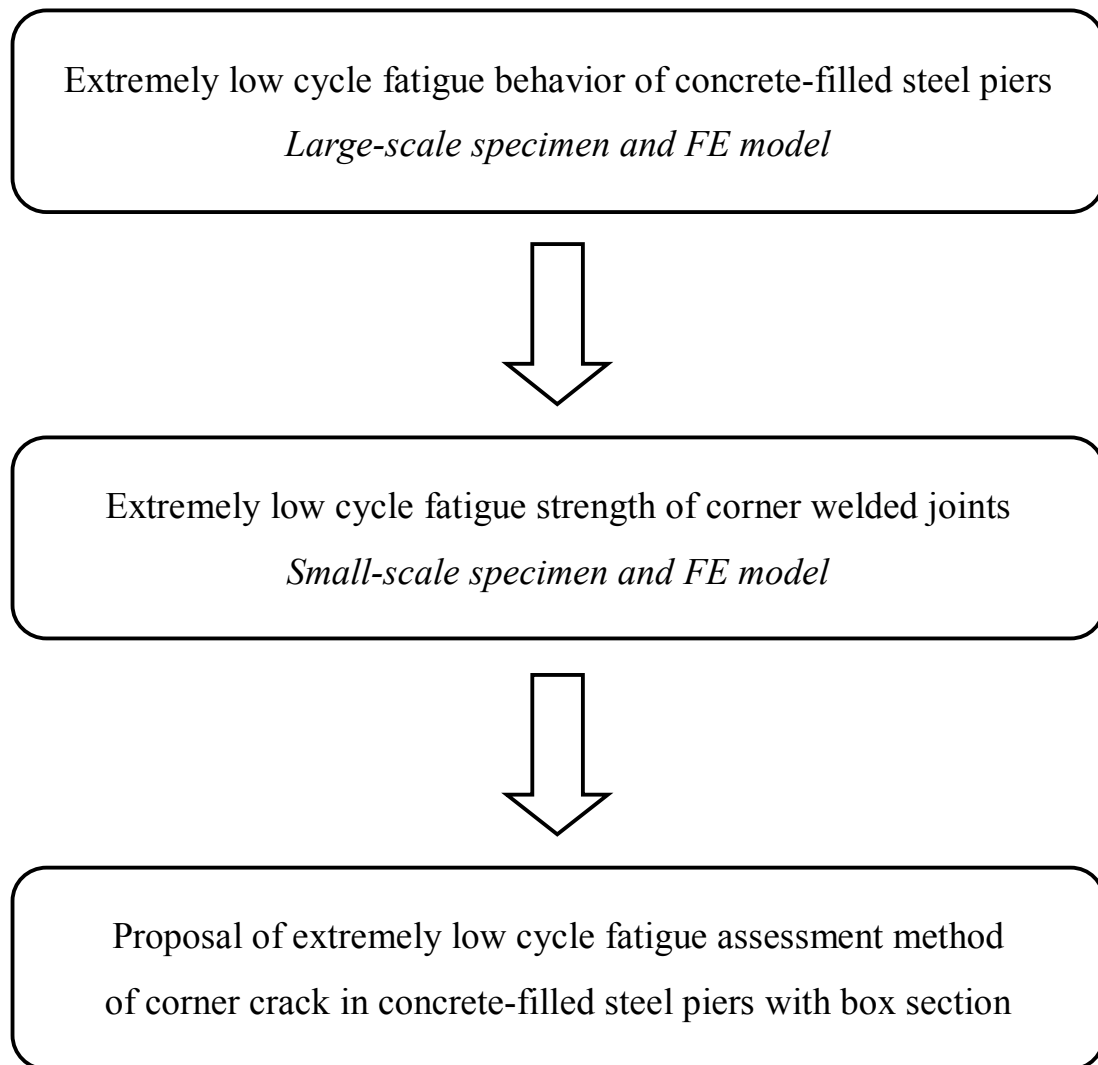
Fig. 1.4 Flow chart of this research

1.4 Structure of dissertation

Chapter 1 provides important background, previous studies, objectives and organization of the dissertation.

Chapter 2 performs extremely low cycle fatigue tests on concrete-filled steel pier with box section. Load-displacement hysteresis loops, types of damage, low cycle crack initiation and propagation behaviors are recorded. Then strain distribution and behaviors at the cracking sites in the specimen are investigated by finite element analyses.

Chapter 3 describes extremely low cycle fatigue assessment of corner welded joints using fatigue test and numerical analysis. As the results, the effective notch strain based fatigue assessment method is proposed. A unique fatigue strength curve is achieved which is relationship between the effective notch strain range and the fatigue life of welded joints.

Chapter 4 deals with the application of the effective notch strain based approach for concrete-filled steel piers. Finally, a new extremely low cycle fatigue assessment method for concrete-filled steel piers with box section is proposed.

Chapter 5 presents the summaries and conclusions of this study. The perspectives and recommendations for future study are also presented.

CHAPTER 2

EXTREMELY LOW CYCLE FATIGUE BEHAVOR OF CONCRETE-FILLED STEEL BRIDGE PIERS

2.1 Introduction

Ge et al. (1994) experimentally investigated the effect of the filling concrete on deformation capacity of steel piers. In the research, low cycle fatigue cracks were detected at welded joints during the tests. However, low cycle fatigue characteristics of concrete-filled steel piers have not been investigated in detail.

In this chapter, concrete-filled steel pier specimens were fabricated and tested under large cyclic displacement. Based on the test results, the extremely low cycle fatigue behavior of the concrete-filled steel pier was experimentally investigated. Moreover, elasto-plastic finite element analyses were conducted to investigate strain distributions around the cracking sites in the specimen.

2.2 Experimental procedures

2.2.1 Specimen configuration

Concrete-filled steel pier specimens were manufactured and tested. The configuration and dimension of the specimens are shown in **Fig. 2.1**. The specimen with a box section was fabricated by welding. The longitudinal welds between flange and web plates, which was called "corner weld" in this study, were connected with partial joint penetration groove welds, as shown in the figure. The plate thickness was 4.5mm, and flanges and webs were 200mm in width. Triangular ribs attached outside of the column near the base joint, because the ribs were often used in some of existing steel piers. Actually, low cycle fatigue failure occurred from the rib ends in the Hyogo-ken Nanbu Earthquake (Miki, 1996).

15
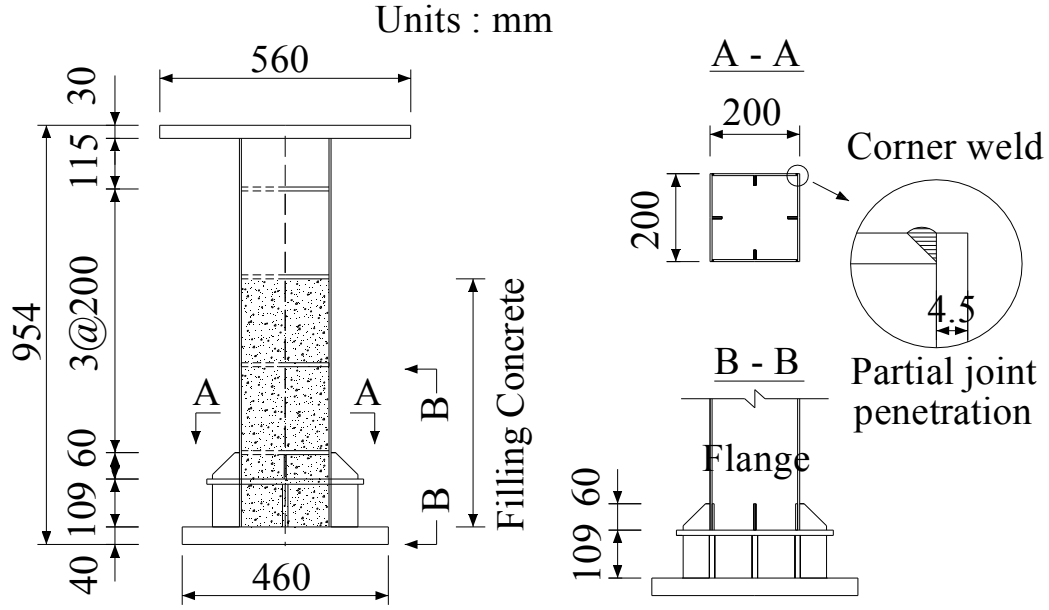
Fig. 2.1 Dimension of test specimen

The geometrical parameters were represented by the width-thickness ratio parameter (R_f) of a flange plate and the slenderness ratio parameter ($\bar{\lambda}$) given as follows,

$$R_f = \frac{b}{t}\sqrt{\frac{12(1-v^2)}{\pi^2 \kappa}}\sqrt{\frac{\sigma_y}{E}} \tag{2-1}$$

$$\bar{\lambda} = \frac{Kh}{R}\frac{1}{\pi}\sqrt{\frac{\sigma_y}{E}} \tag{2-2}$$

where b is flange width, t is plate thickness, σ_y is yield strength, E is Young's modulus, v is Poisson's ratio, κ is buckling coefficient of a plate, h is column height, K is effective length factor (K=2.0 for a fixed-free column), and R is radius of gyration of steel section. In the specimen, the width-thickness ratio parameter is 0.452 and the slenderness ratio parameter is 0.241.

The height of the filling concrete and the stiffener configuration were determined according to the previous study (Ge et al., 1994). In order to fill up the concrete to predetermined height, a hole was made in the center of diaphragms.

2.2.2 Mechanical property of materials

The mechanical properties of the steel and concrete used in this study are shown in **Table 2.1** and **Table 2.2**, respectively. Tensile tests were carried out on six specimens cut from the steel plates used for the specimen. Compression tests on the concrete were also performed on six specimens. The average values are shown in the tables.

Table 2.1 Mechanical properties of steel

Steel grade	Yield strength	Tensile strength	Elongation
SM400A	338 N/mm^2	417 N/mm^2	27 %

Table 2.2 Mechanical properties of filling concrete

Compressive strength	Modulus of elasticity	Remarks
27.7 N/mm^2	2.24×10^4 N/mm^2	28-days strength

2.2.3 Loading method

Test setup is shown in **Fig. 2.2**. The specimen was bolted at the base and loaded at the top. Lateral quasi-static cyclic load and constant axial load was applied to the top of the specimen. Six displacement transducers were installed to the specimen in order to calculate the top lateral displacement of the specimen.
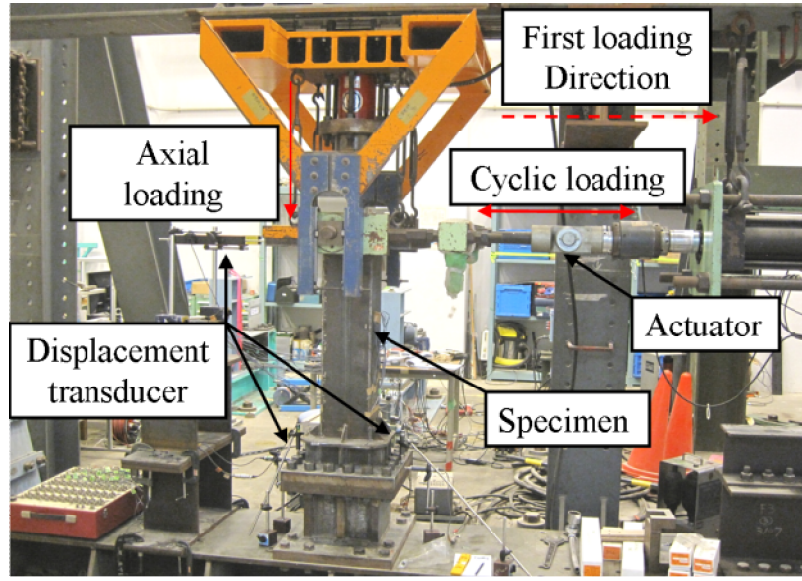
Fig. 2.2 Test setup

Incremental cyclic loading shown in **Fig. 2.3** was applied to the specimen top under displacement control. The initial horizontal yield load (H_{y0}) and yield displacement (δ_{y0}) was calculated based on Timoshenko beam theory considering a cross section of steel parts.

$$\delta_{y0} = \frac{H_{y0}h^3}{3EI} \tag{2-3}$$

$$H_{y0} = \left(\sigma_{y0} - \frac{N}{A}\right)\frac{Z}{h} \tag{2-4}$$

where M_{y0} is yield moment, h is height of specimen, EI is flexural stiffness, σ_{y0} is yielding strength of steel, N is applied axial force, A is section area of steel and Z is section modulus of steel.

As a result of calculation for 20% of yielding strength of steel, the initial horizontal yield load was 93.7kN and yield displacement was 3.77mm. In this study, the same displacement amplitudes were applied to all specimens to investigate the effect of the axial load on the low cycle fatigue behavior under the same load conditions.

18

Displacement/Initial yield displacement
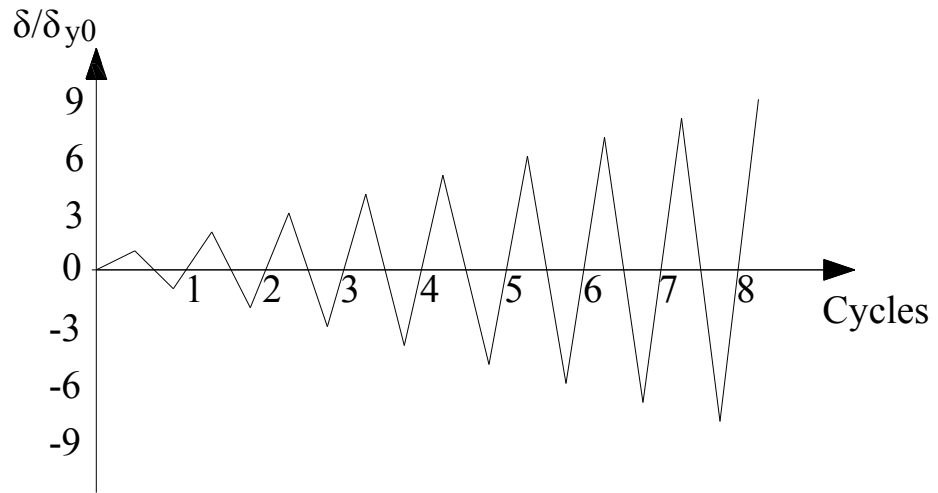
Fig. 2.3 Incremental cyclic loading for horizontal direction

2.2.4 Test matrix

Test matrix is given in **Table 2.3**. Three specimens were used for the low cycle fatigue tests. Two of them were filled with concrete which are called CF series. Another is called NCF which has no in-filled concrete in the pier. Constant compressive axial loads were applied to the specimens which were 10% or 20% of the yield strength of the steel. According to the applied axial load level, the specimens are named as shown in the table.

Table 2.3 Test matrix

Specimen name	In-filled concrete	Axial loading	Horizontal loading pattern
NCF20	None	$20\% \times \sigma_y$	
CF20	Exist	$20\% \times \sigma_y$	Incremental cyclic loading
CF10	Exist	$10\% \times \sigma_y$	

2.3 Experimental results

2.3.1 Overview of damage

Three types of damage were observed during the test, as illustrated in **Fig. 2.4**. One is local buckling. The other two are fatigue cracks from the welded joints. The crack, called "Type A crack", occurred at the welded joint between flanges and triangular ribs. Another is called "Type B crack", which was initiated from longitudinal welds connecting flange and web plates around the position where the local buckling occurred.

2.3.2 Load - displacement hysteretic curves

Fig. 2.5 shows the load-displacement hysteretic curves. The abscissa represents the horizontal displacement at the top of the specimen, whereas the ordinate indicates the load of the actuator. And in these figures, the number of cycles when the damages were first observed is denoted with marks.

In the NCF20 specimen, the maximum load carrying capacity rapidly decreased after the local buckling occurred. After the maximum load was dropped by 5% and 41%, Type A and Type B crack were observed at the welded joint. In the CF20 and CF10 specimens, the load carrying capacity was higher than that of NCF20 and hardly reduced due to the local buckling. In the graphs, it can be found that the maximum load begins to decrease after the Type B crack was detected.
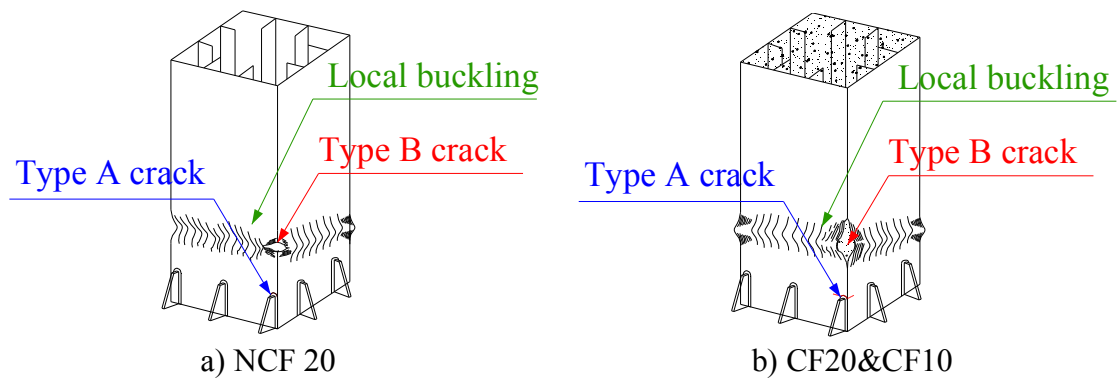
a) NCF 20

b) CF20&CF10

Fig. 2.4 Overview of damage
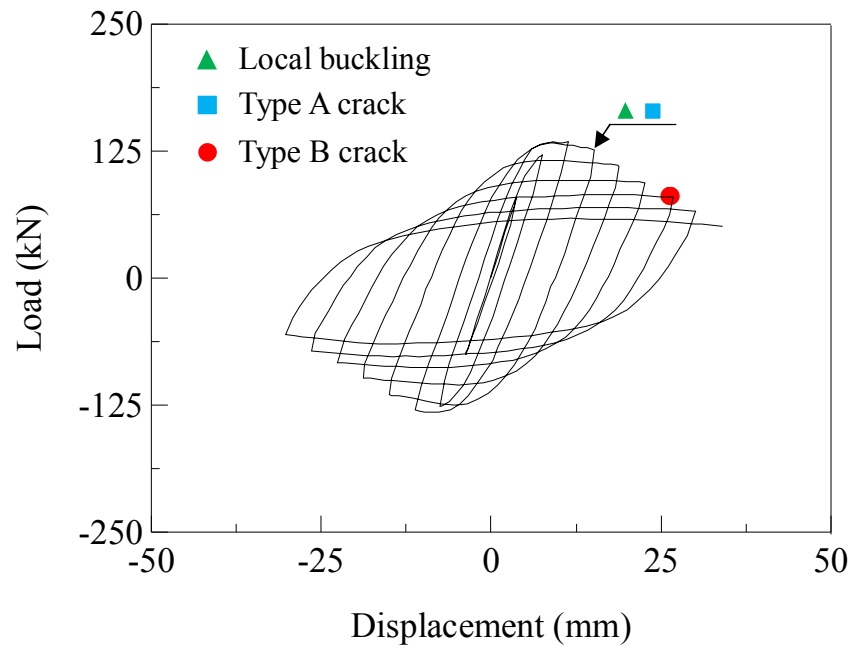
a) NCF 20

Fig. 2.5 Load - displacement hysteretic curves
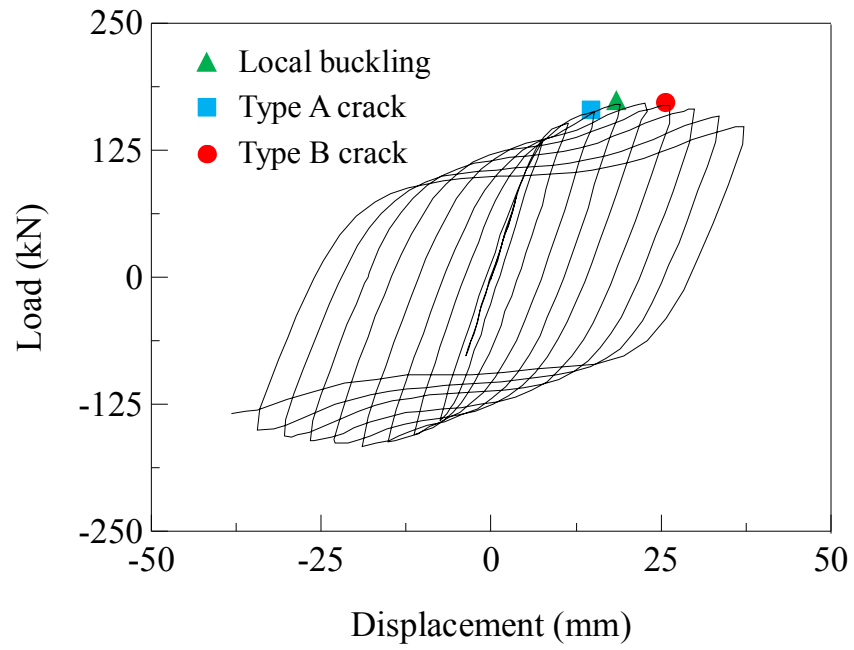
b) CF 20
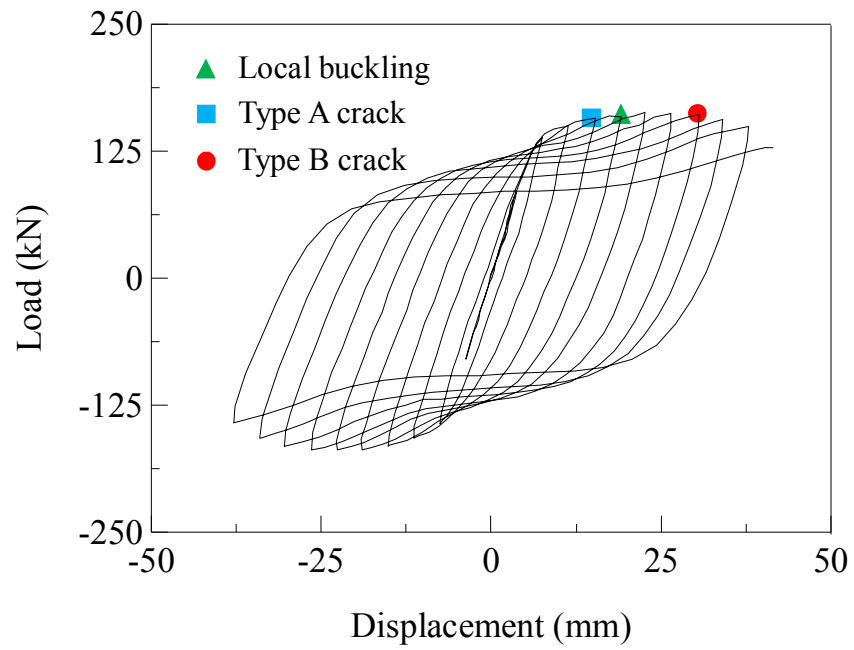
c) CF 10

Fig. 2.5 Load - displacement hysteretic curves (Continued)

22

2.3.3 Failure scenarios

Failure scenarios of each series of the specimen are illustrated in **Fig. 2.6** and **Fig. 2.7**. In the NCF20 specimen, the local buckling occurred in the flange plate of loading direction, and the fatigue cracks coincided at the welded joint between the flanges and triangular ribs in the opposite flange. The buckling was appeared as concave shape on the flange and convex shape on the web. As the buckling grows, another crack originated from the corner weld around the locally-buckled area. The crack propagated perpendicular to the weld.

In the CF20 and CF10 specimens, the low cycle fatigue cracks occurred from the triangular ribs at first. Then, local buckling was observed on the flange and web plates, of which shape was convex on both flange and web plates. After that, the corner welds around the locally-buckled area were split vertically by cyclic plastic strains due to out-of-plane deformation of the flange and web.

a) Type A crack   b) Local buckling   c) Type B crack
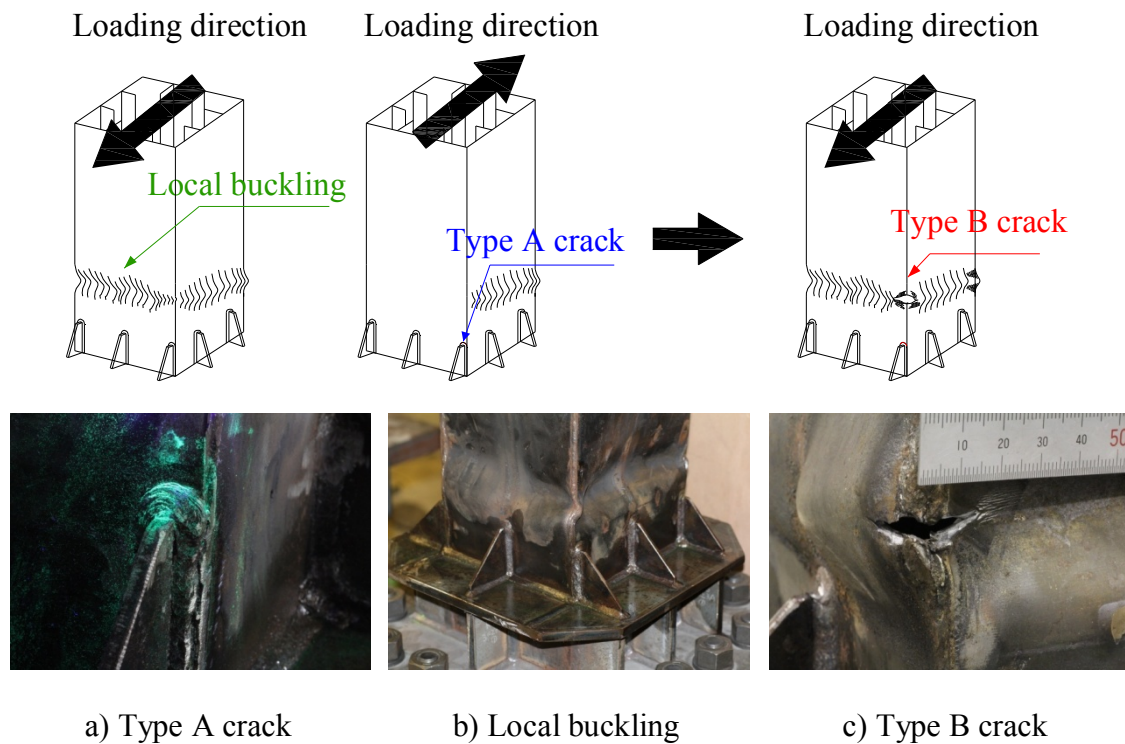
Fig. 2.6 Failure scenarios of NCF specimen

a) Type A crack   b) Local buckling   c) Type B crack
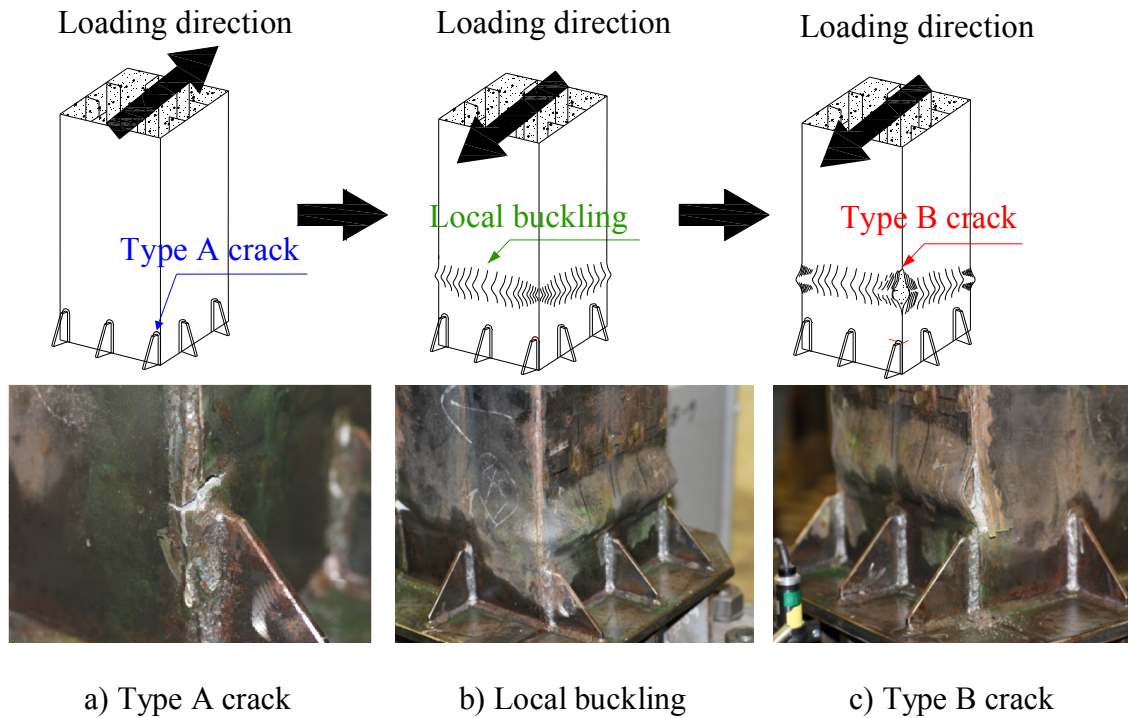
Fig. 2.7 Failure scenarios of CF series specimens

2.3.4 Relationship between crack length and load

During the test, the fatigue crack observation was performed with magnetic particle testing method (MT) at each cycle. Type A crack was firstly detected on the weld toe of welded joints in all specimens. The crack surface lengths were about from 3.75mm to 6mm. The depth of cracks was approximately 0.5mm. However, for the Type B crack, it is impossible to observe the crack detection visually because the crack initiated from inside of specimen. Therefore, Type B crack was firstly observed when the crack penetrated through the weld bead.

The relationships between the crack lengths measured during the test and the number of cycles are shown in **Fig. 2.8**. In the graph, the maximum loads at each cycle are also indicated. In the NCF20 specimen, the low cycle fatigue crack occurred from the triangular rib at the same cycle with the local buckling. After another crack originated from the corner weld around the locally-buckled area, there was little growth in the crack at the triangular rib.

24

The number of cycles when the cracks were first detected at the triangular rib is the same in both the CF20 and CF10 specimens. The crack propagated in the similar tendency regardless of the axial load level. With respect to the cycles of the vertical crack initiation from the corner weld, differences can be observed due to the axial load level.

The load carrying capacity of the concrete-filled pier began to decrease by the growth of the vertical crack at the corner weld. Therefore, the crack from the corner weld is one of the main failure modes of the concrete-filled steel pier.

a) NCF 20
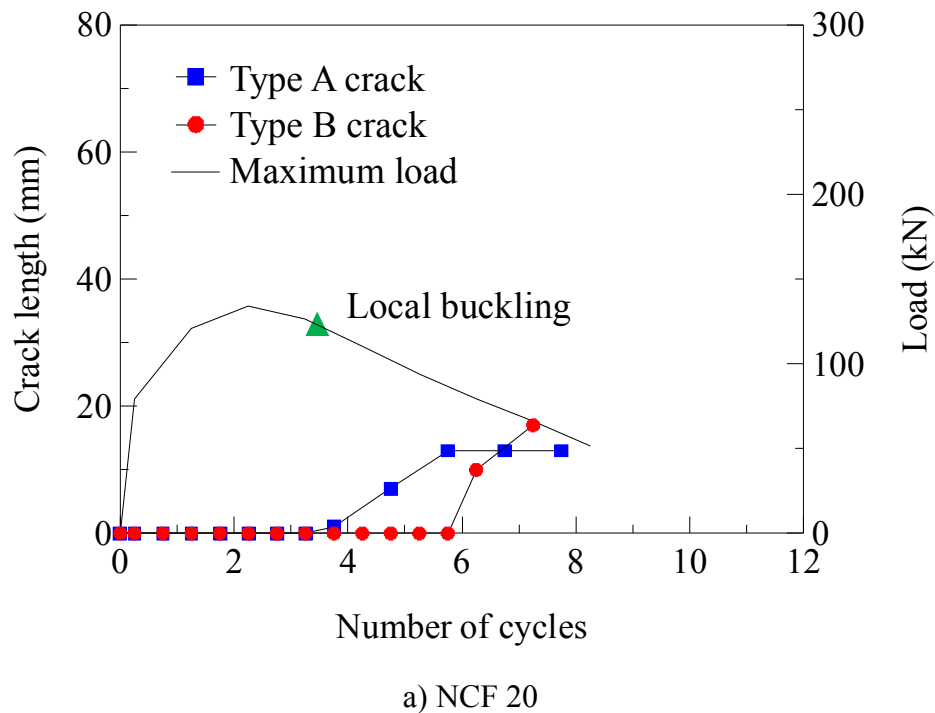
Fig. 2.8 Crack length versus number of cycles
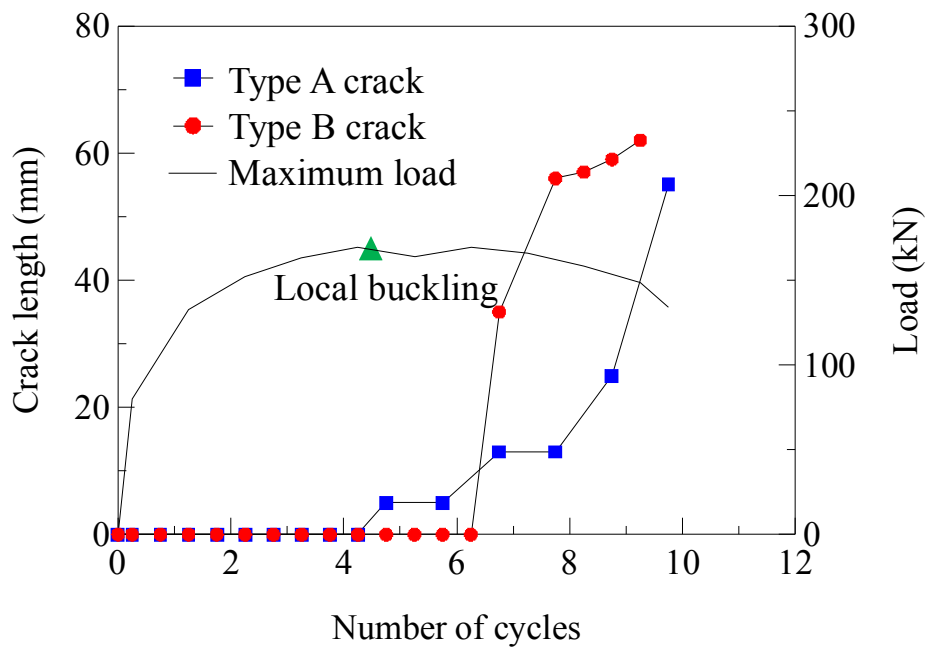
b) CF 20
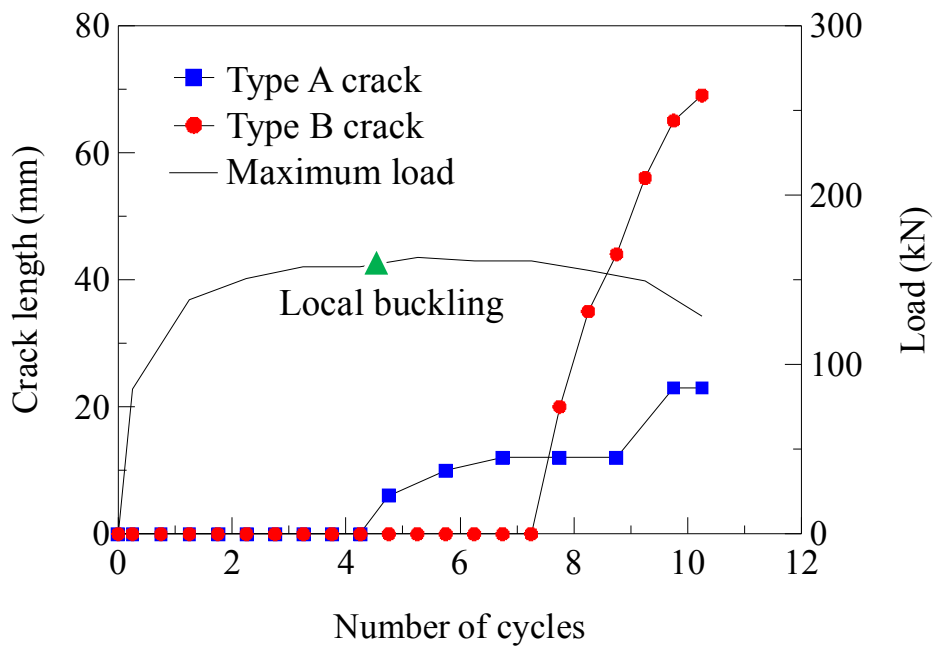
c) CF 10

Fig. 2.8 Crack length versus number of cycles (Continued)

2.4 Finite element analyses

2.4.1 Analysis methods

Elasto-plastic finite element analyses were conducted by using ABAQUS program under the same condition of the experiment to investigate deformation behaviors around the cracking sites in the specimen. **Fig. 2.9** illustrates FE model of steel plates and internal concrete.

The steel plates were modeled by shell and solid elements. In order to simulate welded part, around the crack detected point at the corner weld was created with solid elements. As shown in **Fig. 2.10**, the weld root also modeled in the solid part. The weld root size refers to the actual welding shape of the test specimen. Four-node and thick shell element are used in the shell part, whereas eight-node and hexahedral iso-parametric elements are used in the solid part.
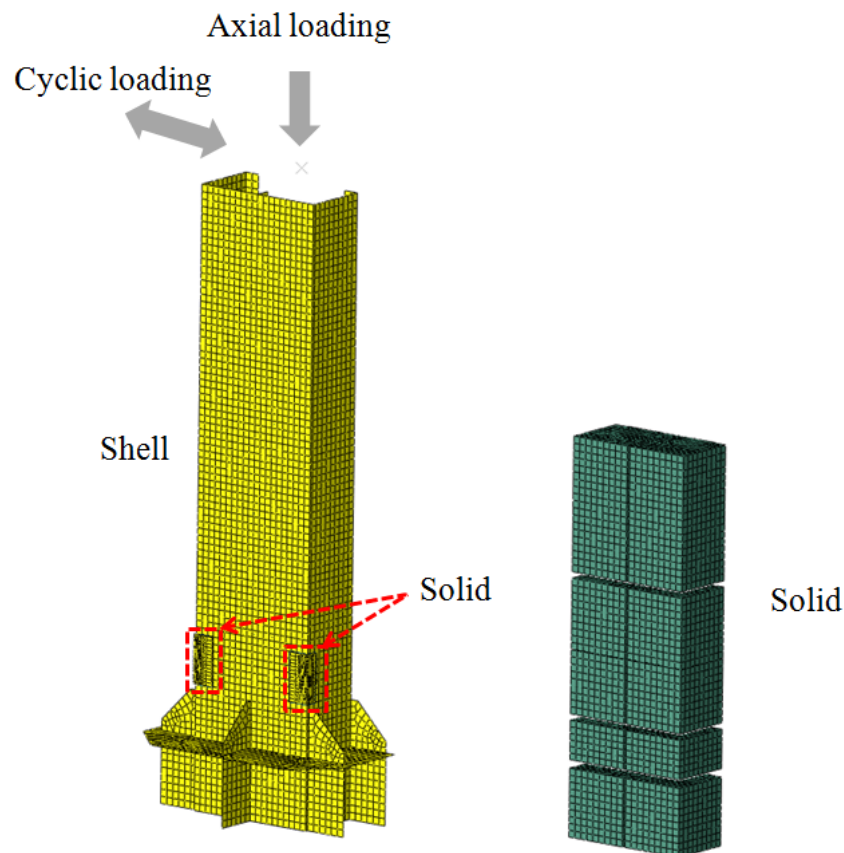
Fig. 2.9 FE model of steel plates and internal concrete
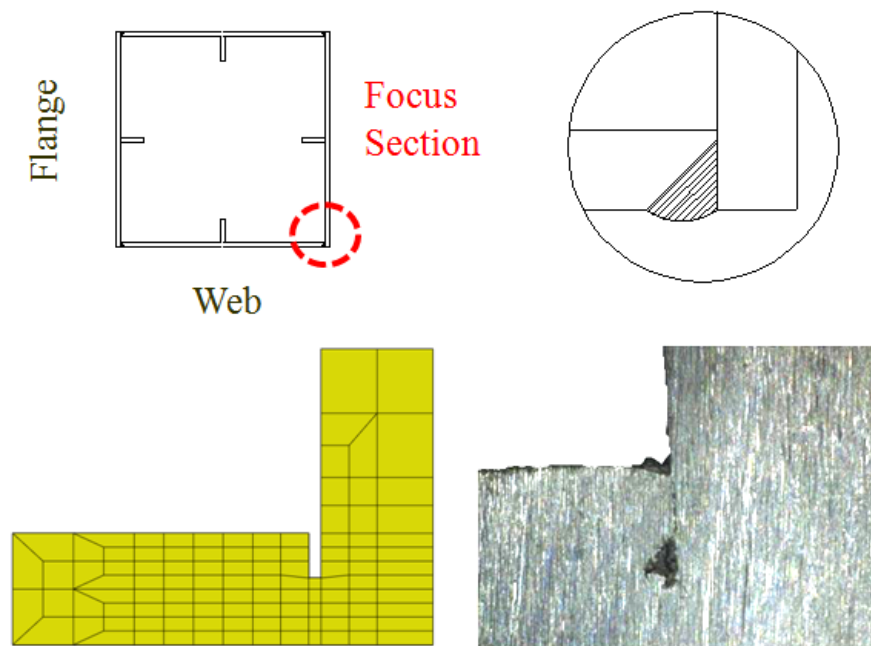
Fig. 2.10 Details of solid parts of steel plates
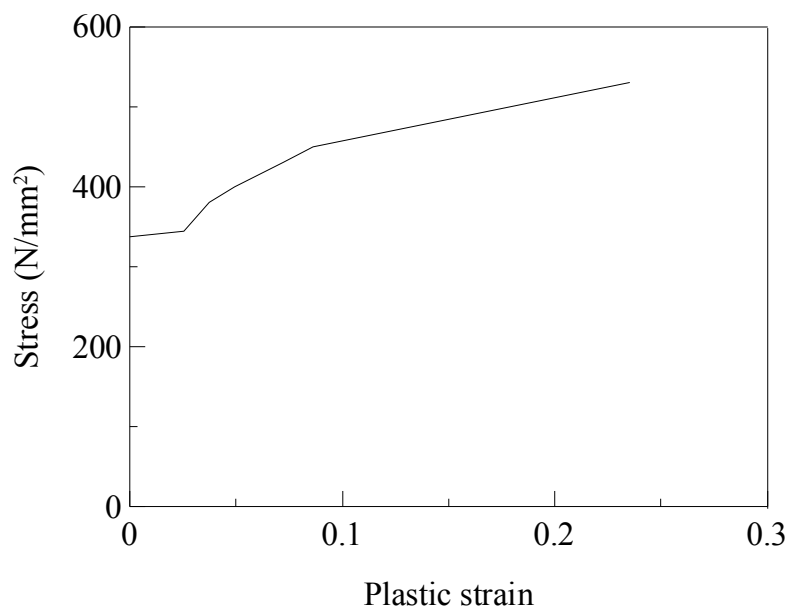
Fig. 2.11 Stress – plastic strain relation for steel

According to the material test results, stress-strain relationships of the steel were determined as shown in **Fig. 2.11**. The yield strength, Young's modulus and Poisson's ratio are 338N/mm^2, 2.0×10^{5}N/mm^2 and 0.3, respectively. The combined isotropic and kinematic hardening model with the von Mises yield surface was used.

The internal concrete was modeled by solid elements, as shown in **Fig. 2.9**. As for the internal concrete, the compressive strength, Young's modulus and Poisson's ratio are 27.7N/mm^2, 2.0×10^{4}N/mm^2 and 0.2, respectively.

The concrete damaged plasticity model (Lee and Fenves, 1998) was employed in this study. Concrete material parameters required to define in this model were Young's modulus (E_c), Poisson's ratio (v_c), equivalent stress-equivalent strain relationships, compressive damage parameters (d_c), tensile damage parameter (d_t), dilation angle (Ψ), shape factor for yield surface (K_c), equibiaxial stress ratio (σ_{b0}/σ_{c0})(equibiaxial yield stress/ uniaxial yield stress), and eccentricity (e). Among these parameters, only limited parameter values were known such as the Young's modulus, the compressive strength and the Poisson's ratio by the concrete compression test. Therefore, this study referred to the previous study (Goto, 2009) to determine the unknown parameters for the model. The compressive stress-plastic compressive strain curve determined in the model is shown in **Fig. 2.12(a)**.

The tensile strength of the concrete was assumed as 10% of its compressive strength (Matsumura and Mizuno, 2007). As a tensile stress (σ_t) and crack opening (u^{cr}), a linear relation with the negative stiffness, schematically shown in **Fig. 2.12(b)**, is assumed as the first-order approximation (Goto, 2010).

The compressive damage parameter (d_c) is determined by the empirical formula as shown in **Fig. 2.13(a)** (Goto, 2010). And the tensile damage parameter (d_t) is assumed to be expressed as in **Fig. 2.13(b)**, following ABAQUS (2014). The crack opening (u^{cr}) can be converted into plastic tensile strain by u^{cr} / l_0, where $l_0 = V^{1/3}$. V denotes the averaged in-filled concrete element volume in FE model.
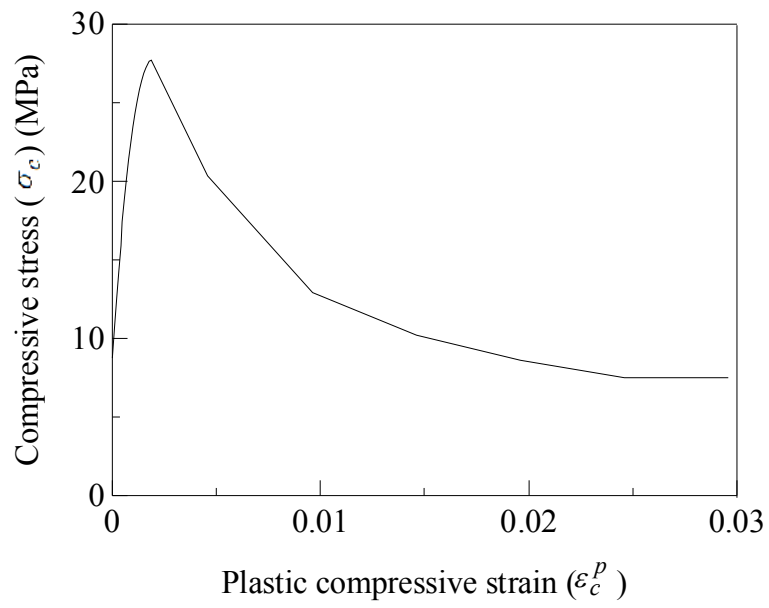
a) Compressive strain - plastic compressive stain relation
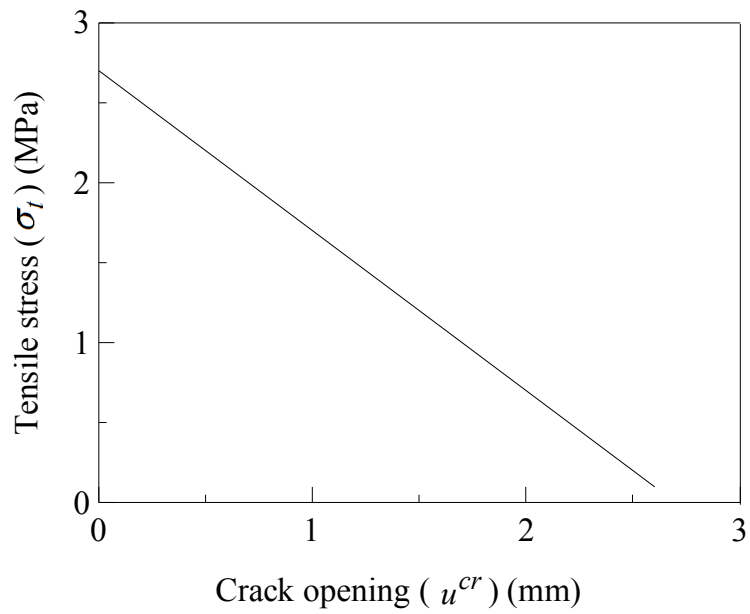
b) Tensile stress - crack opening relation

Fig. 2.12 Compressive and tensile behavior of concrete

$$d_c = \frac{155\varepsilon_c^p}{\left[1 + \left(\varepsilon_c^p / 0.0035\right)^{1.08}\right]^{1.08}}$$

a) Compressive damage parameter (d_c)

$$d_t = \frac{E_c u^{cr} / l_0}{E_c u^{cr} / l_0 + \sigma_t}$$

Element characteristics length $l_0 = V^{1/3}$
σ_t = Tensile stress
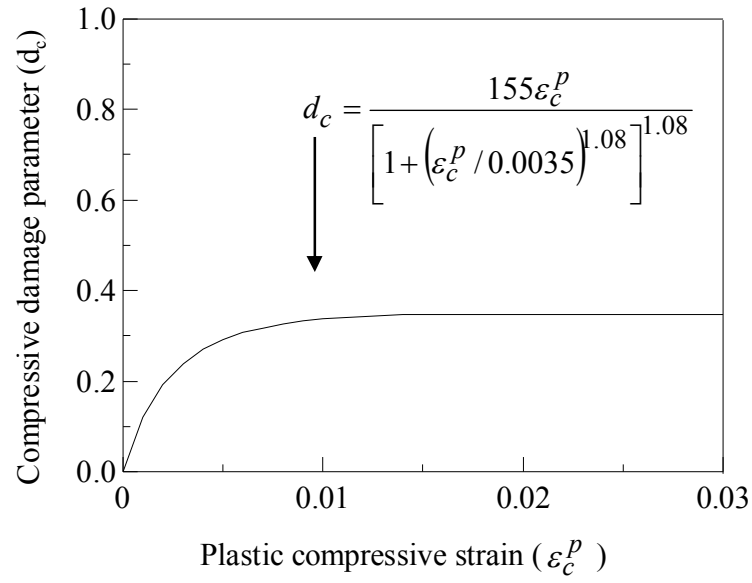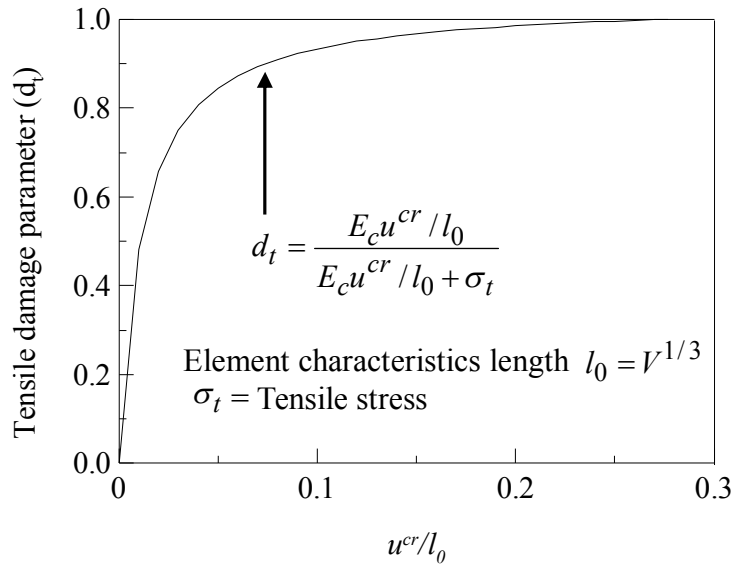
b) Tensile damage parameter (d_t)

Fig. 2.13 Damage parameters for concrete

As the input data was not available for Ψ, Kc, σ_{b0}/σ_{c0}, and e, $\sigma_{b0}/\sigma_{c0} = 1.16$, $K_c = 0.67$, and $e = 0.2$ are used as the default recommended values by ABAQUS (2014). Ψ was determined to be 20° as a value when the structural analysis results fitted in best with the experiment results.

The discrete crack model was applied to simulate crack opening and closing behavior of the in-filled concrete under cyclic loadings (Goto, 2010). The locations of discrete cracks in the concrete are expressed in terms of distance from bottom surface, as shown in **Fig. 2.14**. The discrete cracks were inserted into the cross section of the internal concrete horizontally at the locations which were determined by trial analysis using without discrete crack model. The locations of discrete crack were locally-buckled area occurred in experiment and high tensile stress of the concrete was observed in trial analysis.

Contact elements were applied to the interface between the steel and the concrete. The friction coefficient is determined as 0.2 for the steel to concrete (Johansson and Gylltoft, 2001) and 1.0 for the concrete to concrete crack surface (ACI, 2001).
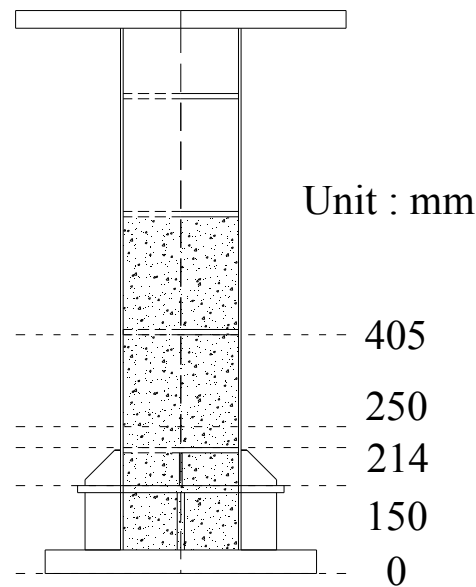
Fig. 2.14 Locations of discrete cracks in in-filled concrete

2.4.2 Comparisons with test results

Fig. 2.15 shows comparisons of the hysteresis loops between the analysis and the experiment. It is observed in the graphs of the CF series that the initial slopes are slightly different between the analysis and the experiment. This may be because the degradation of the concrete is occurred quickly during the test under the cyclic loading. But the analysis results and the experiments show relatively good agreement. The tendency of the stiffness degradation and recovery in cyclic loading process can be expressed by the analysis which is similar with the experiment results before the low cycle fatigue failure was observed.
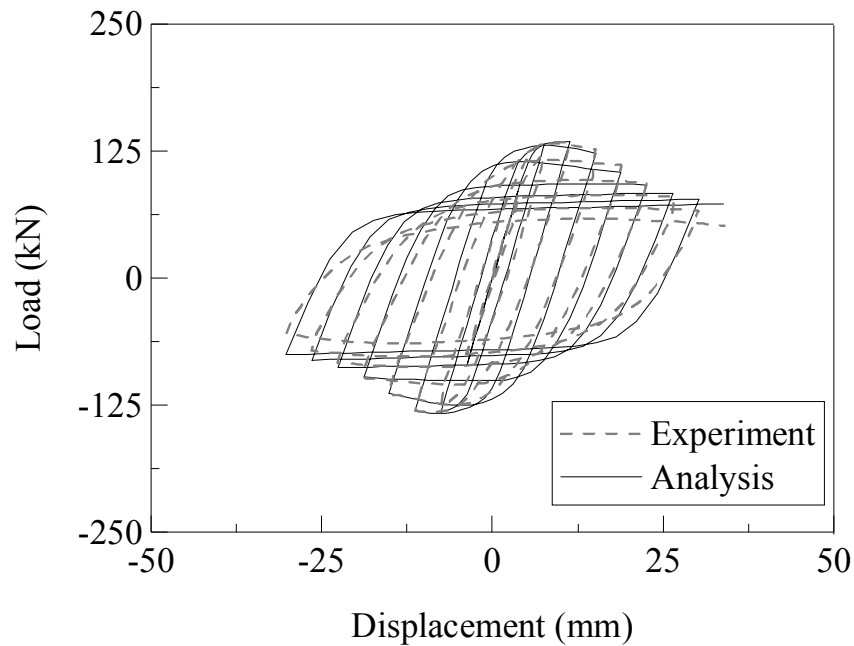
a) NCF20

Fig. 2.15 Comparisons of hysteretic curves
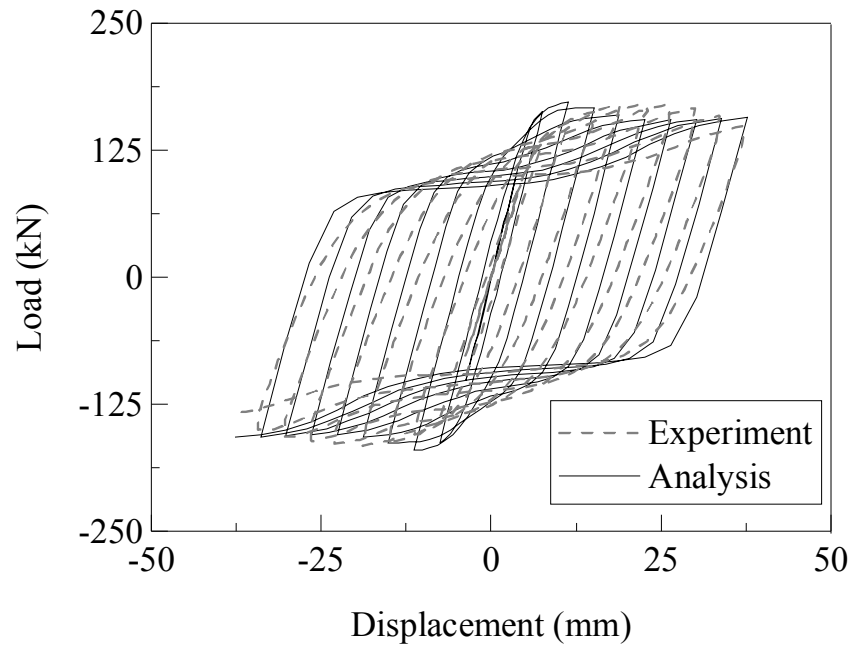
b) CF20
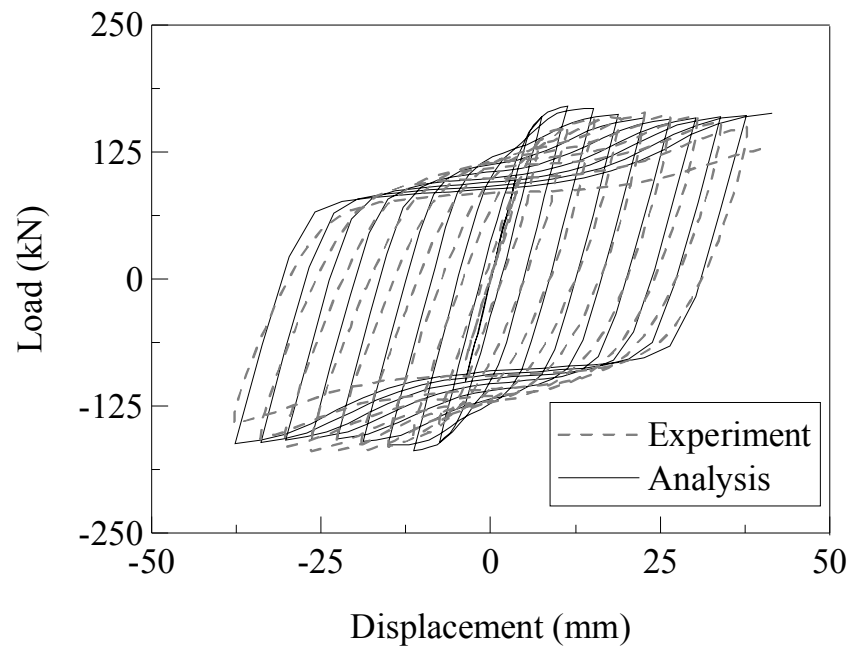
c) CF10

Fig. 2.15 Comparisons of hysteretic curves (Continued)

Fig. 2.16 and **Table 2.4** show comparisons of deformation shapes between experiment and analysis. The location of the local buckling and its shape in the analysis was similar with the experiment. Form these results, the validity of the finite element modeling was proved.

a) NCF20
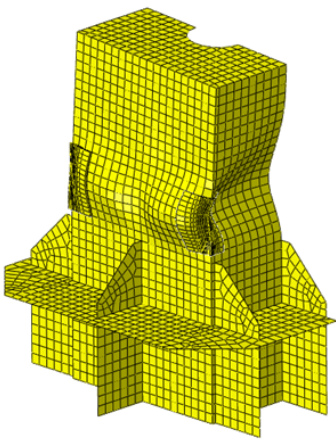
b) CF20
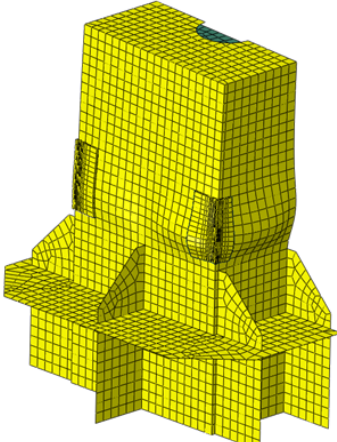
Fig. 2.16 Comparisons of deformation shapes

Table 2.4 Examples of deformations of locally-area (CF20, 3.25cycles)
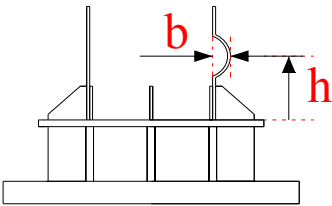
	Experiment (mm)	Analysis (mm)
b	20.0	20.6
h	100	116.0

2.4.3 Local deformation around cracking site

Fig. 2.17 shows local deformation and principal strain distribution around the corner weld when the focus section is in the compression side (5.25 cycles) and in the tension side (5.75 cycles), respectively. High strain can be seen at the weld root tip. Besides, the weld root tends to open when it is in the compression side because of the out-of plane deformation of the flange and web plates due to the buckling, whereas the root tip opening width decreases in the tension side. It means that the weld root repeats opening and closing by cyclic loading, which is one of the causes of low cycle fatigue cracks from the corner weld in the concrete-filled steel piers.

a) Compression state in focus section
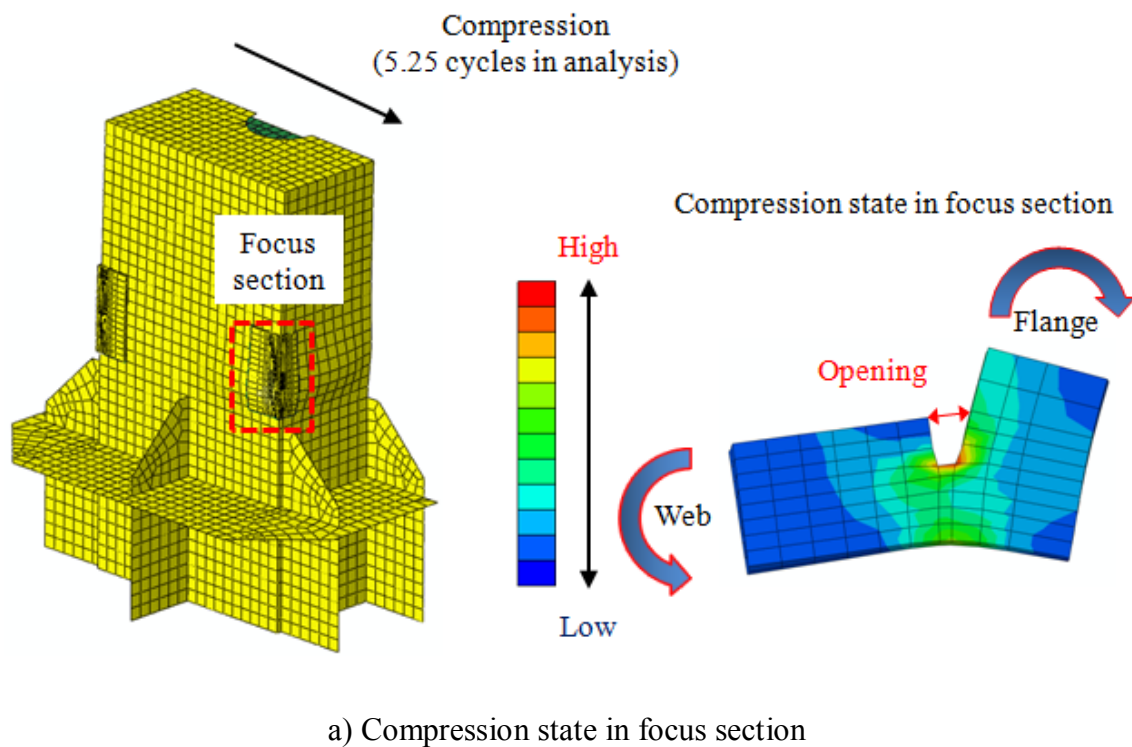
Fig. 2.17 Local deformation around corner weld (CF20 specimen)
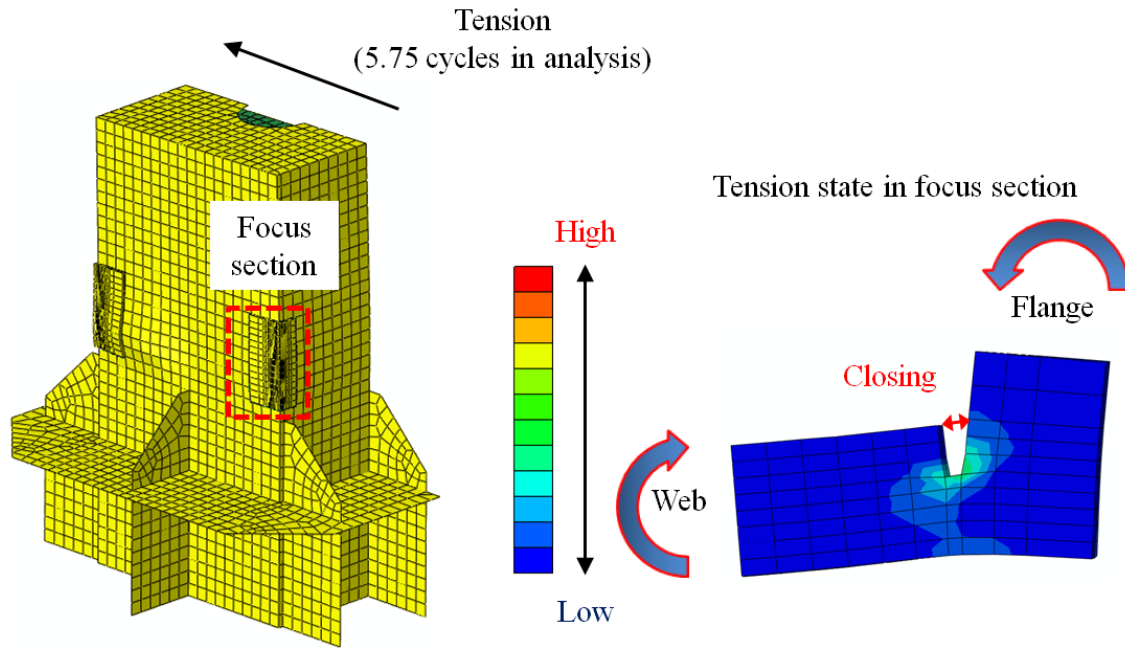
b) Tension state in focus section

Fig. 2.17 Local deformation around corner weld (CF20 specimen) (Continued)

2.4.4 Principal strain directions around cracking site

To investigate the effect of axial force, the principal strain directions around cracking site are defined in the focus section, as shown in **Fig. 2.18**. When the weld root opens (5.25 cycles), the direction is located xy-plane horizontally. When the weld root moves to close (5.75 cycles), the direction is small changed to vertical direction. However, the dominant direction is also located xy-plane. It is indicated that the effect of axial force is very small from viewpoint of occurrence of low cycle fatigue cracks at corner weld in the concrete-filled steel piers.
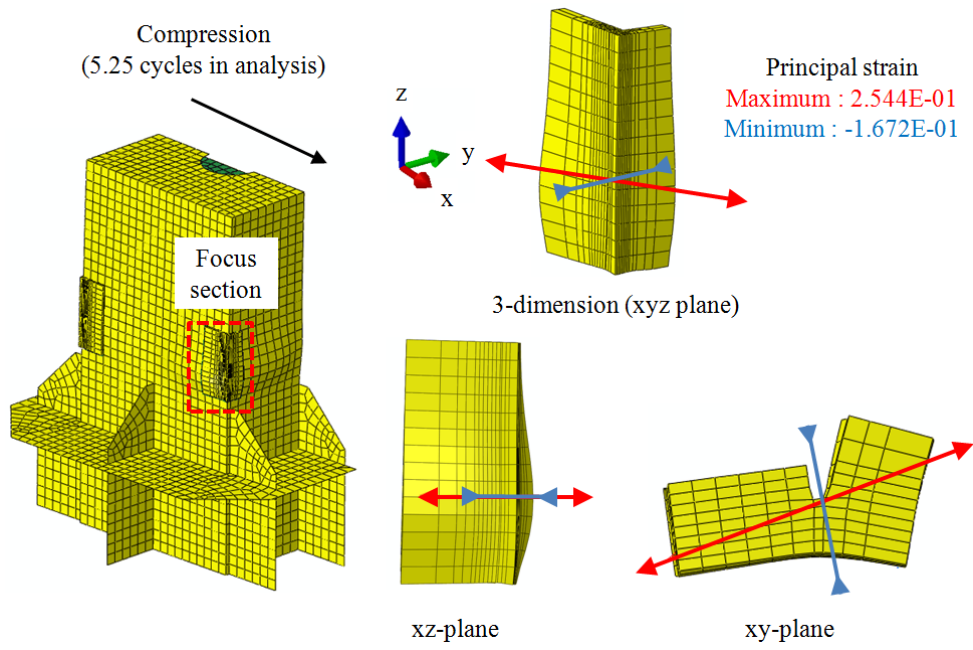
a) Compression state in focus section
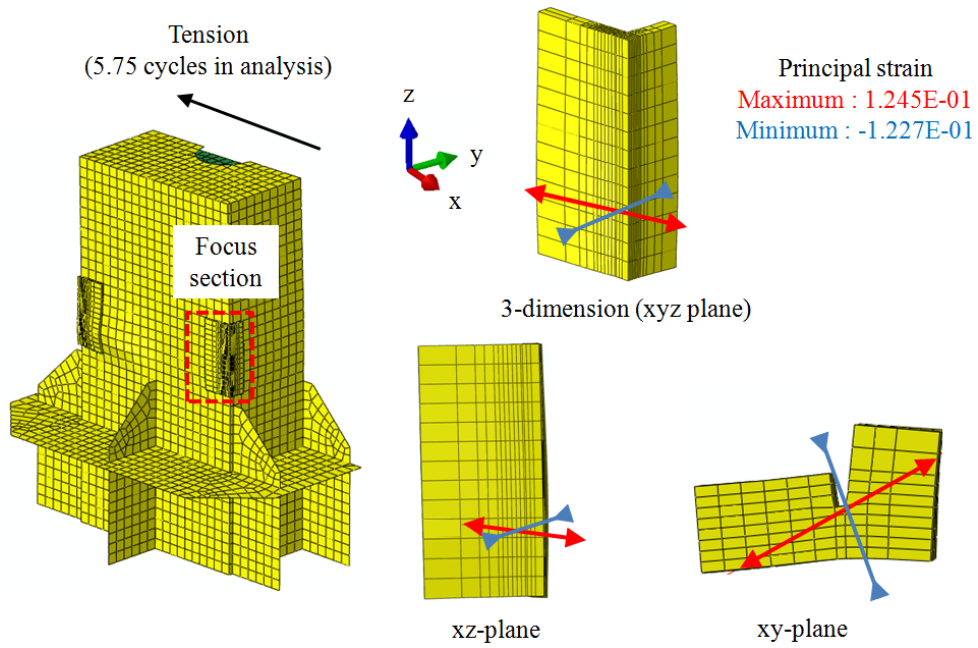
b) Tension state in focus section

Fig. 2.18 Principal strain directions around cracking site (CF20 specimen)

2.5 Concluding remarks

In this chapter, the extremely low cycle fatigue behaviors of concrete-filled steel piers were experimentally and analytically investigated.

Following conclusions can be drawn:

1) In the concrete-filled steel pier specimen, low cycle fatigue cracks occurred first from the triangular ribs. Then, local buckling was observed on the flange and web plates. After then, the corner weld around the locally-buckled area was split vertically by cyclic plastic deformation. The buckling deformation was relatively small compared with that of no in-filled concrete steel pier and the load carrying capacity was hardly reduced due to the local buckling.

2) The load carrying capacity of concrete-filled steel pier specimen decreased due to the crack initiation and propagation from the corner weld. This crack is one of the main failure modes of the concrete-filled steel piers.

3) The strain behaviors around the cracking site were revealed by elasto-plastic finite element analyses. The analysis result indicated that the crack from corner weld in the specimen is initiated at the weld root tip by its opening and closing behavior due to cyclic out-of-plane bending deformation of the flange and web plates.

CHAPTER 3

EXTREMELY LOW CYCLE FATIGUE STRENGTH OF CORNER WELDED JOINTS AND ITS EVAUATION METHOD BASED ON LOCAL STRAIN

3.1 Introduction

In the preceding chapter, it was revealed that low cycle fatigue cracks on concrete-filled steel pier with box section are initiated from longitudinal welds connecting flange and web plates, which can cause a decrease of load-carrying capacity of the pier.

As a countermeasure of the crack from the corner weld, current design code (Japan Road Association, 2012) has recommended a welding method with enough penetration, such as K-groove welding shown in **Fig. 3.1(b)**. However, in the existing steel piers retrofitted against local buckling by filling with concrete, single bevel groove welds and relatively small amount of fillet welds inside of two plates were often used in the corner welded joints, as shown in **Fig. 3.1(c)**. However, the relatively small amount of fillet weld may be easily failed under the cyclic plastic deformation. And then, the weld root in the single weld has possibility to cause low cycle fatigue failures. Therefore, it is needed to develop the fatigue strength evaluation method of the corner welded joints.
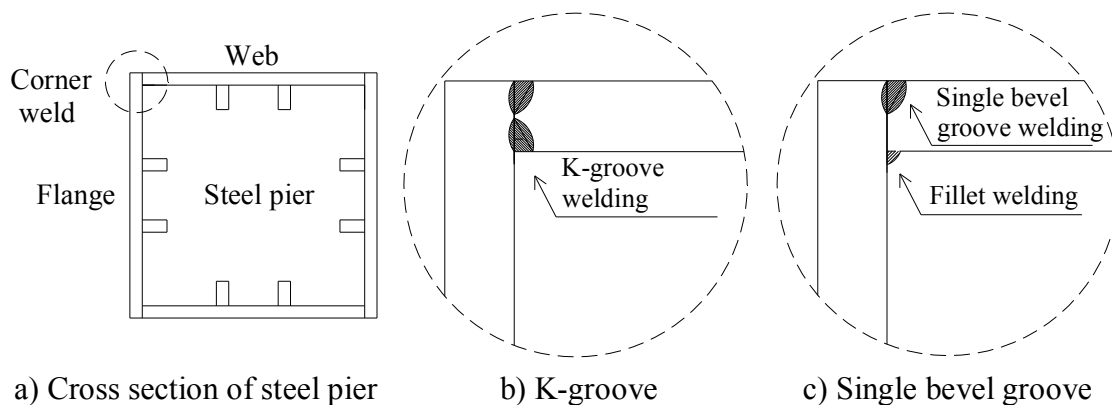

a) Cross section of steel pier   b) K-groove   c) Single bevel groove

Fig. 3.1 Typical welding types of corner welded joints

In the previous research on low cycle fatigue test of T-shape welded joints (Hanji et al., 2006), where fatigue cracks were initiated from a weld toe, it was demonstrated that fatigue strength of welded joints can be evaluated by strain amplitude at a cracking site, which is called "local strain".

In corner welded joints, however, it is difficult to calculate local strain because low cycle fatigue cracks are usually initiated from a tip of weld root. In high cycle fatigue regions where deformations are primarily elastic, in order to obtain local stress at the root tip, the effective notch concept has been proposed (Radaj et al., 2006; Fricke et al., 2008). In the effective notch approach, as shown in **Fig. 3.2**, a fictitious notch with a fixed radius, which is called "effective notch", is introduced at a root tip and fatigue strength can be evaluated based on stress calculated along the notch.
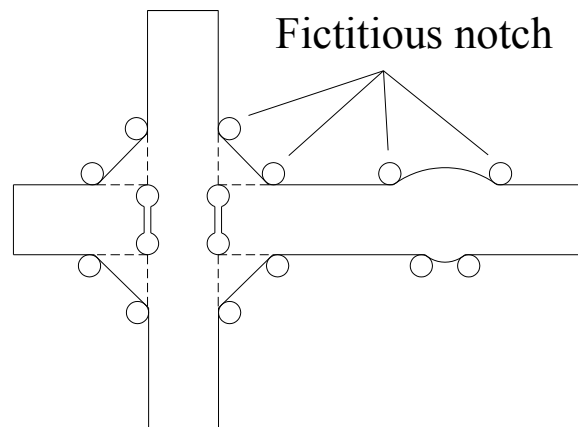
Fig. 3.2 Fictitious rounding of weld toes and roots (Hobbacher, 1996)

Previous study has applied using this method to low cycle fatigue regions and indicated that the fatigue strength of load-carrying cruciform welded joints with root cracks can be evaluated by the effective notch strain regardless of weld root size and main plate thickness (Hanji et al., 2011).

In this chapter, in order to develop the fatigue assessment method for corner welded joints in the extremely low cycle fatigue region, fatigue tests of the corner joints were performed under large cycle bending deformations. Based on the results, the applicability of the effective notch strain approach to the corner joints was investigated.

3.2 Experimental procedures

3.2.1 Specimen configuration and fabrication methods

Fig. 3.3 shows the configuration and dimension of the specimens. The specimens were corner welded joints with single bevel groove welding, which simulate a corner weld in existing steel bridge piers with box section. Steel plates of SM490YA with a thickness of 16mm were used to the specimen. The mechanical properties and chemical compositions of the material are tabulated in **Table 3.1**. The welding method was CO_2 gas welding under flat position. Three types of specimen were used in the experiments, which have different sizes of weld root face (0mm, 4mm and 8mm in design). **Table 3.2** summarizes specimen series and average values of weld profiles measured in the specimen.
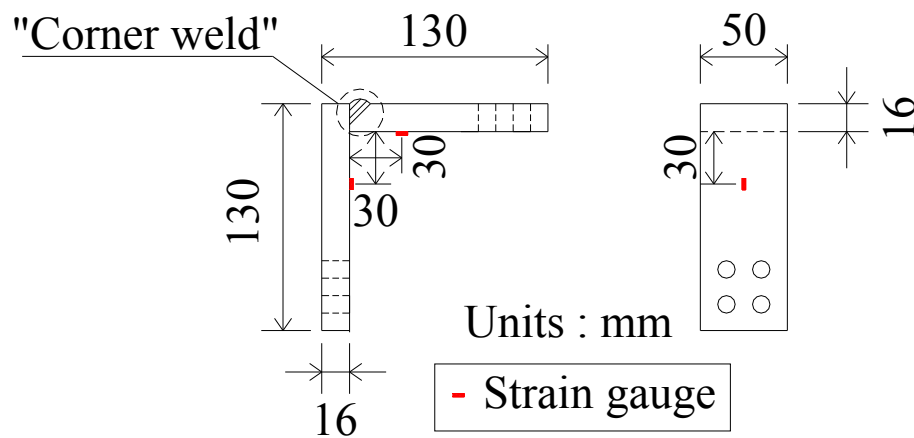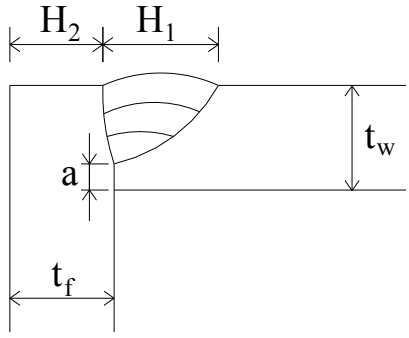

Fig. 3.3 Configuration and dimension of specimens

Table 3.1 Mechanical properties and chemical compositions

SM490YA	Yield Stress (N/mm^2)	Tensile Strength (N/mm^2)	Elongation (%)	Chemical compositions (%)				
				C	Si	Mn	P	S
	429	532	19	0.15	0.20	1.10	0.014	0.004

Table 3.2 Average values of weld profiles

Specimen	t_f (mm)	t_w (mm)	a (mm)	H_1 (mm)	H_2 (mm)
C0	16.35	16.13	1.10	20.00	14.00
C4	16.28	16.10	4.75	17.50	14.00
C8	16.30	16.01	8.00	11.50	15.00

3.2.2 Loading methods

As indicated in Chapter 2, the low cycle fatigue crack from the corner weld in the concrete-filled specimen were caused by cyclic out-of-plane bending deformation of the flange and web plates. In order to apply the cyclic bending deformations to the corner joints specimen, loading devices were newly developed as described below.

Fig. 3.4 shows the test setup. Loading devices were attached to both the upper and lower side of the specimen. Cyclic bending deformations can be applied to the specimen by moving the devices up and down. Displacement transducers were installed as shown in the figure to measure the vertical displacement of the devices.

The tests were performed by controlling the fluctuation range of the displacement. Three types of constant displacement ranges of 12~18mm were applied to the specimen. In the test, the minimum displacement was basically set to be 0mm. In some specimens of the displacement range of 12mm, the minimum displacement was change to 3mm and 6mm to investigate the effect of the mean strain on fatigue strength. As shown in **Fig. 3.3**, strains in the specimen were recorded by strain gauges attached 30mm away from the inner intersection between two plates. The cyclic loading was applied until the specimen was broken completely.
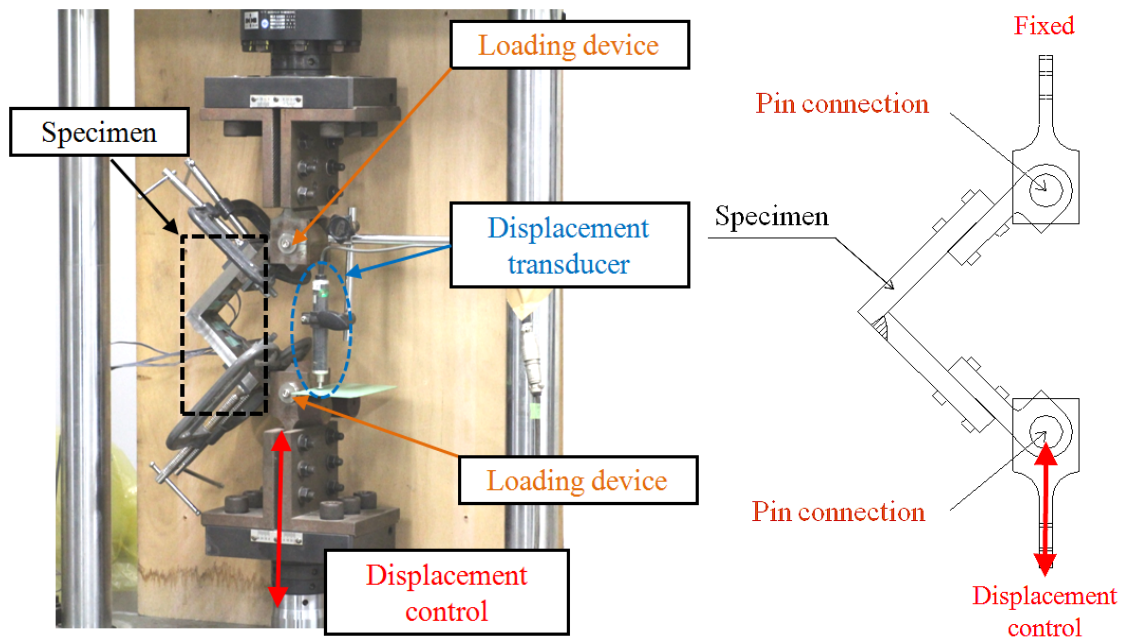

Fig. 3.4 Test setup

3.2.3 Test matrix

Test matrix is given in **Table 3.3**. According to the size of the weld root face (0mm, 4mm and 8mm in design) and the displacement range (12mm, 15mm, and 18mm), the specimens were named as shown in the table. For example, "C4-15" represents 4mm in the weld root size and 15mm of the displacement range, respectively. As mentioned above the minimum displacement value was 0mm, but in some specimens, the minimum value was 3mm or 6mm. In that case, "-3" or "-6" are added to the end of the specimen name, such as "C4-12-3" (root size: 4mm, displacement range: 12mm, minimum displacement: 3mm)

Table 3.3 Test conditions

Specimen series		C0			C4					C8		
Size of weld root face in design (mm)		0			4					8		
Applied displacement (mm)	Range.	12	15	18	12	15	18	12	12	12	15	18
	Max.	12	15	18	12	15	18	15	18	12	15	18
	Min.	0	0	0	0	0	0	3	6	0	0	0

3.3 Experimental results

3.3.1 Load-displacement hysteresis loops

Fig. 3.5 shows examples of the load-displacement hysteresis loops, in case of 18mm displacement range. Please see appendix for the results of other displacement cases. The abscissa represents the displacement of the devices, whereas the ordinate indicates the load. **Fig. 3.6** represents the relationship between changes of the maximum load at each loop and the number of cycles. The ordinate is the load normalized by the maximum load at the initial cycle. From these graphs, it was found that the maximum load decreases as the number of cycles increases. The load drops were caused by crack initiation and propagation due to the cyclic loading. These results indicate that the crack initiates in early cycles, and that crack propagation is dominant over the total fatigue life of the specimen.
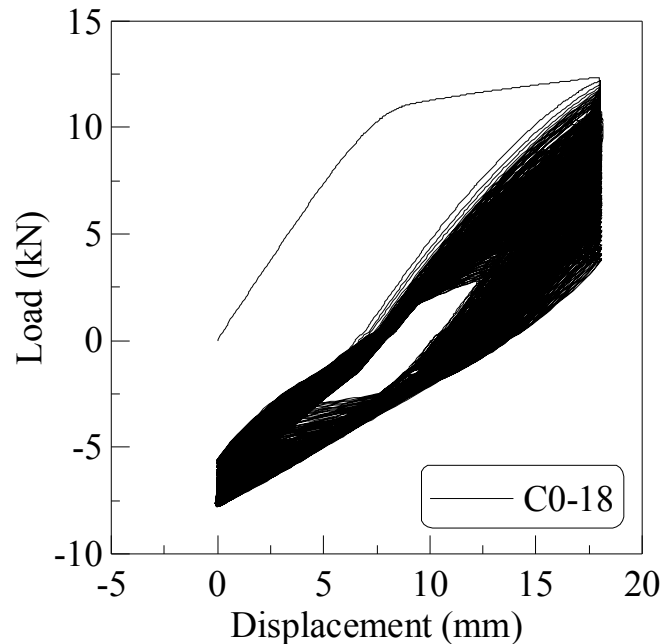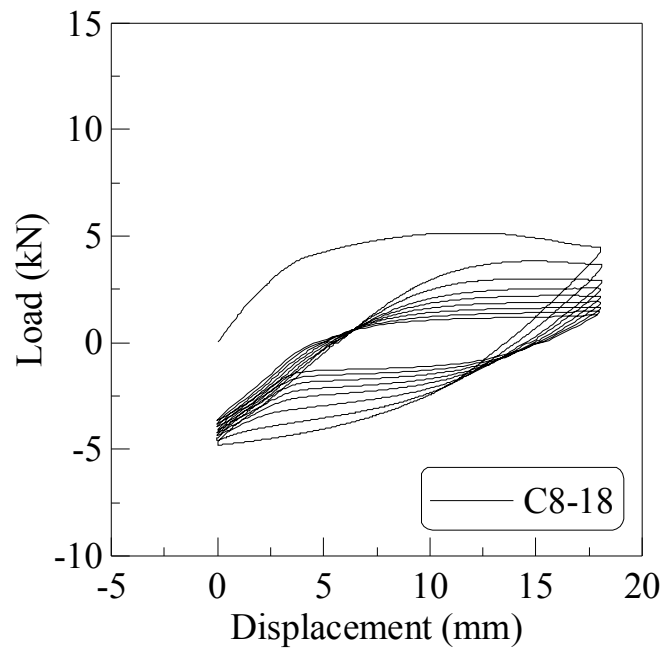

a) C0-18

Fig. 3.5 Load – displacement hysteresis loops
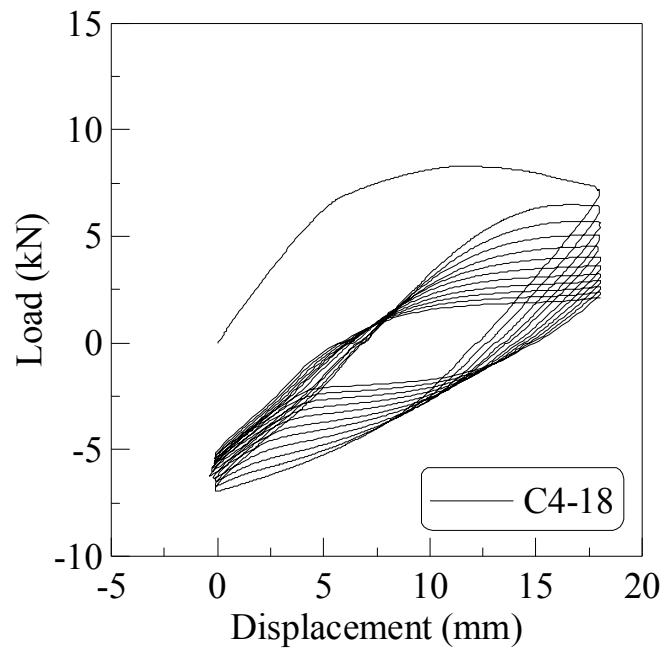
b) C4-18

c) C8-18

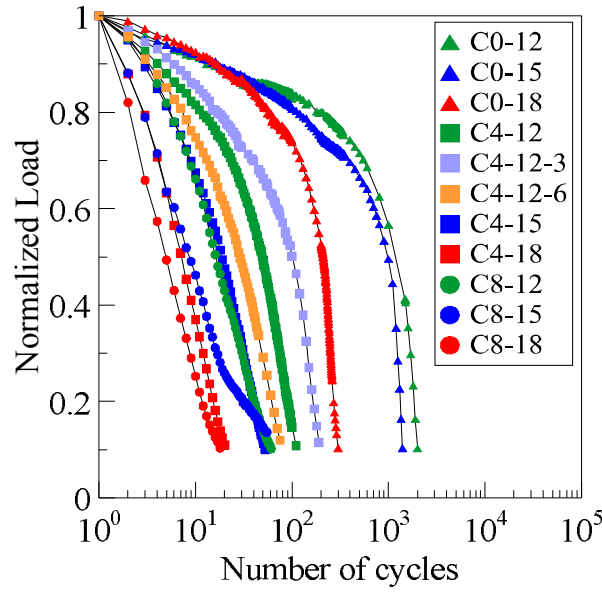**Fig. 3.5** Load – displacement hysteresis loops (Continued)

48

Fig. 3.6 Relationships between maximum loads at each loop and number of cycles

3.3.2 Crack initiation and propagation

Fig. 3.7 shows the crack initiation and propagation behavior observed at the side surface of the C0-12 and C4-12 specimens. The small crack was first detected at the weld root tip, and the crack gradually propagated to the thickness direction with the loading repetitions. **Fig. 3.8** shows photos taken at the side surface of the ruptured specimens and their illustrations. The failure patterns of C0 specimens are different from those in C4 and C8 specimens. In the C0 specimen, the crack propagated through the base metal, while it went through the boundary between the base metal and deposited metal in the C4 and C8 specimens. The failure patterns may be related to the locations of maximum strain around weld root, which are different between C0 specimen and the others. Strain distributions around weld root will be indicated by finite element analyses in the following chapter. Please see appendix for the results of other specimens.

The crack growth curves measured at the side surface of the specimen are shown in **Fig. 3.9**. In the graphs, the crack length includes the size of the weld root face. The crack growth rates in the C0 specimen are lower than those in the other series of specimens. It may be because of the differences of the cracking paths as shown in **Fig. 3.8**.

a) 500 cycles (0.57mm)	b) 1000 cycles (2.93mm)
c) 1700 cycles (8.73mm)	d) 2000 cycles (13.61mm)

a) C0-12

a) 40 cycles (0.67mm)	b) 80 cycles (3.64mm)
c) 120 cycles (6.19mm)	d) 140 cycles (7.21mm)

b) C4-12
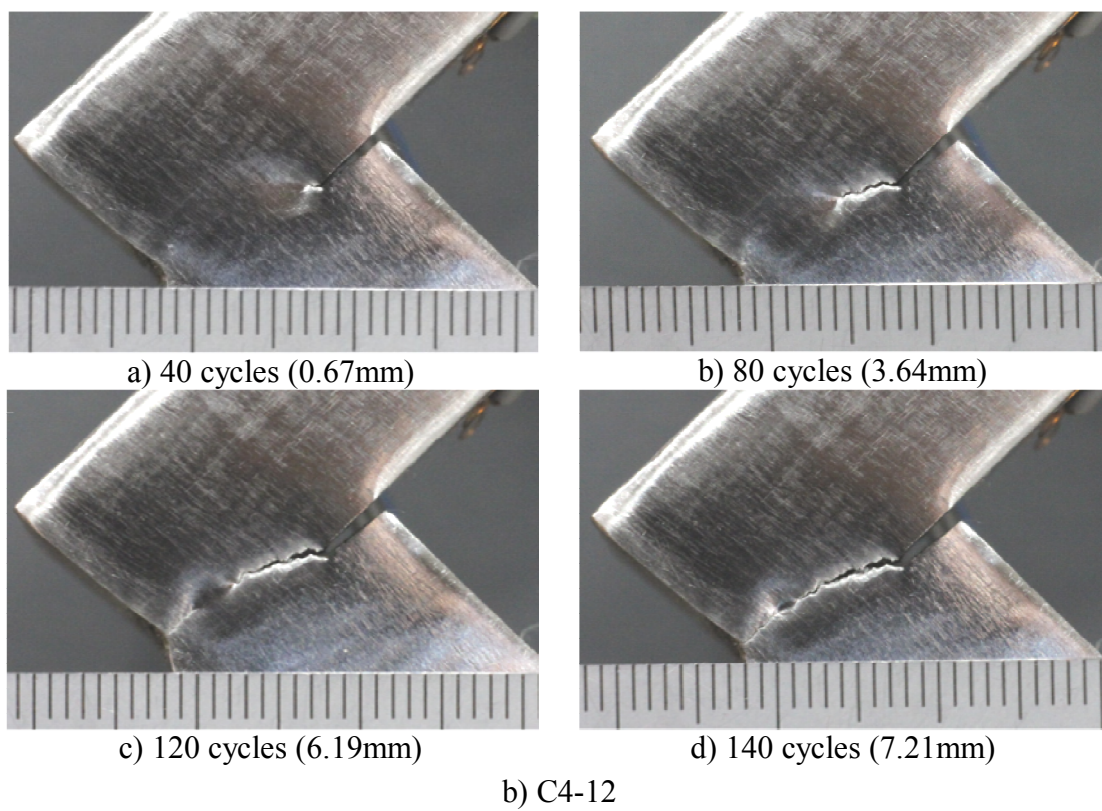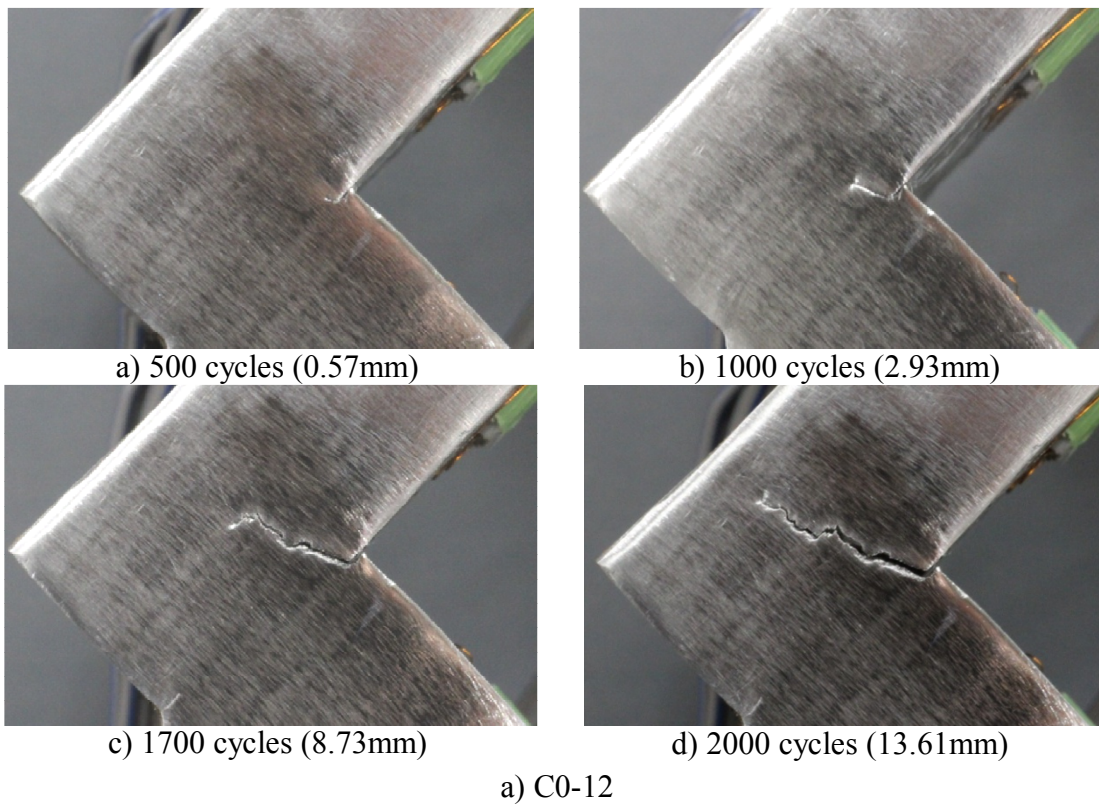
Fig. 3.7 An example of crack propagation behaviors at the side surface of specimen, ( ): crack length
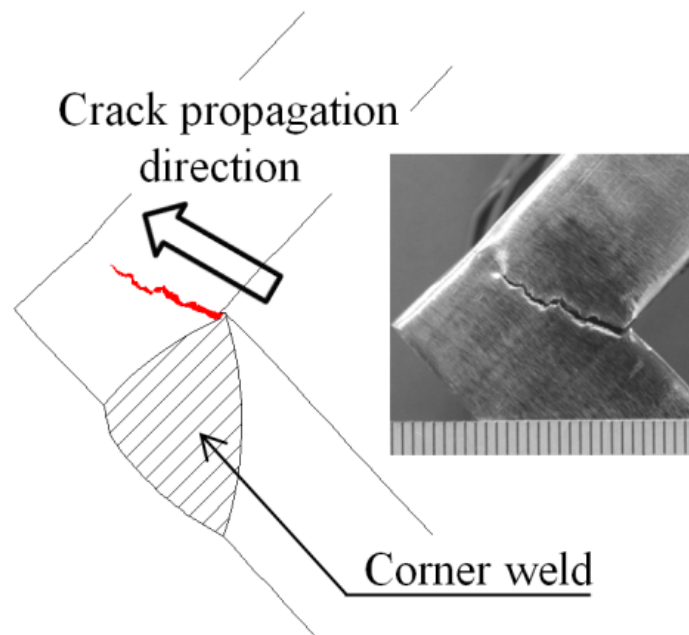
a) C0-12 specimen
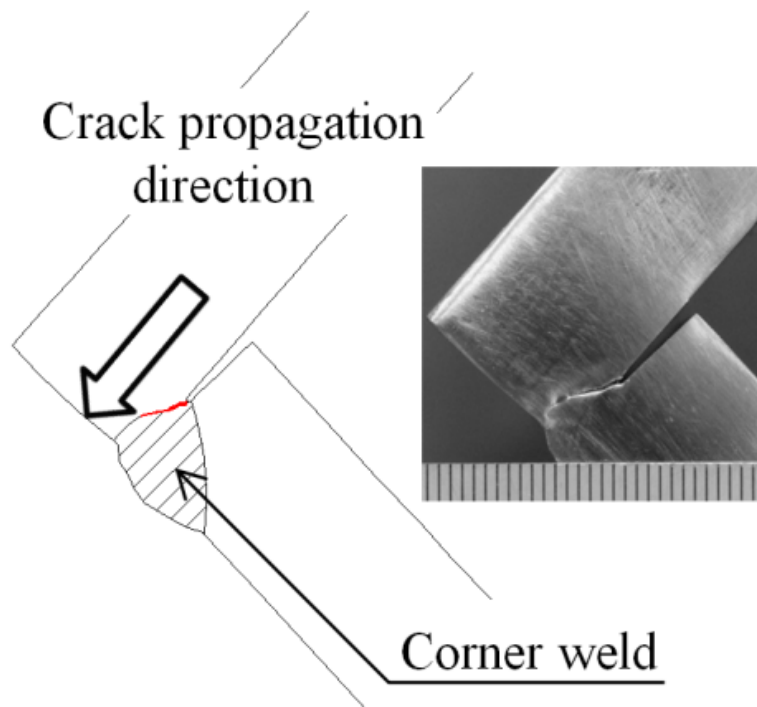
b) C8-12 specimen

Fig. 3.8 Failure paths

a) C0 series specimens

b) C4 series specimens

Fig. 3.9 Relationships between crack length and number of cycles

c) C8 series specimens

Fig. 3.9 Relationships between crack length and number of cycles (Continued)

a) C0-12 specimen

b) C8-12 specimen

Fig. 3.10 Fracture surfaces

Fig. 3.10 shows examples of the fracture surfaces. Uneven surface from the low cycle fatigue crack propagation can be observed. This pattern of the fracture surface is almost the same in all specimens. Please see appendix for the other results.

3.3.3 Definition of low cycle fatigue life

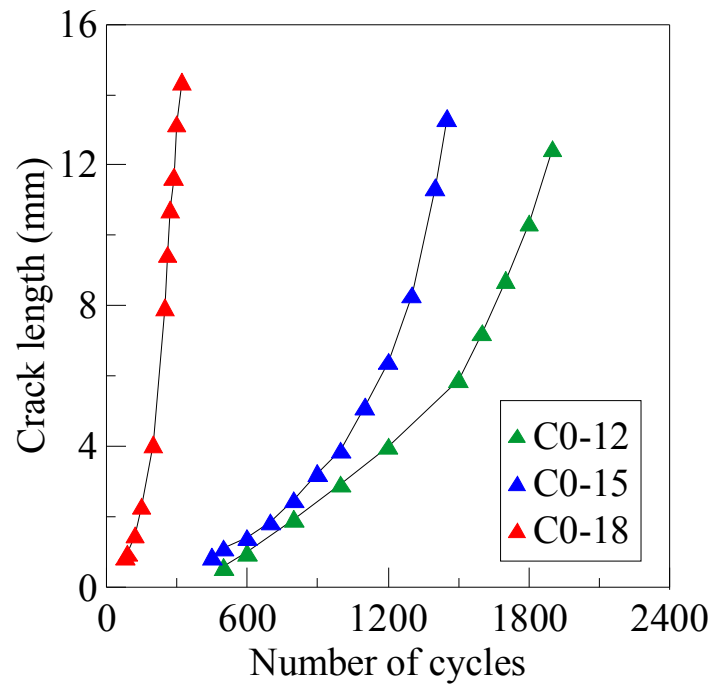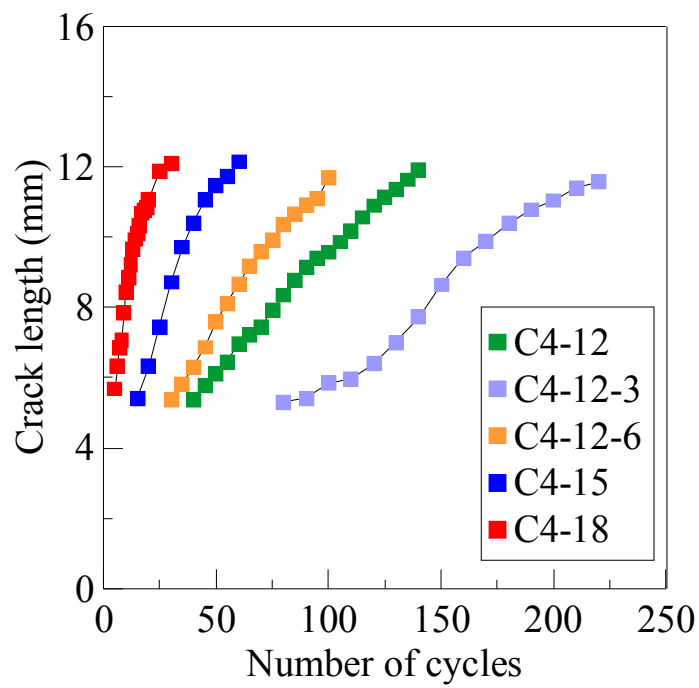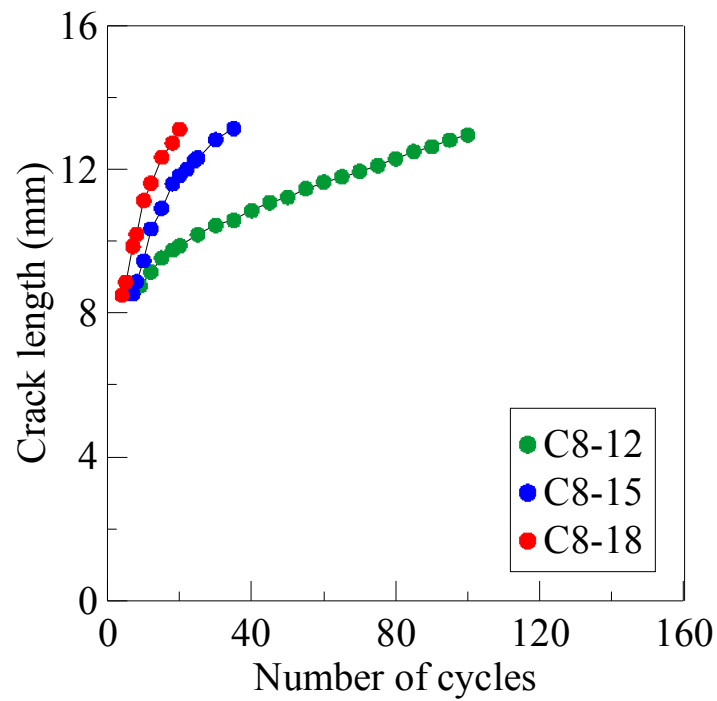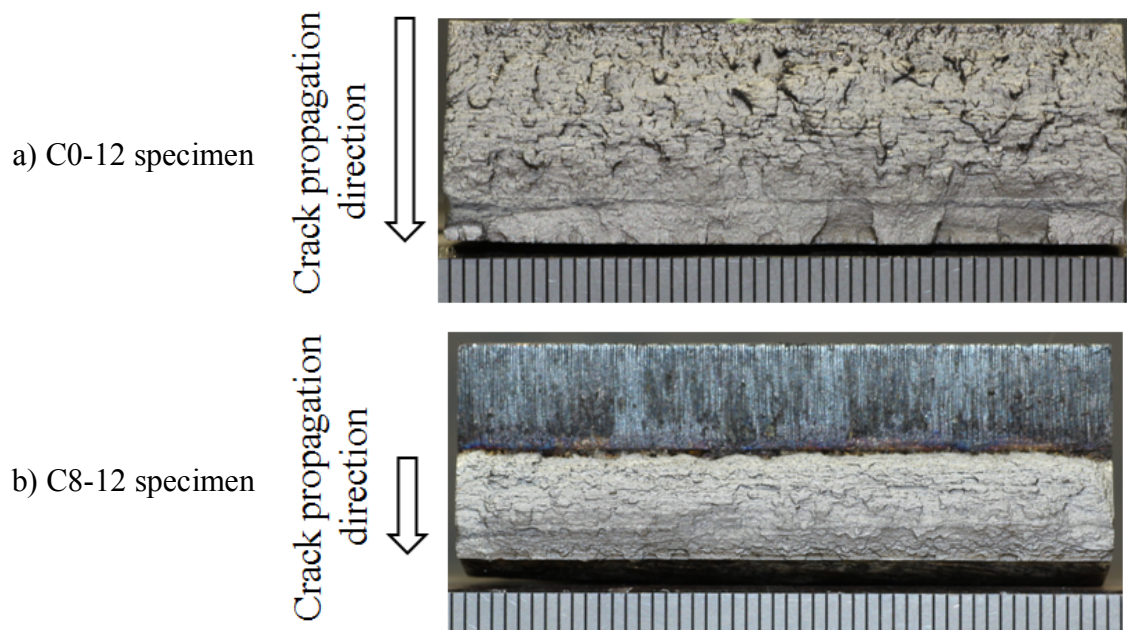As stated above in **Fig. 3.6**, the maximum load continues to decrease with the loading repetition and, especially after approximately a 20~30% load drop, the load tends to decrease rapidly. Here, the crack length inside of the specimen was measured with C0-15 specimen.

The test was stopped at the 20% load drop. After that, cyclic loading in elastic region was applied to the specimen to mark the location of the crack tip. Then, the specimen was broken by monotonic loading. The fracture surface obtained by the procedure mentioned above is shown in **Fig. 3.11**. It can be observed in the picture that the low cycle fatigue crack first occurs inside of the specimen. The crack lengths are approximately from 1.03mm to 2.07mm. Generally in low cycle fatigue region, crack initiation life is considered in relation to local strain at cracking point, which is defined as the number of cycles when crack length is about 0.3mm to 1.0mm as technical size in structure components (Iida et. al., 1977; Nakagomi et. al., 1995; Nihei. et al., 1984; Tateishi et. al., 2004). Therefore, the low cycle fatigue life of the corner welded joints in this study was defined as the number of cycles to 20% load drop.
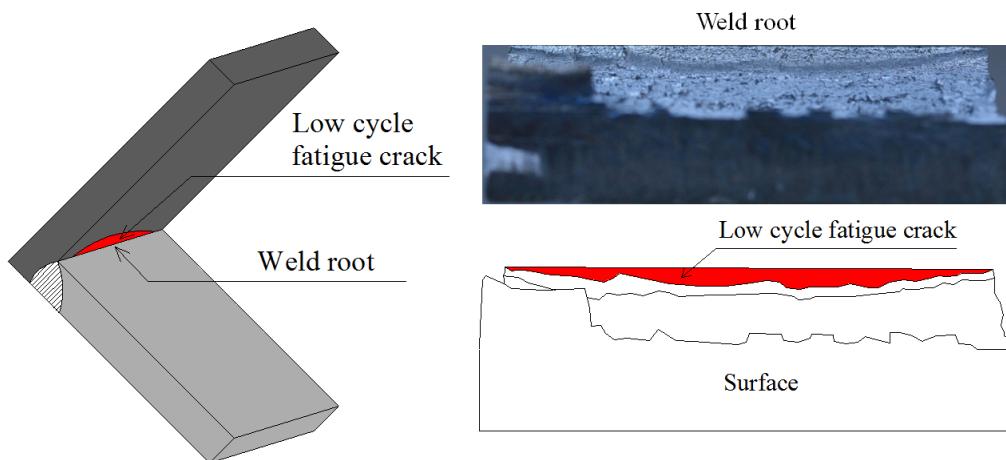
Fig. 3.11 Fracture surface at 20% load drop (C0-15)

3.3.4 Fatigue lives

The relationships between the displacement range applied to the specimen and the fatigue life are shown in **Fig. 3.12**. As defined above, the fatigue life is the number of cycles when the maximum load drops by 20%. The specimens with enough weld penetration (the actual weld root size is about 1mm) have significantly longer fatigue life than others. Besides, there is small effect of the mean strain on the fatigue life of the joint compared to that of the weld root size. Therefore, it is indicated that the low cycle fatigue strength of the corner welded joints strongly depends on the size of the weld root face.

Fig. 3.12 Relationships between displacement and number of cycles

3.4 Effective notch strain based fatigue assessment

3.4.1 Analysis methods

Elasto-plastic finite element analyses were conducted by using ABAQUS program under the same condition of the experiment to investigate strain distributions around a weld root tip in the specimen. **Fig. 3.13** shows an e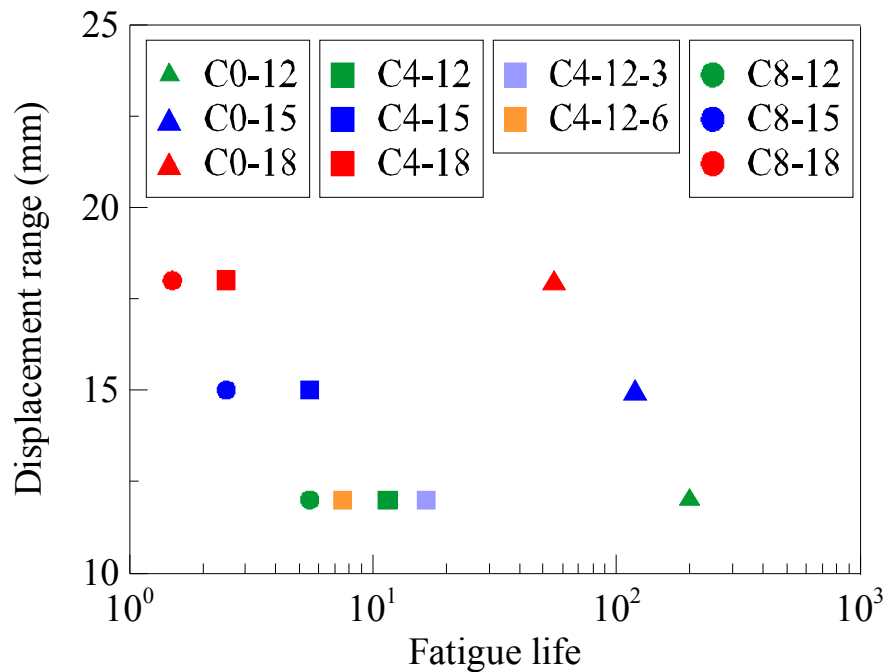xample of FE model and its boundary condition. Two-dimensional analyses under the plane stain assumption were performed. The loading devices were also modeled and assumed to be completely fixed to the specimen.

The weld root tip was modeled as shown in **Fig. 3.13**. Two types of effective notch with a radius (R) of 0.3mm and 1.0mm were adopted at the tip so that different radii can be used depending on plate thickness. The tip of the effective notch radius is located in the position of the root tip in C4 and C8 specimens, while it is located in the intersection of two plates in C0 specimen. The minimum element sizes 1/20 of the notch radius (0.015mm and 0.05mm, respectively) were used around the notch, which satisfies the IIW recommendation (Hobbacher, 2008).

The base metal region, the deposit metal (DM) region and the heat affected zone (HAZ) were modeled individually, as shown in **Fig. 3.13**. Based on the measurement of the weld profiles shown in **Table 3.2** and the precious study (Gunaraj et al., 2002), the sizes of the DM region and HAZ were determined. As for the size of the HAZ, it was set to be constant of 1mm.

In this analysis, different stress-strain curves were assigned to each region. The true stress-strain relationships of each material (base metal, DM and HAZ) are shown in **Fig. 3.14**. The DM and HAZ are assumed to have 20% higher yielding strength than the base metal (Dražan et al., 2002). In all materials, Young's modulus and Poisson's ratio were $2.0 \times 10^5 \text{N/mm}^2$ and 0.3, respectively.

The combined isotropic and kinematic hardening model with the von Mises yield surface was used. Cyclic displacements were applied to the bottom device. Crack initiation and propagation were not considered in this analysis.
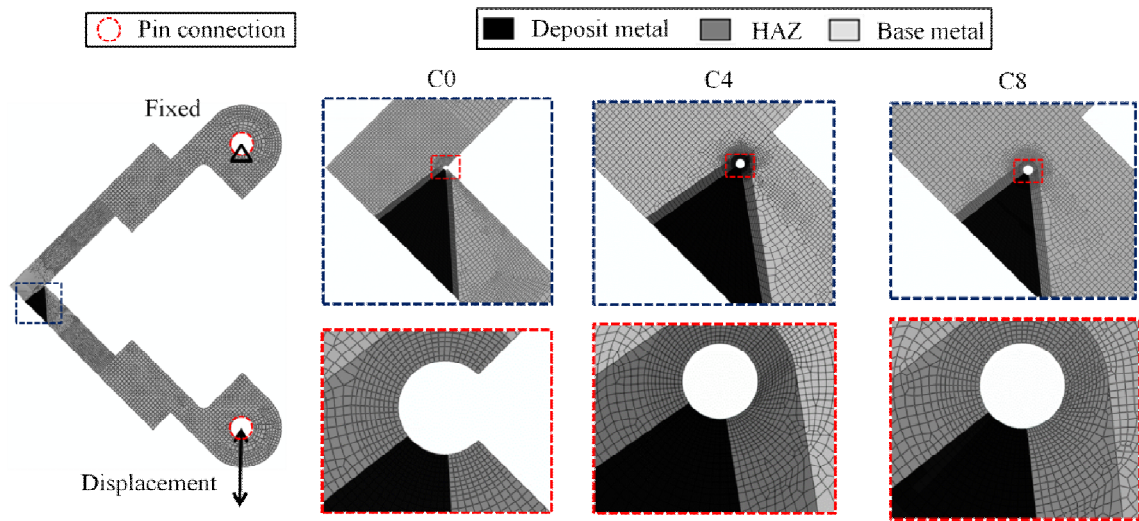
a) 1.0mm radius of effective notch
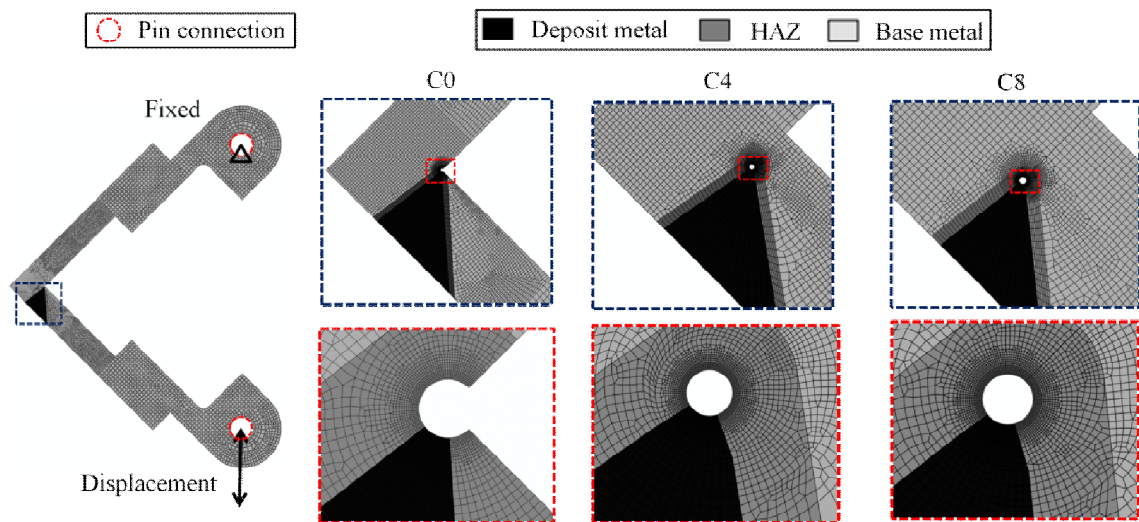
b) 0.3mm radius of effective notch

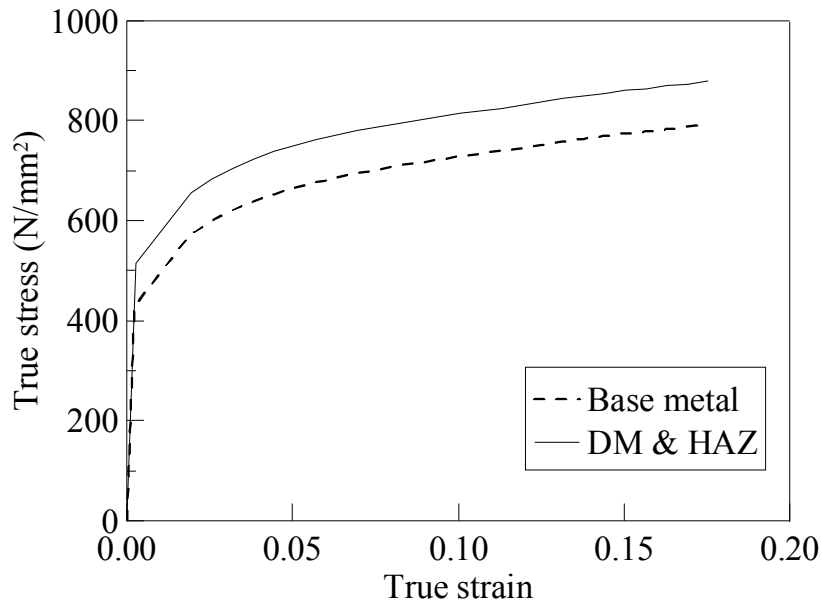**Fig. 3.13** Finite element model

Fig. 3.14 Stress-strain relationships

3.4.2 Load – displacement relationship

Fig. 3.15 shows an example of a comparison of hysteresis loops between the analysis and the experiment. Relatively good agreement was obtained, meaning that the effective notch and the notch size hardly affects to the global behavior of the model. In **Fig. 3.16**, strains in the analysis were compared with those measured by strain gauges attached to the specimen as shown in **Fig. 3.3**. The strains shown in the analysis are in agreement with the measurements. Therefore, these comparisons indicated that the finite element modeling can accurately represent the behaviors of the specimen.

3.4.3 Strain distributions around weld root tip

In **Fig. 3.17** and **Fig. 3.18**, equivalent plastic strain distributions around the effective notch are shown when the maximum tensile displacement was applied. High strain concentration can be observed around the effective notch. The locations of the highest strain are different depending on the size of the root face, which are almost consistent with the direction of cracking in the specimens.
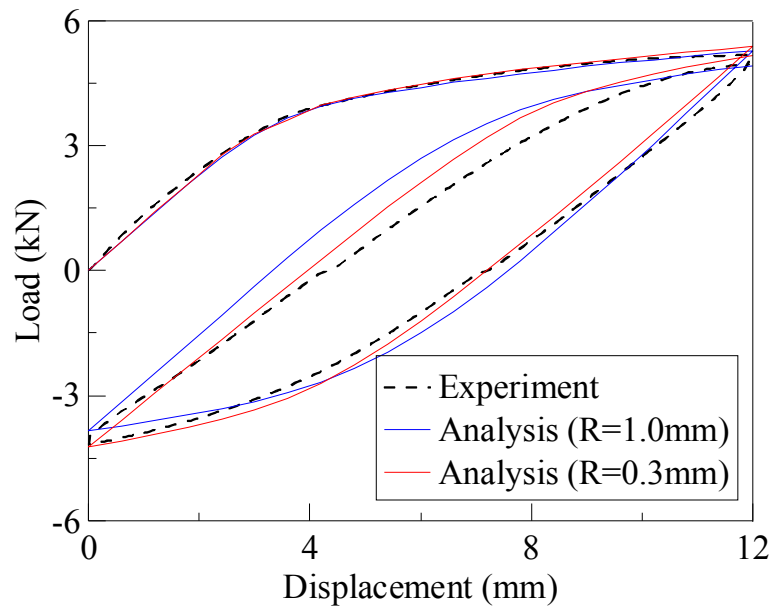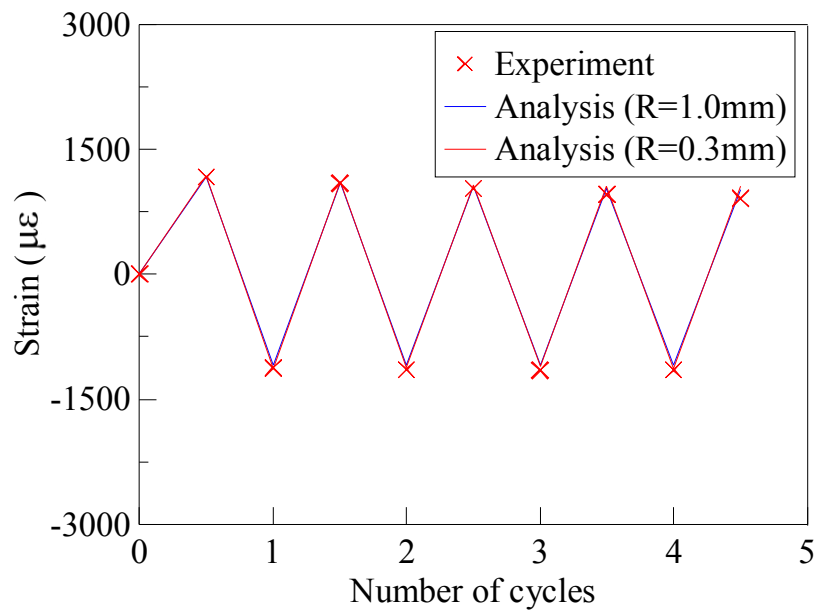
58

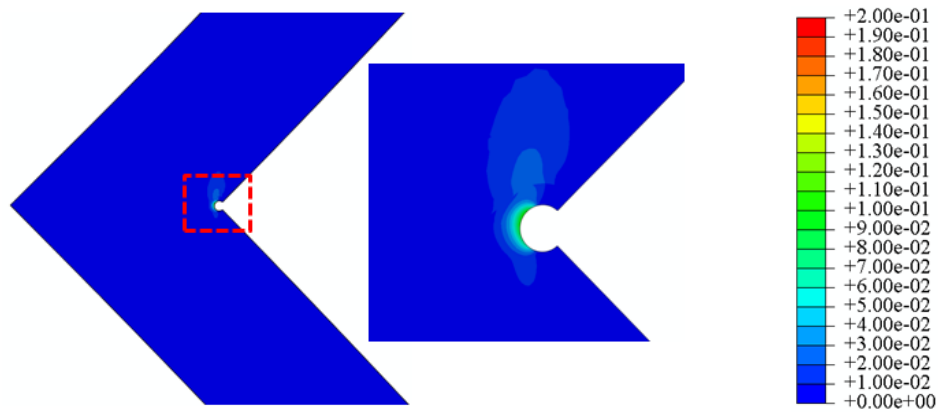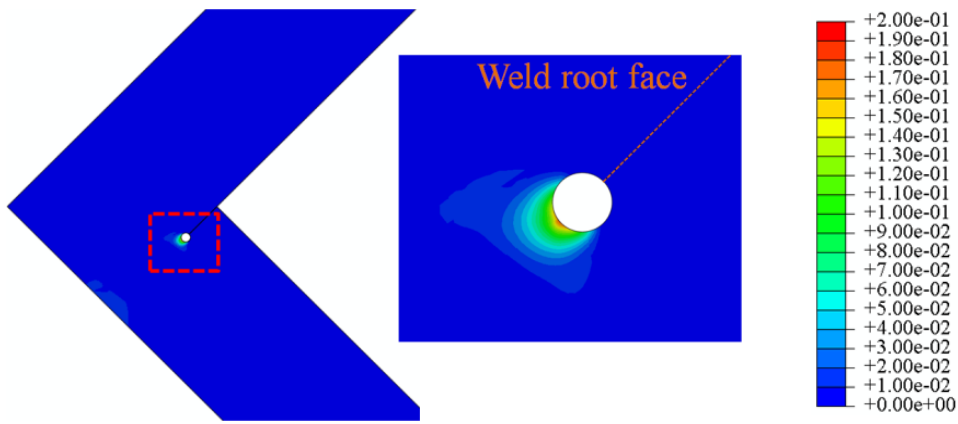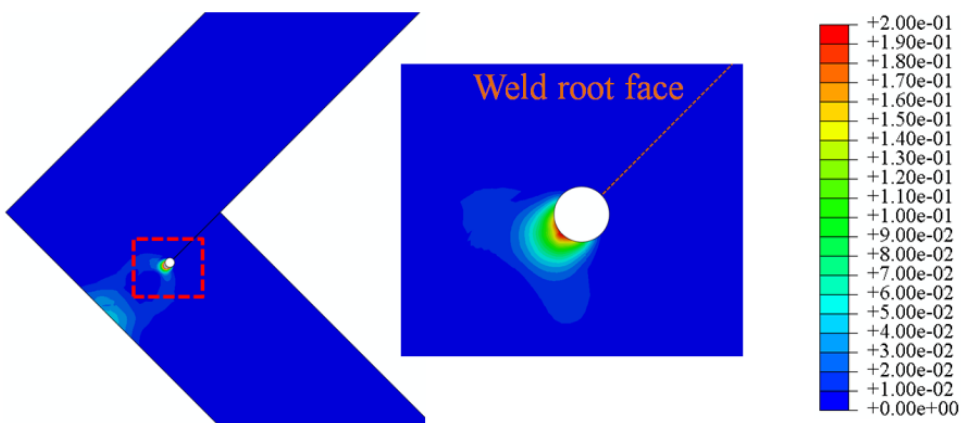**Fig. 3.15** Comparison of load-displacement relationships (C8-12)

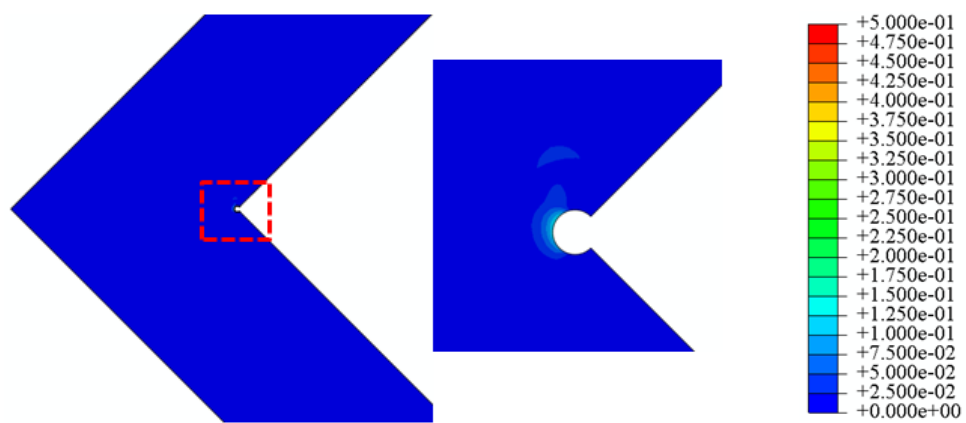**Fig. 3.16** Strain history relationship (C8-12)

a) C0-18

b) C4-18
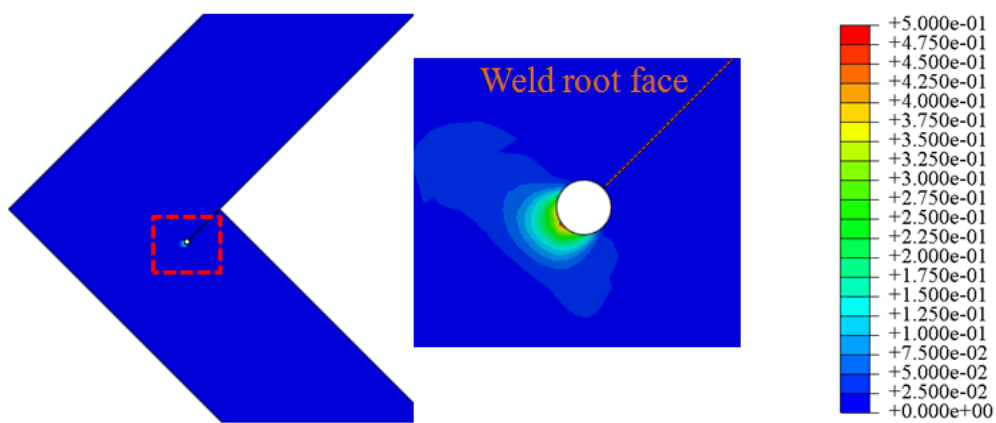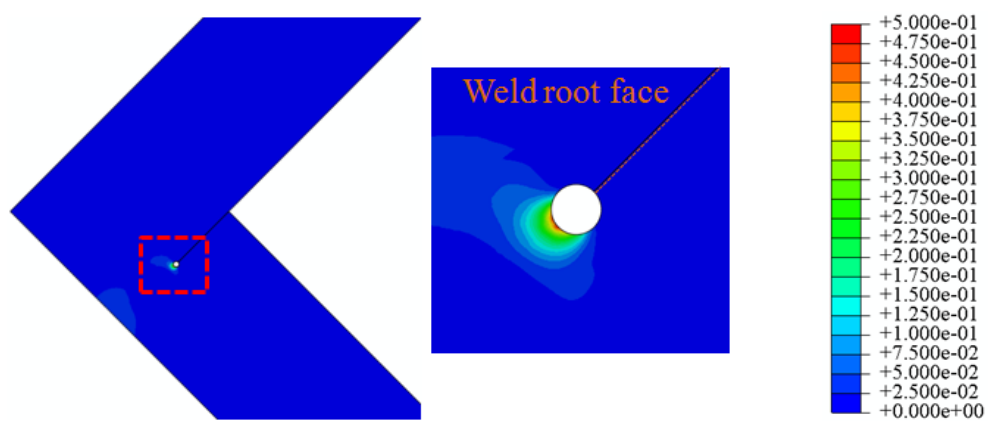

c) C8-18

Fig. 3.17 Equivalent plastic strain distributions around weld root tip (R=1.0mm)

a) C0-18

b) C4-18

c) C8-18

Fig. 3.18 Equivalent plastic strain distributions around weld root tip (R=0.3mm)

3.4.4 Calculation method of effective notch strain range

The range of effective notch strain was obtained from the elastic and plastic equivalent strain in elements along the effective notch in elasto-plastic finite element analysis. The effective notch strain range was defined as the summation of the elastic and plastic equivalent strains, as illustrated in **Fig. 3.19** and given in equation (3-1). The elastic and plastic component can be calculated by in equation (3-2) ~ (3-3).
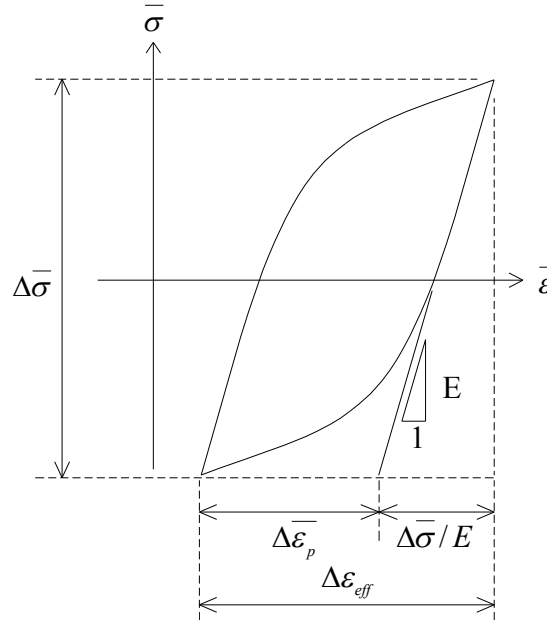
Fig. 3.19 Definition of effective strain range

$$\Delta \varepsilon_{eff} = \frac{\Delta \overline{\sigma}}{E} + \Delta \overline{\varepsilon}_p \qquad (3\text{-}1)$$

$$\overline{\sigma} = \sqrt{\frac{1}{2}[(\Delta\sigma_x - \Delta\sigma_y)^2 + (\Delta\sigma_y - \Delta\sigma_z)^2 + (\Delta\sigma_z - \Delta\sigma_x)^2 + 6(\Delta\tau_{xy}^2 + \Delta\tau_{yz}^2 + \Delta\tau_{zx}^2)]} \qquad (3\text{-}2)$$

$$\overline{\varepsilon}_p = \frac{1}{3} \times \sqrt{2\left[\left(\Delta\varepsilon_{p,x} - \Delta\varepsilon_{p,y}\right)^2 + \left(\Delta\varepsilon_{p,y} - \Delta\varepsilon_{p,z}\right)^2 + \left(\Delta\varepsilon_{p,z} - \Delta\varepsilon_{p,x}\right)^2 + \frac{3}{2}\left(\Delta\gamma_{p,xy}^2 + \Delta\gamma_{p,yz}^2 + \Delta\gamma_{p,zx}^2\right)\right]} \qquad (3\text{-}3)$$

where $\Delta\varepsilon_{eff}$ is the effective notch strain range, $\Delta\overline{\sigma}$ is the equivalent stress range, $\Delta\overline{\varepsilon}_p$ is the equivalent plastic strain range, E is Young's modulus, $\Delta\sigma$ is the normal stress range, $\Delta\tau$ is the shear stress range, $\Delta\varepsilon_p$ is the normal plastic strain range, $\Delta\gamma_p$ is the shear plastic strain range, the subscripts x, y and z are the x, y and z directions, respectively.

3.4.5 Fatigue assessment by effective notch strain

Fig. 3.20 shows the relationship between the effective notch strain range by equation (3-1) and the fatigue life of the specimens. The effective notch strain ranges were calculated along the effective notch and their maximum value was used for arranging the results. As mentioned above, the fatigue life of the specimen was defined as the number of cycles to 20% load drop. In **Fig. 3.20(a)**, the relationship between the effective notch strain range (R=1.0mm) and the fatigue life obtained for load-carrying cruciform welded joints (Saiprasertkit et al., 2012) is also shown with a solid curve and equation (3-4).

In **Fig. 3.20(a)**, regardless of the size of the weld root face, all test results distribute in the same region when arranging with the effective notch strain. Furthermore, the results locate around the curve for load-carrying cruciform joints, meaning that a unique relationship can be obtained regardless of the joint configurations. Therefore, it is concluded that the low cycle fatigue strength of corner welded joints can be evaluated by using the effective notch strain range with the unique fatigue strength curve.

When applying the effective notch of 0.3mm radius shown in **Fig. 3.20(b)**, the results also locate within a relatively narrow range regardless of the weld root size. The magnitude of the strain in case of R=0.3mm is higher than R=1.0mm, however, the slopes of the results are similar in both cases. Therefore, this study proposed the relationships between the effective notch strain range and the fatigue life, of which slope is constant regardless of the notch radius. The proposed relationships are in equation (3-5), which is calculated by fitting method using the same slope in case of the fatigue strength curve (R=1.0mm). The fatigue strength curves agree with the test result, as shown in **Fig. 3.20**.

$$\Delta\varepsilon_{eff} \cdot N^{0.313} = 0.1847 \quad \text{(R=1.0mm)} \qquad (3\text{-}4)$$

$$\Delta\varepsilon_{eff} \cdot N^{0.313} = 0.3034 \quad \text{(R=0.3mm)} \qquad (3\text{-}5)$$

63
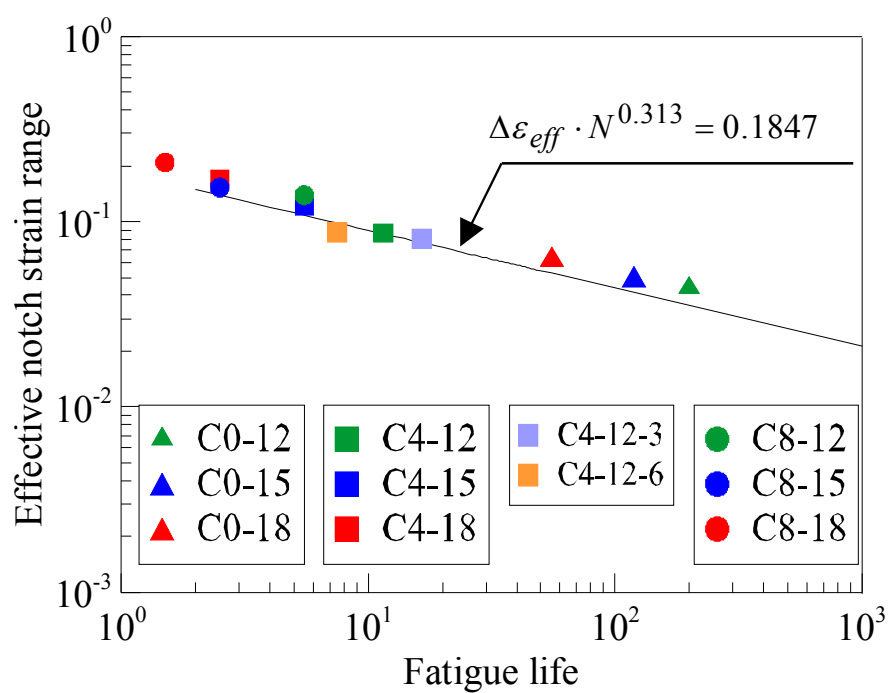
a) 1.0mm radius of effective notch
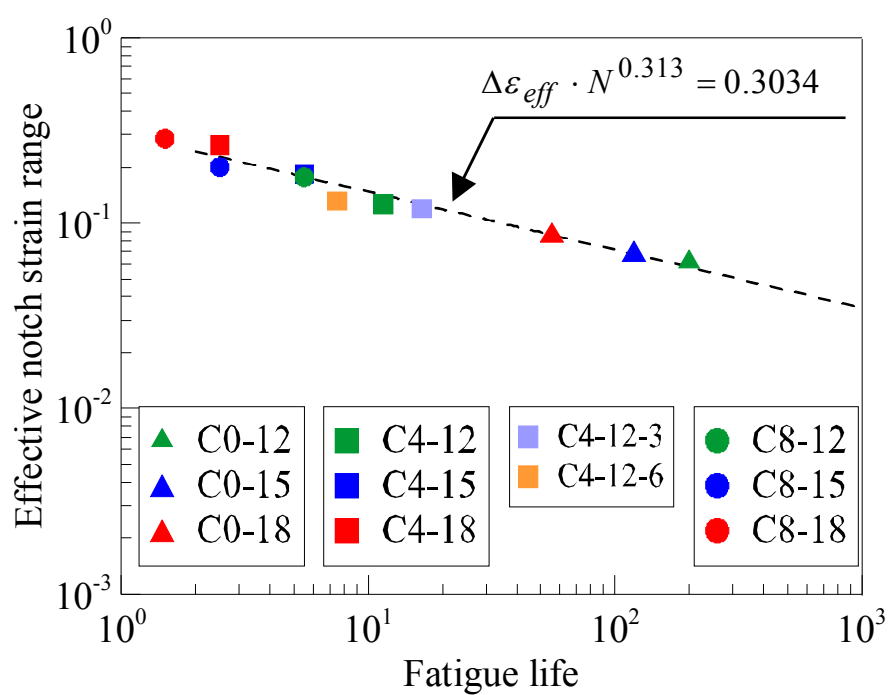
b) 0.3mm radius of effective notch

Fig. 3.20 Fatigue assessment by effective notch strain range

3.5 Concluding remarks

In this chapter, the extremely low cycle fatigue strengths of corner welded joints with single bevel welding were investigated. Fatigue tests were performed with three types of specimens which have different sizes of weld root face. Then, fatigue assessments of corner welded joints in the extremely low cycle fatigue regions were performed based on the effective notch strain approach.

The main conclusions can be drawn as follows:

1) In all specimens, low cycle fatigue cracks were initiated from a tip of weld root. Fatigue cracks occurred in early cycles, and their propagation was dominant over total fatigue life of the specimens.

2) Low cycle fatigue strength of corner welded joints strongly depended on the size of the weld root faces.

3) Local strain at the root tip was calculated by applying the effective notch concept, where it is called the effective notch strain

4) When arranging the test results with the effective notch strain range, a unique fatigue strength curve could be observed regardless of the weld root size and the joint configuration.

5) Based on the results, this study proposed the fatigue strength curve for the corner welded joint based on the effective notch strain.

CHAPTER 4

EXTRMELY LOW CYCLE FATIGUE ASSESSMENTS FOR CONCRETE-FILLED STEEL BRIDGE PIERS

4.1 Introduction

In the previous chapter, it was demonstrated that the low cycle fatigue strength of corner welded joints could be evaluated by comparing the effective notch strain range with the proposed fatigue strength curve. This chapter investigated the applicability of the proposed method to concrete-filled steel piers.

Finite element analyses with the sub-modeling technique were conducted to obtain the effective notch strain range around cracking sites in the concrete-filled steel piers specimen shown in Chapter 2. By comparing the effective notch strain to the fatigue strength curve, fatigue life of the specimen was estimated. Based on the results, the validity of the proposed fatigue assessment method was confirmed.

4.2 Finite element analyses

4.2.1 Analysis methods

In order to introduce the effective notch strain approach to concrete-filled steel piers, the sub-modeling technique was employed. In the sub-modeling technique, the result obtained from a global model is applied to a sub-model as displacement boundary conditions. **Fig 4.1** illustrates the FE models. As for the global model, the concrete-filled steel piers model which was mentioned in Chapter 2 was used. In the global model, the corner weld around the cracking site was created by solid elements with coarse meshing. The same part was modeled as the sub-model with fine meshing as shown in the figure. Effective notch with a radius (R) of 0.3mm was introduced at the

root tip in the sub-model. In the sub-model, the tip of the effective notch radius matches the root tip of the specimen. The minimum size along the notch was 0.015mm, which satisfies the IIW recommendation (Hobbacher, 2008).
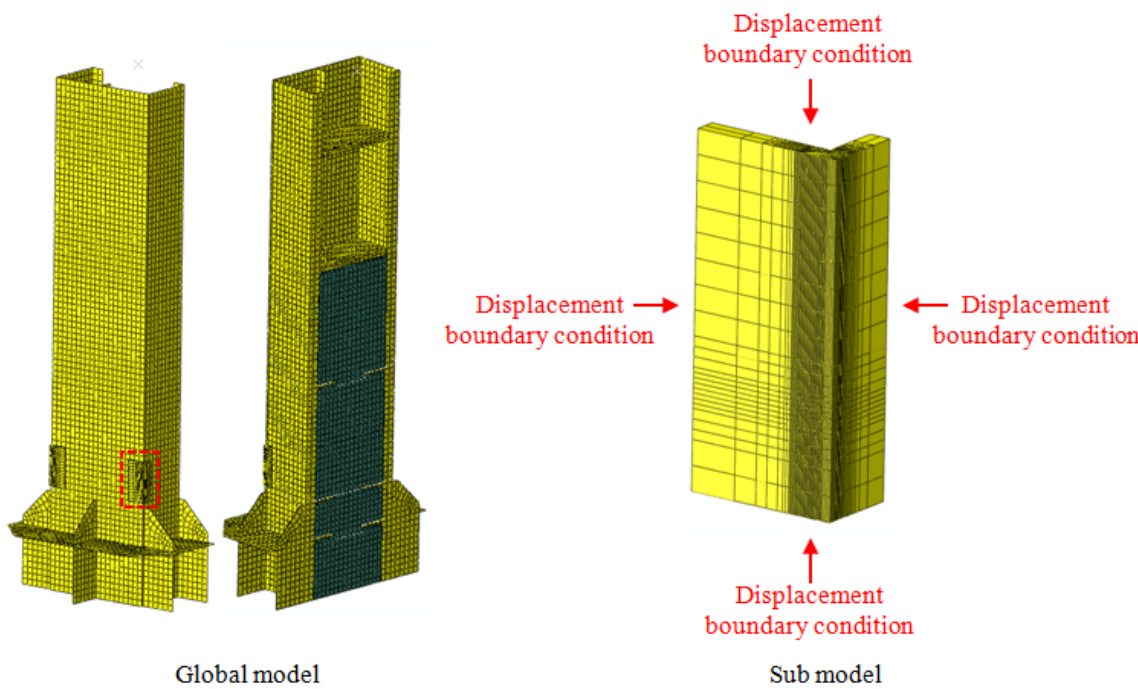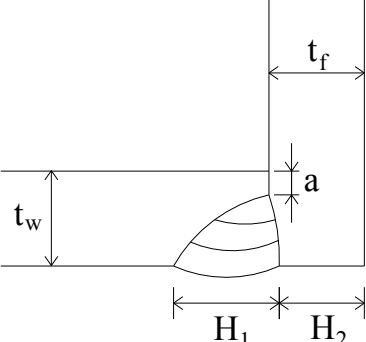
Fig. 4.1 Illustration of FE model

Table 4.1 weld profiles of corner welded joints

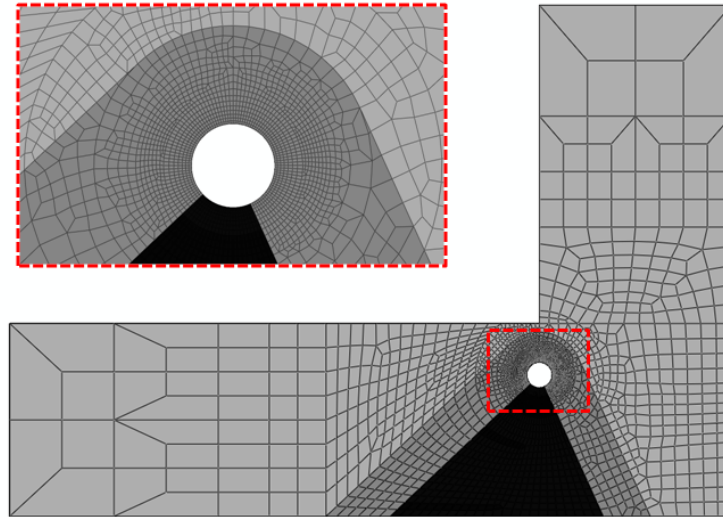| t_f (mm)	t_w (mm)	a (mm)	H_1 (mm)	H_2 (mm)
4.5	4.5	1.5	5.0	3.0

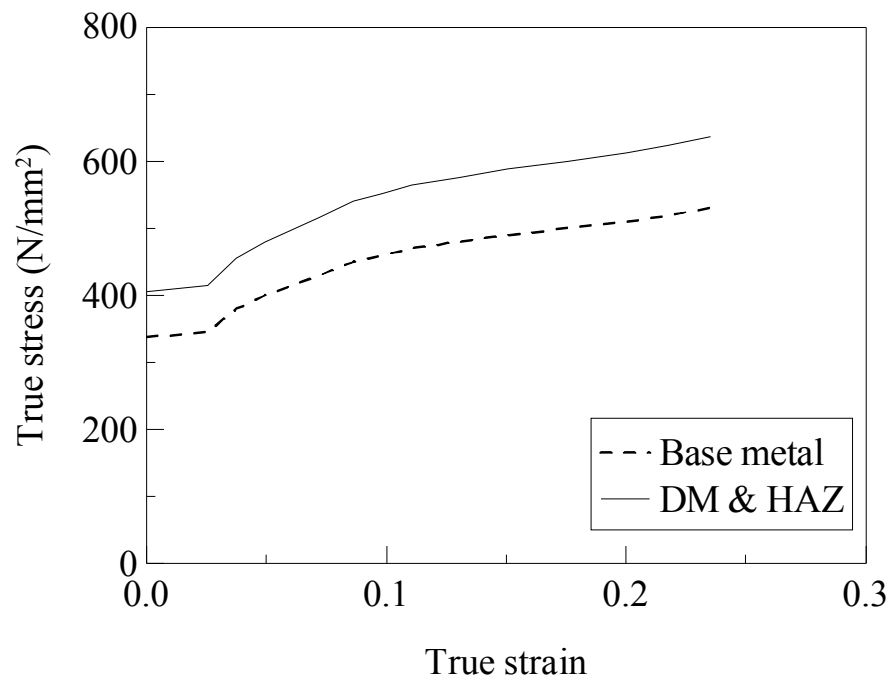**Fig. 4.2** Details of sub-model (effective notch with R=0.3)

Fig. 4.3 Stress-strain relationships

In the sub-model, the base metal, the deposit metal region and the heat affected zone were modeled individually, as shown in **Fig. 4.2**. Based on the measurement of the weld profiles in the concrete-filled specimen shown in **Table 4.1**, the sizes of DM and HAZ were determined. As for the size of the HAZ, it was set to be constant of 1mm.

The true stress-strain relationships of each material are shown in **Fig. 4.3**. The DM and HAZ are assumed to have 20% higher yielding strength than the base metal. The yield strength, Young's modulus and Poisson's ratio are 338N/mm^2, 2.0×10^{5}N/mm^2 and 0.3, respectively.

4.2.2 Verifications of sub-modeling

In order to verify the sub-modeling, the displacement distributions in the sub model were compared with those of the global model. **Fig. 4.4** shows the comparisons of displacement contour between in the global and sub model at 0.25 cycles, 2.25 cycles and 5.25 cycles in case of CF10. The tendency of the displacement of the sub-model is similar with that of the global model. From these results, the validity of the sub-modeling was proved.
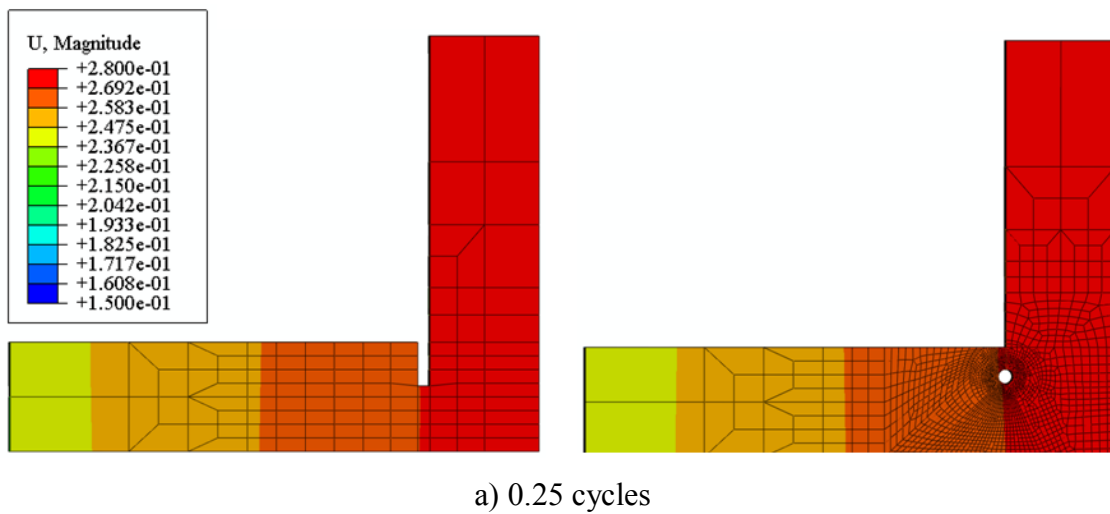
a) 0.25 cycles

Fig. 4.4 Comparison of displacement contour between global and sub model (CF10)
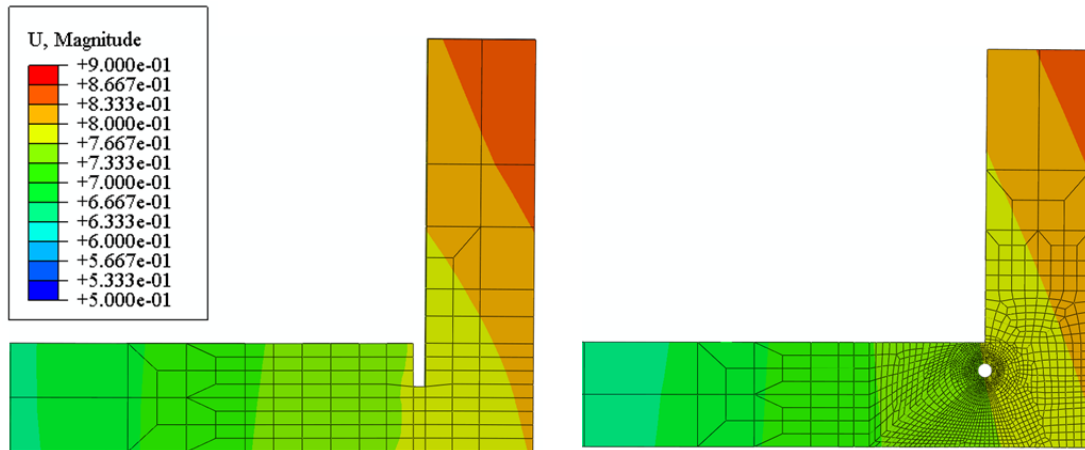
b) 2.25 cycles
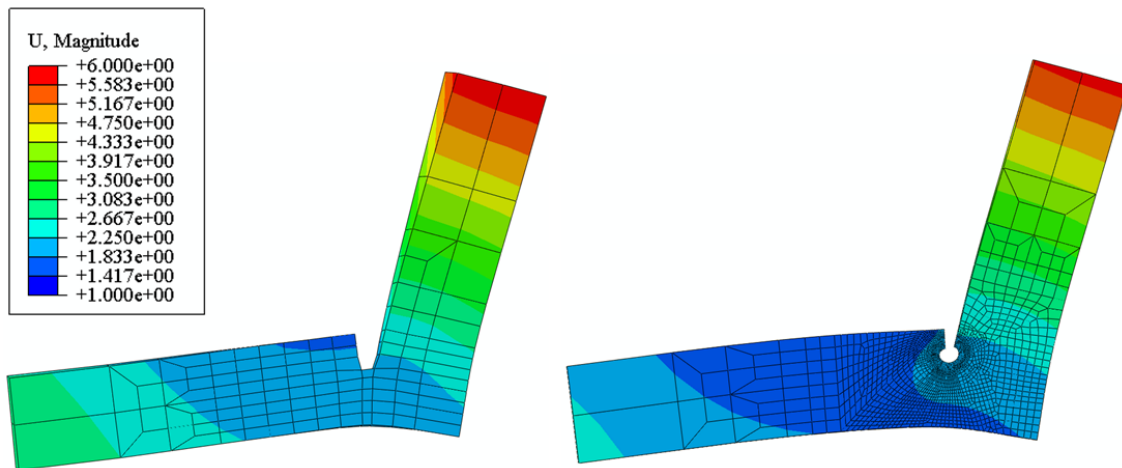
c) 5.25 cycles

Fig. 4.4 Comparison of displacement contour between global and sub model (CF10)

(Continued)

71

4.2.3 Strain distribution around weld root tip

Equivalent plastic strain distributions around the effective notch at 6.25 cycles are shown in **Fig. 4.5**. The scale of the spectrum range is constant in the figures. High strain concentration can be seen around the effective notch. Although the magnitude of the strain around the effective notch differs depending on the axial load level (CF10 and CF20), the difference of strain values is relatively small.
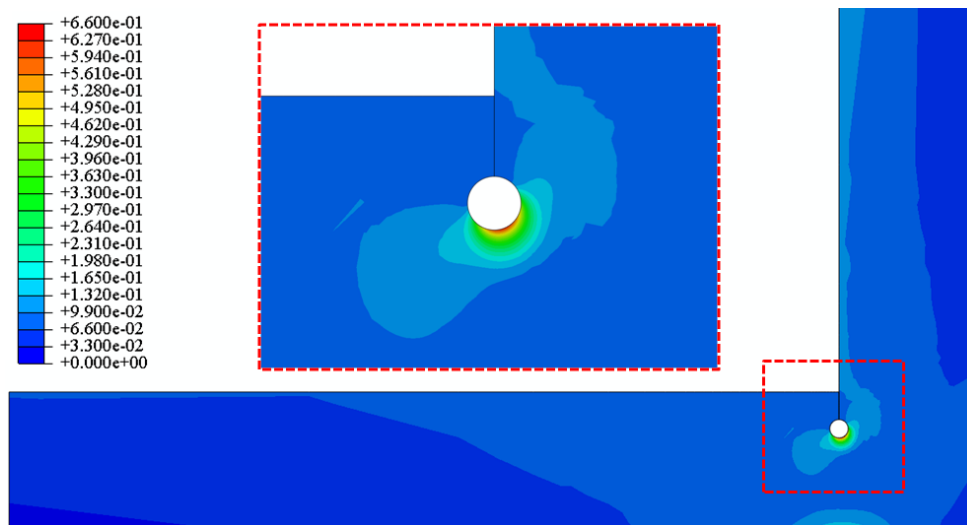
a) CF10
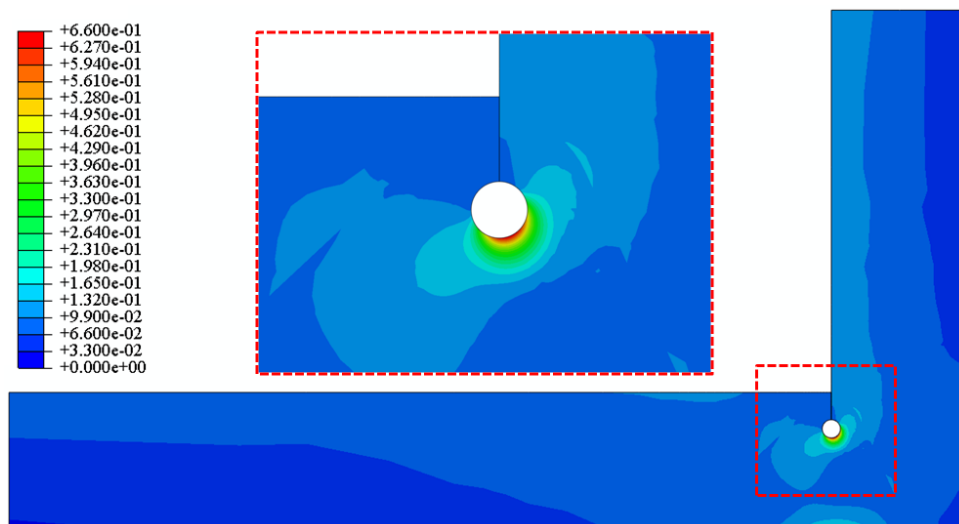
b) CF20

Fig. 4.5 Equivalent plastic strain distributions around weld root tip

4.2.4 Calculation results of effective notch strain range

As stated in Chapter 3, the effective notch strain ranges was calculated by summation of the elastic and plastic equivalent strains. The elastic and plastic components were calculated by in equation (3-1) ~ (3-3).

 Table 4.2 and **Table 4.3** show the calculation results of the effective notch strain range in CF10 and CF20. **Fig. 4.6** shows the relationships between effective notch strain range and the number of cycles. And **Fig. 4.7** shows the displacement histories calculated at the flange and web plates as shown in the figure. The displacement histories gradually increase and, especially after 4.25 cycles, it begins to increase significantly. The tendency of the displacement history is similar with the history of the effective notch strain range. It can be confirmed that the out-of-plane bending deformations of the flange and web causes the rapid increase of the effective notch strain, which can lead to the low cycle fatigue failure.
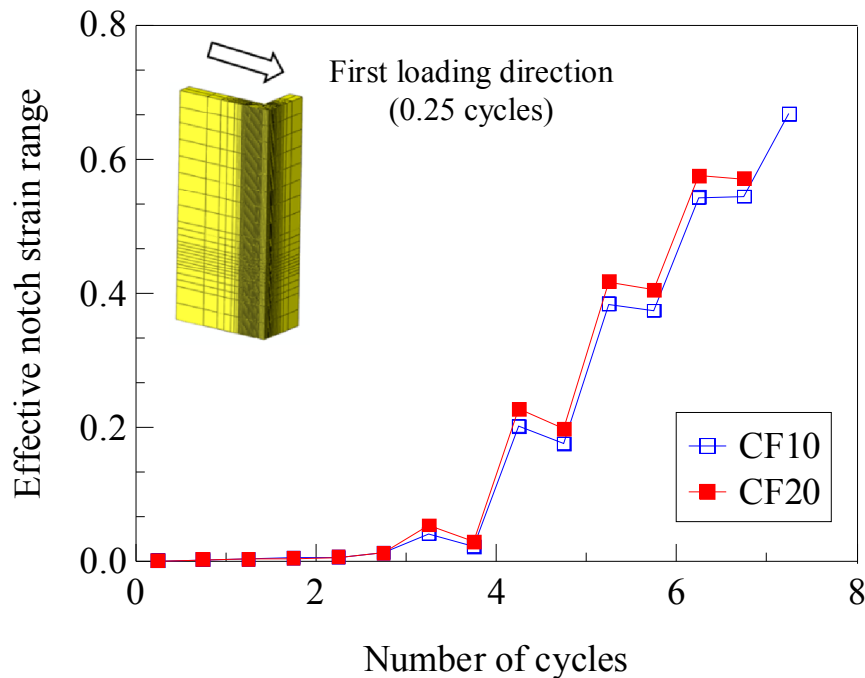

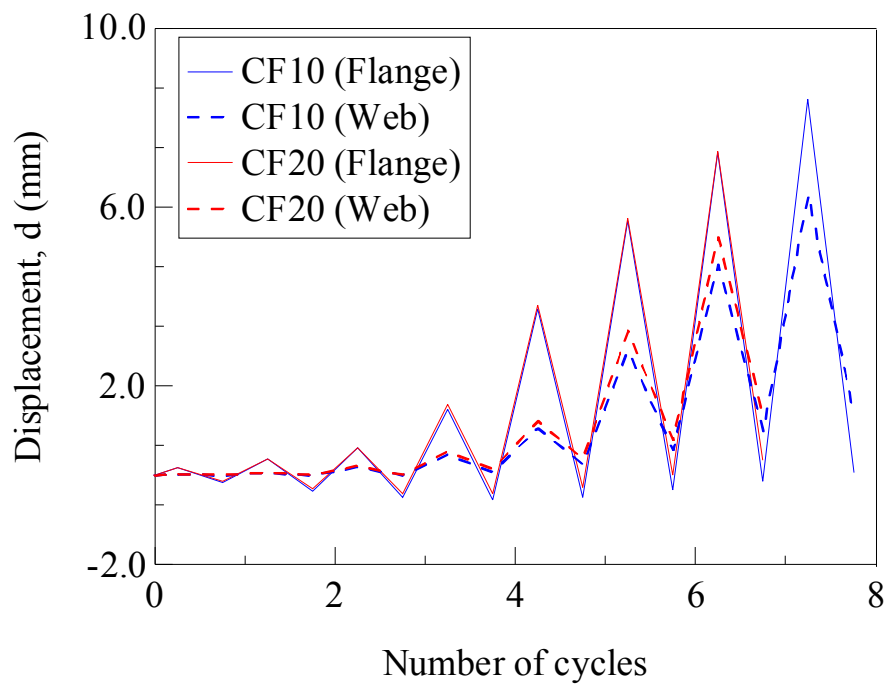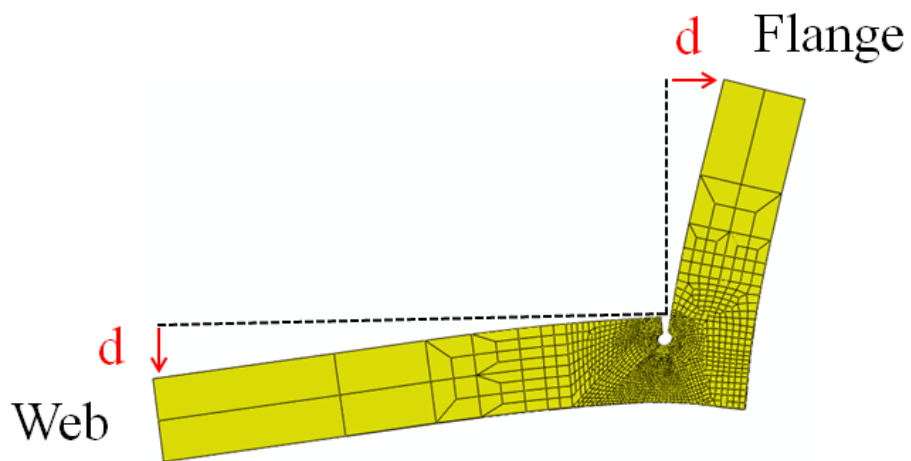**Fig. 4.6** Relationships between effective notch strain range and number of cycles

Fig. 4.7 Displacement histories at the flange and web plates

Table 4.2 Calculation results of effective notch strain range (CF10)

Number of cycles	Equivalent elastic strain	Equivalent plastic strain	Effective notch strain range
0 to 0.25	0.0013	0.0000	0.0013
0.25 to 0.75	0.0029	0.0000	0.0029
0.75 to 1.25	0.0032	0.0004	0.0036
1.25 to 1.75	0.0031	0.0024	0.0055
1.75 to 2.25	0.0030	0.0034	0.0064
2.25 to 2.75	0.0028	0.0104	0.0132
2.75 to 3.25	0.0013	0.0398	0.0411
3.25 to 3.75	0.0015	0.0206	0.0221
3.75 to 4.25	0.0021	0.1996	0.2017
4.25 to 4.75	0.0029	0.1729	0.1758
4.75 to 5.25	0.0039	0.3804	0.3843
5.25 to 5.75	0.0047	0.3693	0.3740
5.75 to 6.25	0.0055	0.5375	0.5430
5.75 to 6.75	0.0058	0.5384	0.5442
6.75 to 7.25	0.0064	0.6609	0.6673

Table 4.3 Calculation results of effective notch strain range (CF20)

Number of cycles	Equivalent elastic strain	Equivalent plastic strain	Effective notch strain range
0 to 0.25	0.0013	0.0000	0.0013
0.25 to 0.75	0.0029	0.0000	0.0029
0.75 to 1.25	0.0030	0.0005	0.0035
1.25 to 1.75	0.0032	0.0017	0.0049
1.75 to 2.25	0.0029	0.0040	0.0069
1.75 to 2.75	0.0026	0.0099	0.0125
2.75 to 3.25	0.0014	0.0529	0.0543
3.25 to 3.75	0.0016	0.0277	0.0293
3.75 to 4.25	0.0024	0.2254	0.2278
4.25 to 4.75	0.0035	0.1947	0.1982
4.75 to 5.25	0.0045	0.4125	0.4170
5.25 to 5.75	0.0053	0.3995	0.4048
5.75 to 6.25	0.0062	0.5690	0.5752
6.25 to 6.75	0.0064	0.5645	0.5709

4.3 Extremely low cycle fatigue assessment for concrete-filled steel pier

Several cumulative damage rules have been proposed in the field of high and low cycle fatigue region. Because of its simplicity and efficiency, this study employed Miner's rule. According to the Miner's rule, cumulative fatigue damage index D can be calculated by the following equation (4-1) ~ (4-3).

$$D = \Sigma D_i \qquad (4\text{-}1)$$

$$D_i = \frac{n_i}{N_i} \qquad (4\text{-}2)$$

$$N_i = (\frac{C}{\Delta\varepsilon_{eff,i}})^{1/k} \qquad (4\text{-}3)$$

where D_i is the damage index for each strain range, $\Delta\varepsilon_{eff,i}$ and n_i are the ith effective notch strain range and its number of cycles, N_i is the fatigue life, and k is the slope of the fatigue strength curve shown in Chapter 3 and C is the constant depending on the radius of the effective notch (k=0.313, C=0.3034 in equation 3-5).

If the cumulative damage index reaches 1.0, it is assumed that low cycle fatigue damage occurred at corner weld in concrete-filled steel piers. The calculation results of the cumulative damage index are shown in **Table 4.4** and **Table 4.5**. In the table, the fatigue life for each effective notch strain calculated by equation (4-3) is also shown. **Fig. 4.8** shows the relationships between the cumulative damage index and the number of cycle. The cumulative damage indexes exceed 1.0 from 4.75 cycles to 5.25 cycles in all cases. From the proposed model, therefore, the fatigue life was estimated to be 5.25 cycles for both specimens.

Table 4.4 Calculation results of cumulative damage index (CF10)

Number of cycles	Effective notch strain range $(\Delta\varepsilon_{eff,i})$	Fatigue life (N_i)	Damage index (D_i)	Cumulative damage index (D)
0 to 0.25	0.0013	3.4E+07	0.000	0.000
0.25 to 0.75	0.0029	2.7E+06	0.000	0.000
0.75 to 1.25	0.0036	1.5E+06	0.000	0.000
1.25 to 1.75	0.0055	3.8E+05	0.000	0.000
1.75 to 2.25	0.0064	2.4E+05	0.000	0.000
2.25 to 2.75	0.0132	2.3E+04	0.000	0.000
2.75 to 3.25	0.0411	593.98	0.001	0.001
3.25 to 3.75	0.0221	4282.40	0.000	0.001
3.75 to 4.25	0.2017	3.68	0.136	0.137
4.25 to 4.75	0.1758	5.71	0.088	0.224
4.75 to 5.25	0.3843	0.47	1.064	1.288
5.25 to 5.75	0.3740	0.51	0.975	2.263
5.75 to 6.25	0.5430	0.16	3.210	5.473
6.25 to 6.75	0.5442	0.15	3.232	8.705
6.75 to 7.25	0.6673	0.08	6.202	14.907

Table 4.5 Calculation results of cumulative damage index (CF20)

| Number of cycles	Effective notch strain range $(\Delta\varepsilon_{eff,i})$	Fatigue life (N_i)	Damage index (D_i)	Cumulative damage index (D)
0 to 0.25	0.0013	3.6E+07	0.000	0.000
0.25 to 0.75	0.0029	2.8E+06	0.000	0.000
0.75 to 1.25	0.0035	1.5E+06	0.000	0.000
1.25 to 1.75	0.0049	5.2E+05	0.000	0.000
1.75 to 2.25	0.0069	1.8E+05	0.000	0.000
2.25 to 2.75	0.0125	2.6E+04	0.000	0.000
2.75 to 3.25	0.0543	244.50	0.002	0.002
3.25 to 3.75	0.0293	1736.18	0.000	0.002
3.75 to 4.25	0.2278	2.50	0.200	0.202
4.25 to 4.75	0.1982	3.90	0.128	0.331
4.75 to 5.25	0.4170	0.36	1.382	1.712
5.25 to 5.75	0.4048	0.40	1.256	2.968
5.75 to 6.25	0.5752	0.13	3.859	6.827
6.25 to 6.75	0.5709	0.13	3.766	10.593
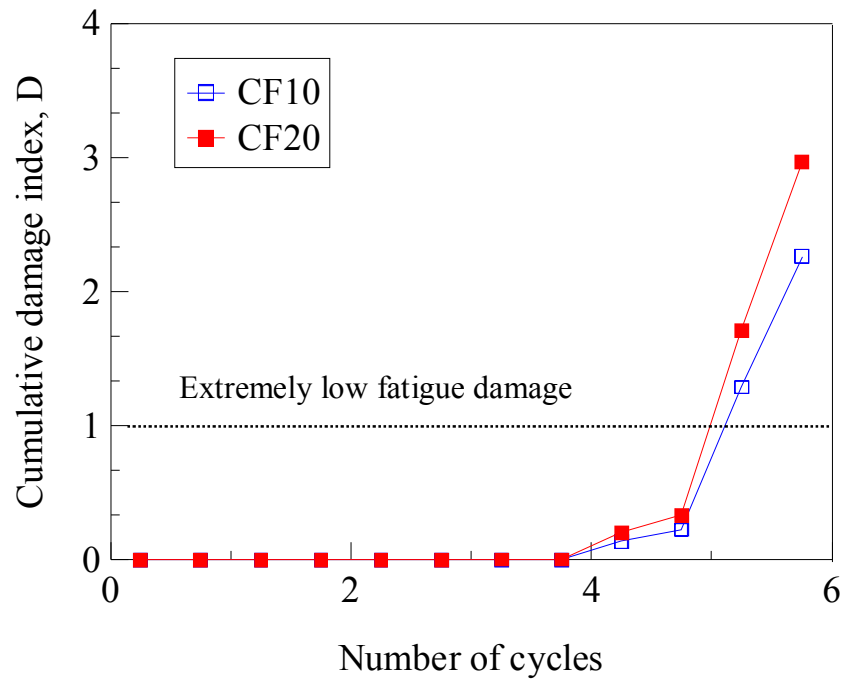
Fig. 4.8 Relationships between cumulative damage index and number of cycles
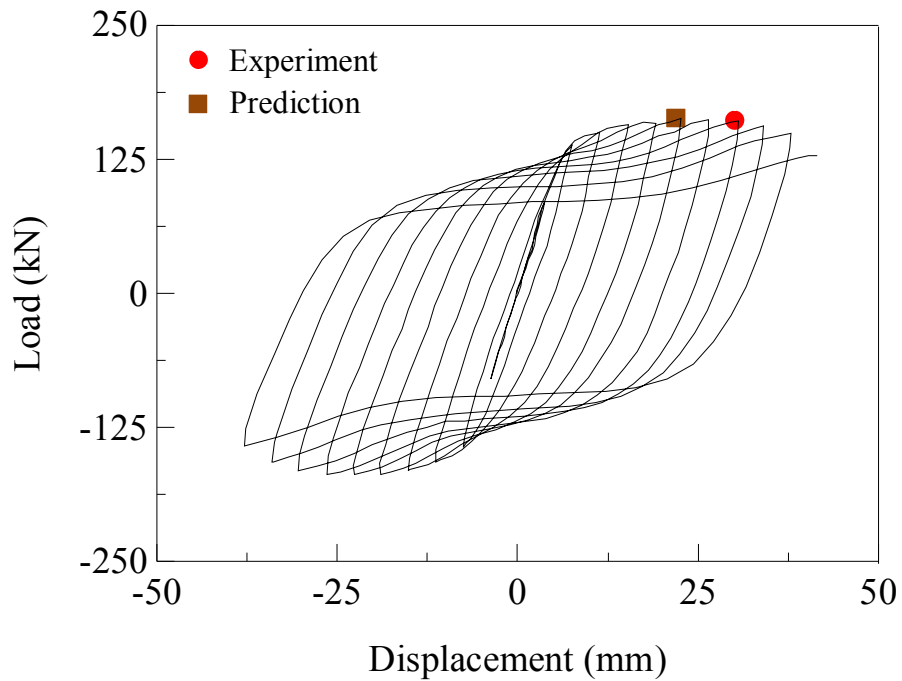
a) CF10

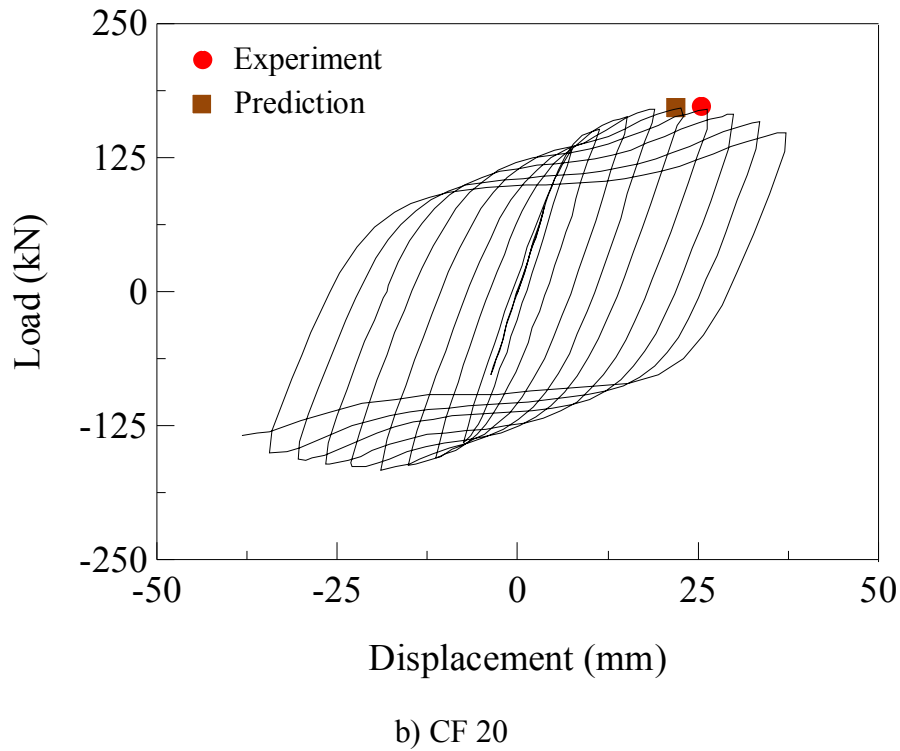**Fig. 4.9** Results of fatigue assessment for concrete-filled steel piers

b) CF 20

Fig. 4.9 Results of fatigue assessment for concrete-filled steel piers (Continued)

Fig. 4.9 shows the comparison of the fatigue life between the proposed method and the experiments. As mentioned in Chapter 3, the crack length at the fatigue life is about 1.0mm in the proposed model. On the other hand in the concrete-filled specimen, the low cycle fatigue crack in the corner weld could be detected when the crack penetrated through the weld bead. The number of cycles when the crack was observed on the specimen surface is defined as the fatigue life of the specimen, where the crack length is about 3.0mm because the sizes of weld root face and the plate thickness of the web are 1.5mm and 4.5mm, respectively.

The fatigue life was estimated to be 5.25 cycles, which are conservative results compared with the experiment. It is because the crack propagation from 1.0mm to 3.0mm was not considered in the model. Although there is small difference between the estimation and the experiment, it was confirmed that the proposed effective notch strain based method can give predictions of fatigue life of concrete-filled steel piers on the

safe side in the extremely low cycle fatigue region. In order to reduce the difference, it is needed to consider the crack propagation into the model properly.

4.4 Extremely low cycle fatigue assessment for concrete-filled steel piers by considering crack propagation

4.4.1 Estimation of crack propagation life

As stated above, the crack length at the fatigue life is different in the proposed model and the steel pier specimen. The crack length at the fatigue life is about 1mm in the proposed model. However, when the crack was first detected in concrete-filled steel pier specimen, the crack length was about 3mm. Therefore, it is needed to consider the crack propagation life from the crack length of 1mm to 3mm.

Here, the crack propagation life from the crack length of 1mm to 3mm was calculated using the crack length measured at the side surface in the corner welded joint. In this study, the results of C4 series corner welded joints specimen was used because the ratio of crack length to specimen thickness is similar with that of concrete-filled specimen.

Fig. 4.10 shows examples of the crack length measured at the side surface in the corner welded joint (C4-12, C4-15 and C4-18). In the double-logarithmic graph, a linear relationship can be achieved between the number of cycles and the crack length on the surface. From this relation, the crack length can be expressed as the following equation.

$$a = \alpha \cdot N^{\beta} \qquad (4\text{-}4)$$

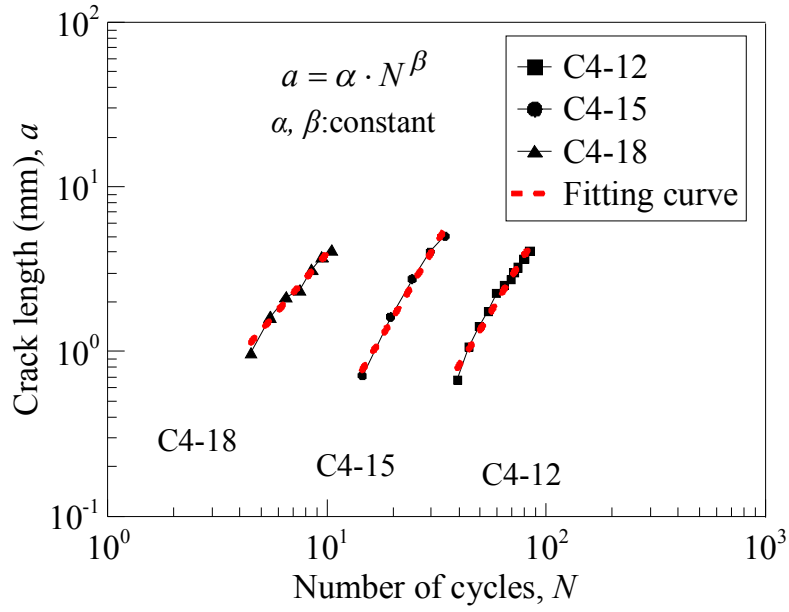where a is crack length, N is the number of cycles, and α and β is constant.

Fig. 4.10 Calculation method of crack propagation life by fitting curve

In this study, it is assumed that the slope "β" in the fitting curve, is constant in both inside and outside surface of the specimen. And the crack length at the 20% load drop is set to be 1.0mm. By assigning the crack length of 1.0mm and the number of cycles when the load was dropped by 20% to equation (4-4), α can be obtained. Then, the number of cycles when the crack propagates to 3.0mm can be estimated by equation (4-4).

After then, the crack growth rate (da/dN) is calculated by dividing crack propagation length (2.0mm) with the number of cycles when crack length is from 1.0mm to 3.0mm

Fig 4.11 shows crack growth relationship between effective notch strain range and crack growth rate (da/dN) in inside of the specimen. A linear relationship can be achieved between the effective notch strain range and the crack growth rate. Therefore, this chapter assumes that the following equation can be used as the fatigue crack growth curve for the concrete-filled steel pier specimen.

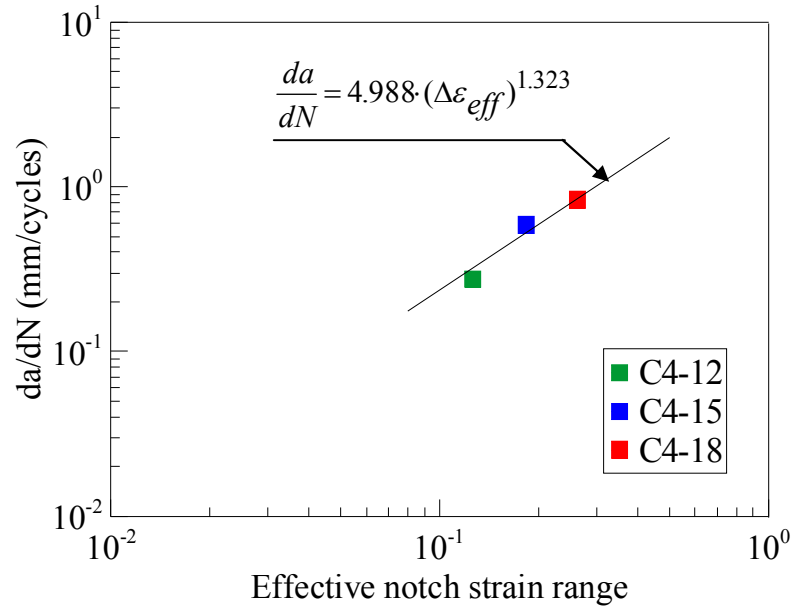$$\frac{da}{dN} = 4.988 \cdot (\Delta\varepsilon_{eff})^{1.323} \tag{4-5}$$

$$\frac{da}{dN} = 4.988 \cdot (\Delta\varepsilon_{eff})^{1.323}$$

Fig. 4.11 Crack growth curve

4.4.2 Re-assessments of concrete-filled steel piers

The prediction fatigue life of concrete-filled steel piers were calculated as the summation of fatigue life in the proposed model and crack propagation life estimated as mentioned above. If the cumulative damage index becomes 1.0, it is assumed that the crack length is 1.0mm. And then, the crack propagation life calculated based on equation (4-5), in which the crack length of 1.0mm to 3.0mm.

Fig. 4.12 shows the comparison of the fatigue life between the proposed effective notch strain approach method and the experiments. By considering the crack propagation life, the prediction life in CF10 specimen was estimated to be 6.25 cycles, whereas it was 7.25 cycles in the experiment. In CF 20 specimen, the prediction life gets to agree with the test result. It was revealed that the fatigue life of concrete-filled steel piers can be predicted more accurately when considering crack propagation into the assessment. However, this study estimated crack propagation life under the assumption that crack growth curve in extremely low cycle fatigue region can be

expressed as equation (4-5). On this point, further investigation is strongly needed in future research.
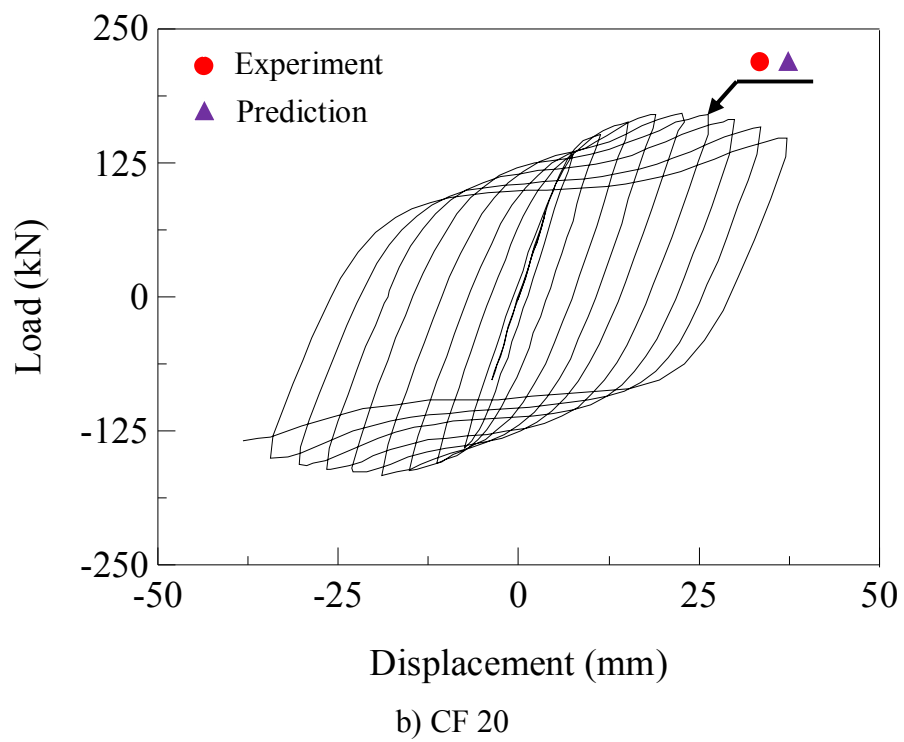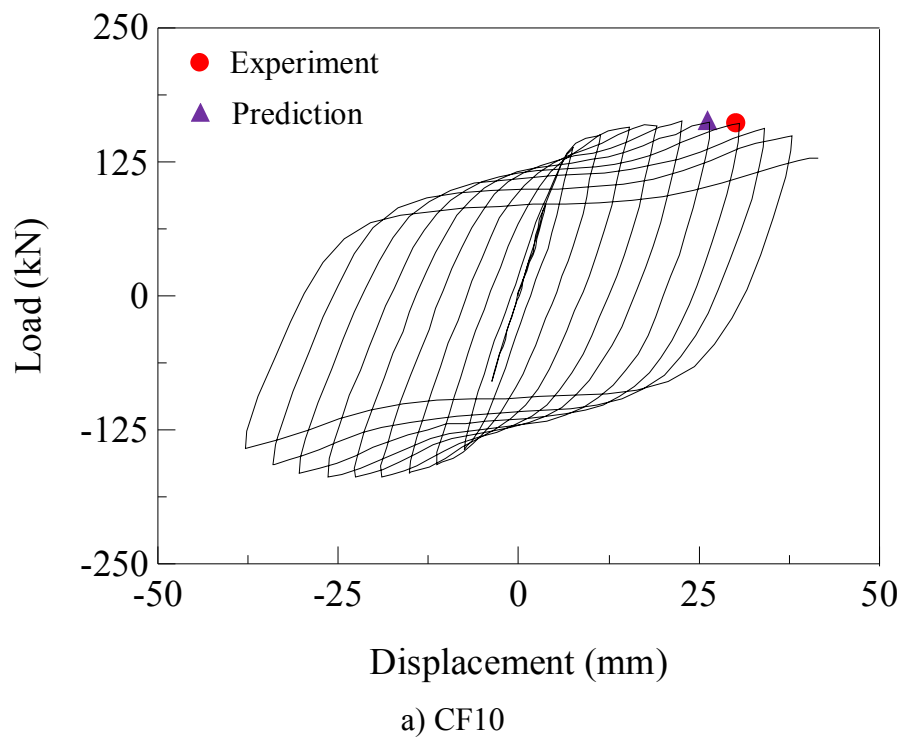

a) CF10

b) CF 20

Fig. 4.12 Results of re-assessment of concrete-filled steel piers

4.5 Concluding remarks

In this chapter, the applicability of the proposed method to concrete-filled steel piers was investigated. Effective notch strain range around cracking sites in the steel piers specimens was calculated by finite element analyses with the sub-modeling technique. Based on the results, the fatigue lives of concrete-filled steel piers specimen were estimated.

The main conclusions can be drawn as follows:

1) The out-of-bending deformations of the flange and web caused the rapid increases of the effective notch strain, leading to the low cycle fatigue failure.

2) The fatigue lives of the concrete-filled steel pier specimen were conservatively estimated when compared with the experiment results. The proposed effective notch strain based method can predict the fatigue life of concrete-filled steel piers on the safe side in the extremely low cycle fatigue region.

3) By considering the fatigue crack propagation life into the proposed method, the fatigue lives of the specimens can be predicted more accurately.

CHAPTER 5

SUMMARIES AND CONCLUSIONS

As a countermeasure of local buckling, filling steel piers with concrete methods are often used. The concrete-filled steel piers have high strength, ductility, and load carrying capacity due to confinement of in-filled concrete. However, when large plastic deformation repeatedly occurs in the piers, low cycle fatigue can be a serious problem. In the existing steel piers retrofitted against local buckling by filling with concrete, the corner crack from corner welded joints has possibility to cause extremely low cycle fatigue failures. Therefore, this dissertation research aims to develop the extremely low cycle fatigue assessment method of corner crack in concrete-filled steel piers. The following is a summary of the research findings.

5.1 Conclusion

In *Chapter 2*, the extremely low cycle behavior of concrete-filled steel piers was experimentally and analytically investigated. Concrete-filled steel pier specimens with box section were fabricated by welding. The longitudinal welds between flange and web plates, which is called "corner weld" in this study, were connected with partial joint penetration groove welds. According to axial load level and the filling concrete state, the low cycle fatigue tests were performed. Incremental loading was applied under displacement control in the tests. And elasto-plastic finite element analyses were conducted to investigate deformation behaviors around the cracking sites in the specimen. Based on the experiment and analysis results, the following conclusions were obtained.

1) In the concrete-filled steel pier specimen, low cycle fatigue crack occurred first from triangular ribs. Then, local buckling was observed on the flange and web plates. Finally, the corner weld around the locally-buckled area was split

85

vertically by cyclic plastic deformation. The buckling deformation was relatively small compared with that of no in-filled concrete steel pier and the load carrying capacity was hardly reduced due to the local buckling.

2) The load carrying capacity of concrete-filled steel pier specimen decreased due to the crack initiation and propagation from the corner weld. This crack is one of the main failure modes of the concrete-filled steel piers.

3) The strain behaviors around cracking site were revealed by elasto-plastic finite element analysis. The analysis result indicated that the crack from corner weld in the specimen initiated at the weld root tip by its opening and closing behavior due to cyclic out-of-plane bending deformation of the flange and web plates.

In *Chapter 3*, the extremely low cycle fatigue strength of the corner joints with single bevel welding was investigated. Low cycle fatigue tests were performed with corner welded joints specimens with different size of weld root faces. The tests were performed under large cyclic bending deformations. The low cycle fatigue life of the corner welded joints was defined as the number of cycles to 20% drop, because the maximum load tended to decrease rapidly. The crack length at the fatigue life is about 1.0mm. In the FE analysis, effective notch concept is introduced at a weld root tip to avoid the effect of strain singularity. Two types of effective notch with a radius (R) of 0.3mm and 1.0mm were adopted at the tip so that different radius could be used depending on plate thickness. The fatigue assessments of corner welded joints in the extremely low cycle fatigue regions were performed based on the effective notch strain approach. Based on the experiment and analysis results, the following conclusions were reached.

1) Low cycle fatigue strength of corner welded joints strongly depended on the size of the weld root faces.

2) Local strain at the root tip was calculated by applying the effective notch concept, where it is called the effective notch strain.

3) When arranging the test results with the effective notch strain range, a unique fatigue strength curve could be observed regardless of the weld root size and the joint configuration.

4) Based on the results, this study proposed the fatigue strength curve for the corner welded joint based on the effective notch strain.

In *Chapter 4*, the applicability of the proposed method to concrete-filled steel piers was investigated. In order to calculate the effective notch strain around cracking sites in the steel piers specimens, sub-model technique was applied in finite element analyses. The validity of sub-model was proved by the results of global model. By comparing the effective notch strain with the proposed fatigue strength curve, cumulative damage indexes were calculated. The predicted fatigue lives by the method were estimated compared with experiment results. Furthermore, new fatigue strength curve was suggested by considering crack propagation and based on the new curve, the predicted fatigue lives were estimated again. The conclusions could be drawn as follows:

1) The out-of-bending deformations of the flange and web plates caused the rapid increases of the effective notch strain, leading to the low cycle fatigue failure.

2) The fatigue lives of the concrete-filled steel pier specimen were conservatively estimated when compared with the experiment results. The proposed method could predict the fatigue life of concrete-filled steel piers on the safe side in the extremely low cycle fatigue region.

3) By considering the fatigue crack propagation life into the proposed method, the fatigue lives of the specimens could be predicted more accurately.

5.2 Recommendation for future research

The following recommendations for further study are suggested as follows:

1) The fatigue assessment method based on the effective notch approach needs finite element model with very fine mesh. So, in order to establish design method for concrete-filled steel piers, it is needed to develop a simpler method using such as nominal strain.

2) In Chapter 4, in order to match the definition of the fatigue life between the concrete-filled specimen and the corner joint, the crack propagation behavior was simply assumed. It is needed to establish more rational assessment method for the crack propagation in the extremely low cycle fatigue region.

REFERENCES

American Concrete Institute: *ACI Code issues-coefficient of friction: Concrete to concrete*, 2001.

Chen, T., and Tateishi, K.: Extremely Low Cycle Fatigue Assessment of Thick Walled Steel Pier Using Local Strain Approach, *Journal of Structural Engineering, JSCE*, 53A, pp.485-492, 2007.

Coffin, L. F.: A Study of the Effects of Cyclic Thermal Stresses on a Ductile Metal, *Trans. ASME* , 76, pp.931-950, 1954.

Dražan, K.., Nenad, G., and Pejo K.: Fracture Mechanics Approach to Heterogeneous Welded Structures, *International Conference Research and Development in Mechanical Industry*, 1, pp.237-240, 2002.

Fricke, W.: Guideline for the Fatigue Assessment by Notch Stress Analysis for Welded Structures, *IIW Documentation*, XIII-2240-08/XV-1289-08, 2008.

Ge, H., Usami, T., and Toya, K.: A Study on Strength and Deformation Capacity of Concrete-filled Steel Columns under Cyclic Loading, *Journal of Structural Engineering, JSCE*, 40A, pp.163-176, 1994 (in Japanese).

Goto, Y., Ghosh, P. K., and Kawanishi, N.: FEM Analysis for Hysteretic Behavior of CFT Bridge Piers Considering Interaction Between Steel Tube and In-filled Concrete, *Doboku Gakkai Ronbunshuu A, JSCE*, 65 (2), pp.487–504, 2009 (in Japanese).

Goto, Y., Ghosh, P. K., and Kawanishi, N.: Nonlinear Finite Element Analysis for Hysteretic Behavior of Thin-walled Circular Columns with In-filled Concrete, *Journal of Structural Engineering, ASCE*, 136 (11), pp.1413-1422, 2010.

Goto, Y., Kosuke, M., and Ghosh, P. K.: Nonlinear Finite Element Analysis for Cyclic Behavior of Thin-walled Stiffened Rectangular Steel Columns with In-filled concrete, *Journal of Structural Engineering, ASCE* , 138 (5), pp.571-584, 2012.

Gunaraj, V., and Murugan, N.: Prediction of Heat-affected Zone Characteristics in Submerged Arc Welding of Structural Steel Pipes, *Welding Research Supplement*, pp. 94-98, 2002.

Hobbacher, A.: Recommendations for Fatigue Design of Welded Joints and Components, *IIW Documentation*, XIII-1539-96/XV-845-96, 2008.

Hajjar, J. F., Molodan, A., and Schiller, P. H.: A Distributed Plasticity Model for Cyclic Analysis of Concrete-filled Steel Tube Beam Columns and Composite Frames, *Engineering structures*, 20 (4-6), pp.398–412. 1998

Hanji, T., Siprasertkit, K., and Miki, C.: Low- and High-cycle Fatigue Behavior of Load-carrying Cruciform Joints with Incomplete Penetration and Strength Under-match, *International Journal of Steel Structure* , 11 (4), pp.409-425, 2011.

Hanji, T., Tateishi, K., Minami, K., and Kitoh, K.: Extremely Low Cycle Fatigue Assessment for Welded Joints based on Peak Strain Approach, *Journal of Structural Mechanics and Earthquake Engineering, JSCE*, 808 (I-74), pp.137-145, 2006 (in Japanese).

Iida, K.: Various Fundamental Problems on Low Cycle Fatigue, *Journal of the Japan welding society*, 37 (6), pp.542-559, 1968.

Iida, K.: Notch Effects in Low Cycle Fatigue of Steels, *Selected papers from the journal of the Society of Naval Architects of Japan*, 11, pp.117-134, 1973.

Iida, K., and Fujii, E.: Low cycle fatigue strength of steels and welds in relation to static tensile properties. *4th International Conference on Fracture*, 2, pp. 19-24, 1977.

Iura, M., Orino, A., and Isizawa, T.: Elasto-plastic Behavior of Concrete-filled Steel Tubular Columns, *Journal of Structural Mechanics and Earthquake Engineering, JSCE* , 696 (I-58), pp.285-298, 2002 (in Japanese).

Japan Road Association: *Specification for high way bridge*, 2012 (in Japanese).

Japan Society of Civil Engineers: *Investigation report on the Tohoku Earthquake,* 2011(in Japanese).

Johansson, M., and Gylltoft, K.: Structural Behavior of Slender Circular Steel-concrete Composite Columns under Various Means of Load Application, *Steel Composite Structures*, Vol. 1(4), pp.393–410, 2001.

Kaneta, K., and Kohzu, I.: Low Cycle Fatigue Strength of Welded Steel Structural Joint, *Transactions of the Architectural Institute of Japan* , pp.313, 30-38, 1983.

Komotori, J., and Shimizu, M.: Mircostructural Effect Controlling Exhaustion of Ductility in Extremely Low Cycle Fatigue, *Journal of the Japan Society of Mechanical Engineers,* 57 (544), pp.2879-2883, 1991.

Lee, J., and Fenves, G.: Plastic-Damage Model for Cyclic Loading of Concrete Structures. *Journal of Engineering Mechanics*, 124(8), pp.892–900, 1998.

Liu, W. C., Liang, Z., and Lee, G. C.: Low-cycle Bending-Fatigue Strength of Steel Bars under Random Excitation, Part I: Behavior, *Journal of Structural Engineering, ASCE*, 131(6), pp.913-918, 2005.

Liu, W. C., Liang, Z., and Lee, G. C.: Low-cycle Bending-Fatigue Strength of Steel Bars under Random Excitation. Part II: Design Considerations. *Journal of Structural Engineering, ASCE*, 131(6), pp.919-923, 2005.

Machida, S., Matoba, M., Yoshinari, H., and Nishimura, R.: Definition of Hot Spot Stress in Welded Structure for Fatigue Assessment (2nd report), *Journal of the Society of Naval Architects of Japan*, 170, pp.705-721, 1991.

Mander, J. B., Panthaki, F. D., and Kasalanati, A.: Low-Cycle Fatigue Behavior of Reinforcing Steel. *Journal of Materials in Civil Engineering, ASCE* , 6 (4), pp.453-468, 1994.

Manson, S. S.: Behavior of Materials under Conditions of Thermal Stress. *NASA technical note*, 2933, 1953.

Masatoshi, k.: Extremely Low Cycle Fatigue Life Prediction based on a New Cumulative Fatigue Damage Model. *International Journal of Fatigue*, 24, pp.699-703, 2001.

Matsumura, T., and Mizuno, E.: 3-D FEM Analyses on Internal State inside the Concrete Filled Steel Tubular Columns subjected to Flexural Deformation under Axial Loading, *Journal of Structural Engineering, JSCE,* 53A, pp.75–83, 2007 (in Japanese).

Michael, J., Verrilli, J., Rodney, E., and Robert W. Swindeman: Current Activities in Standardization of High-Temperature, Low-Cycle-Fatigue Testing Techniques in the United States*, NASA Technical Memorandum 103675*, 1990.

Miki, C.: Damage to Civil Structures in Great Hanshin Earthquake, *Welding in the world*, 38, pp.243-255, 1996.

Miki, C., Nishimura, R., Tanabe, H., and Nishikawa, K.: Study on Estimation of Fatigue Strengths of Notched Steel Members, *Proc. JSCE*, 316, pp. 153-168, 1981.

Nakahara, H., Ninakawa, T., and Sakino, K.: Cyclic Bending Behavior of Concrete Filled Steel Tubular Columns under Constant Gravity Load, *Journal of Structural and Construction Engineering*, AIJ, 568, pp.139-146, 2003.

Nakagomi, T., and Lee, K.: Experimental study on fatigue characteristic of SM490 by repeated load, *Journal of Structural and Construction Engineering,* AIJ, 469, pp. 127-136, 1995 (in Japanese).

Nakajima, N., and Yamada, M.: Research on the Extremely Low Cycle Fatigue Fracture Limit of Structural Steel from the View Point of Damage Energy, *Journal of Structural Construction Engineering*, AIJ, 534, pp.9-16, 2000 (in Japanese).

Nihei, M., Konno, T., and Iida, K.: Prediction of fatigue strength under bending by use of hysteresis energy concept, *Journal of the Society of Naval Architects of Japan*, 184, pp. 458-468, 1984.

Nishimura, T., and Miki, C.: Strain Controlled Low Cycle Fatigue Behavior of Structural Steels, *Proc. JSCE*, 279, pp. 29-44, 1978 (in Japanese).

Park, Y. S., Park, S. J., Iwai, S., and Kang, S. H.: Failure and Damage of Steel Thin-Plate Elements and Angle Members Due to Very-Low-Cycle Loading, *Engineering Structures* , 26, pp.1623-1632, 2004.

Radaj, D., Sonsino, C. M. and Fricke, W.: Fatigue Assessment of Welded Joints by Local Approach, *Woodhead: Woodhead Publishing*, 2006.

Saiprasertkit, K., Hanji, T. and Miki, C.: Fatigue Strength Assessment of Load-carrying Cruciform Joints with Material Mismatching in Low- and High-cycle Fatigue Regions on the Effective Notch Concept, *International Journal of Fatigue*, 40, pp.120-128, 2012.

Sakano, M. and Wahab, M. A.: Extremely Low Cycle (ELC) Fatigue Cracking Behaviour in Steel Bridge Rigid Frame Piers, *Journal of Materials Processing Technology*, 118, pp.36-39, 2001.

Sakino, K., and Tomii, M.: Hysteretic Behavior of Concrete Filled Square Steel Tubular Beam-Column Failed in Flexure, *Transactions of the Japan Concrete Institute*, 3, pp.439-446, 1981.

Shimada, K., Komotori, J., and Shimizu, M.: The Applicability of the Manson-Coffin law and Miner's law to Extremely Low Cycle Fatigue, *Journal of the Japan Society of Mechanical Engineers*, 53 (491), pp.1178-1185, 1987.

Susantha, K. A., Ge, H., and Usami, T.: Cyclic Analysis and Capacity Prediction of Concrete-filled Steel Box Columns, *Earthquake Engineering and Structural dynamics,* 31 (2), 195–216, 2002.

Tateishi, K., and Hanji, T.: Low cycle fatigue strength of butt-welded steel joint by means of new testing system with image technique, *International Journal of Fatigue*, 26, pp. 1349-1356, 2004.

Tateishi, K., Hanji, T., and Minami, K.: A Prediction Model for Extremely Low Cycle Fatigue Strength of Welded Materials, *Journal of Structural Engineering, JSCE*, 51A, pp.1275-1282, 2005 (in Japanese).

Tateishi, K., Hanji, T., and Minami, K.: A Prediction Model for Extremely Low Cycle Fatigue Strength of Structural Steel, *International Journal of Fatigue*, 29, pp.887-896, 2007.

Urm, H. S., Yoo, I. S., Heo, J. H., Kim, S. C., and Lotsberg, I.: Low Cycle Fatigue Strength Assessment for Ship Structures, *9th Symposium on Practical Design of Ships and Other Floating Structures,* 2, pp.12-17, 2004.

Usami, T., and Kumar, S.: Damage Evaluation in Steel Box Columns by Pseudodynamic Tests, *Journal of structural engineering*, 122 (6), pp.635-642, 1996.

Usami, T.: Guidelines for Stability Design of Steel Structures (2nd Edition ed.), *Japan Society of Civil Engineers*, 2005 (in Japanese).

Usami, T.: Guidelines for Seismic and Damage Control Design of Steel Bridges, *Japan Society of Steel Construction*, 2006 (in Japanese).

Varma, H. A., Ricles, J. M., Sause, R., and Lu, L. W.: Seismic Behavior and Modeling of High-strength Composite Concrete-filled Steel Tube (CFT) Beam-columns, *Journal of Constructional Steel Research*, 58 (5-8), pp.725–758, 2002.

Wong, Y. K., Hu, X. Z., and Norton, M. P.: Low and High Cycle Fatigue Interaction in 316L Stainless Steel, *Journal of Testing and Evaluation*, 29 (2), pp.138-145, 2001.

Xiao, Y., He, W. H., and Mao, X. Y.: Development of Confined Concrete Filled Tubular (CCFT) Columns, *Journal of Building Structures*, 25 (6), pp.59-66, 2004.

Zhang, G. W., Xiao, Y., and Kunnath, S.: Low-Cycle Fatigue Damage of Circular Concrete-Filled-Tube Columns, *ACI Structural Journal*, 106 (2), pp.151-159, 2009.

Zhong, Y., Shan, Y., Xiao, F., and Yang, K.: Effect of Toughness on Low Cycle Fatigue Behavior of Pipeline Steels, *Materials Letters*, 59, pp.1780-1784, 2005.

APPENDIX A: Load-displacement hysteresis loops

Following figures are load-displacement hysteresis loops on the small-scale specimens corresponding to **Fig. 3.5** in Chapter 3.
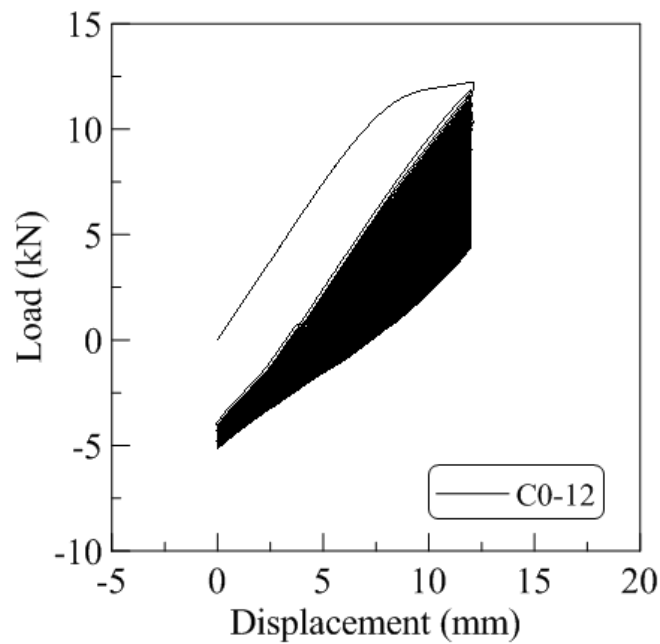
a) C0-12
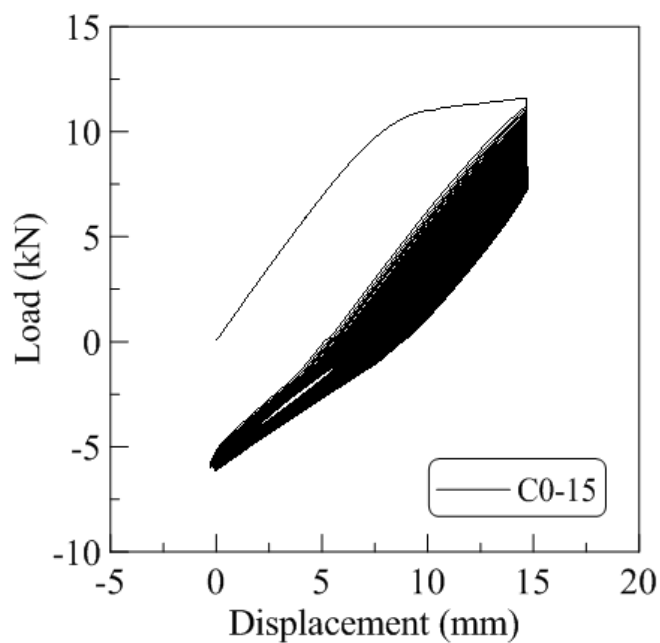
b) C0-15
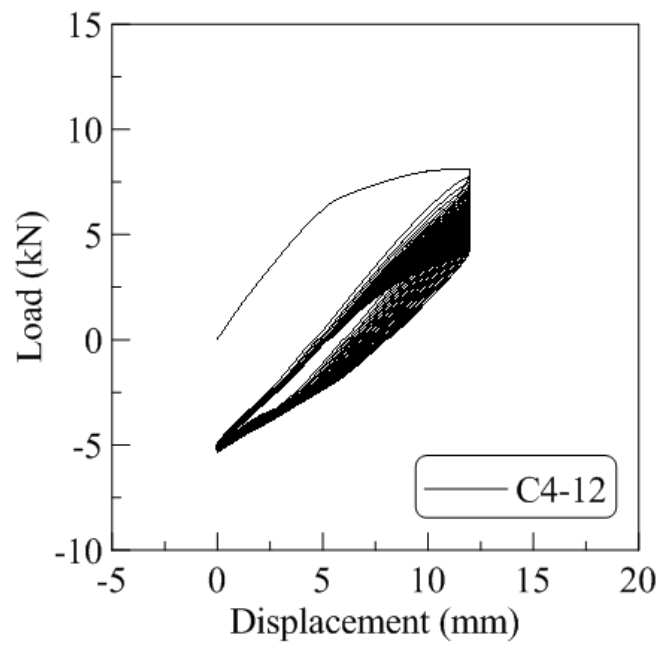
c) C4-12
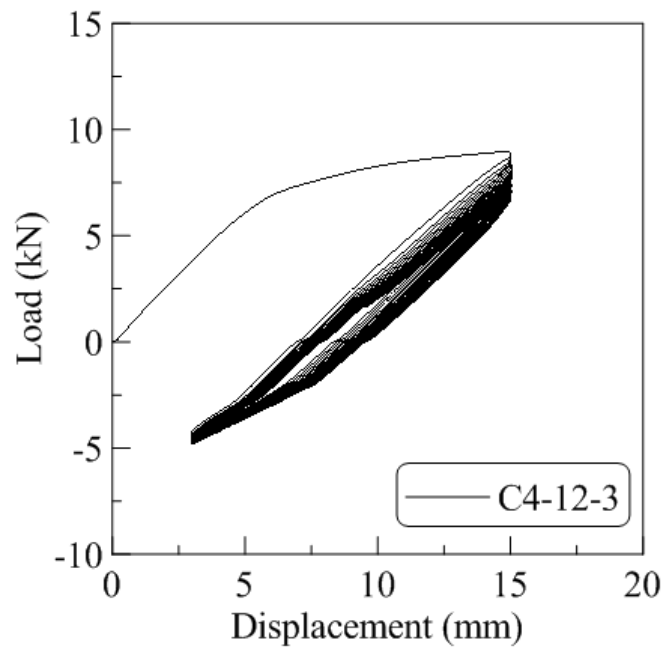
d) C4-12-3
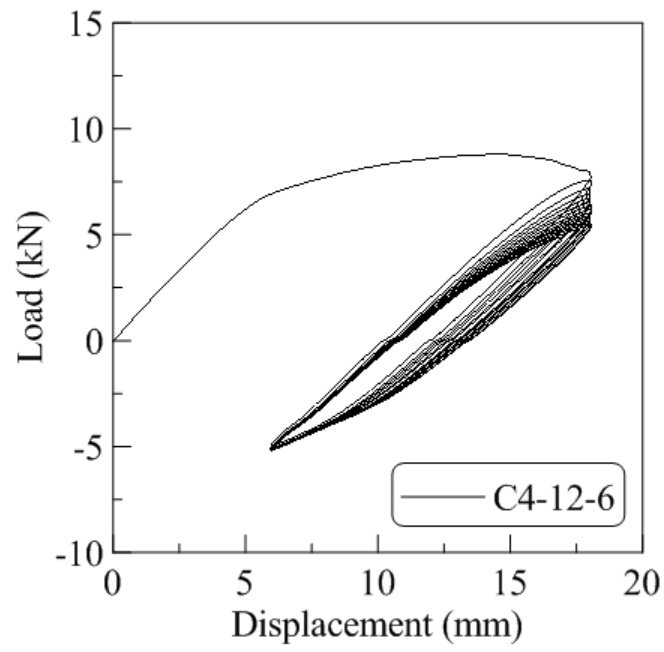
e) C4-12-6
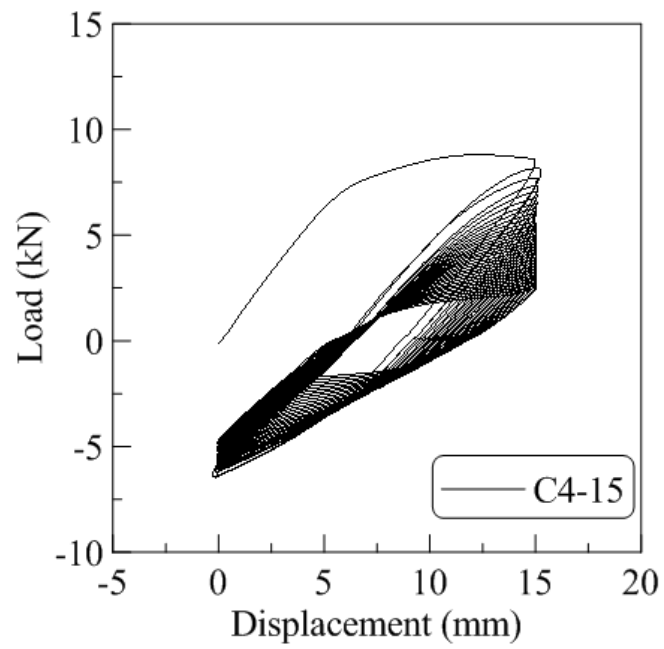
f) C4-15
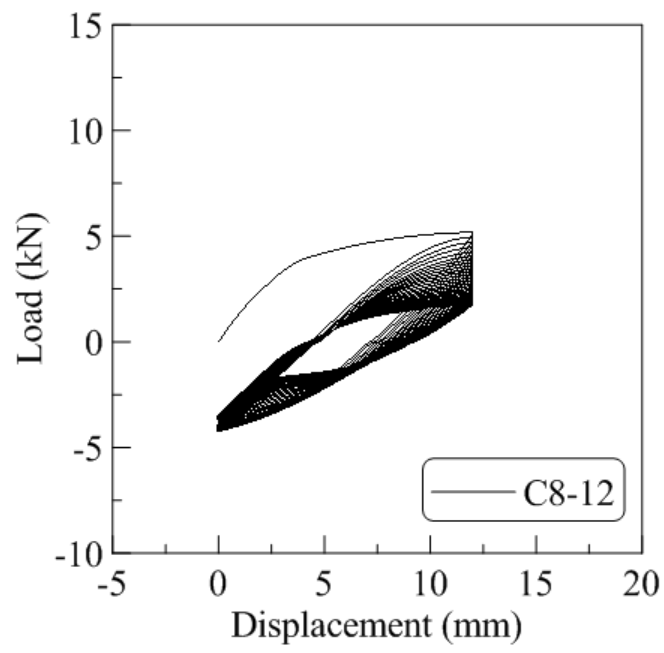
g) C8-12
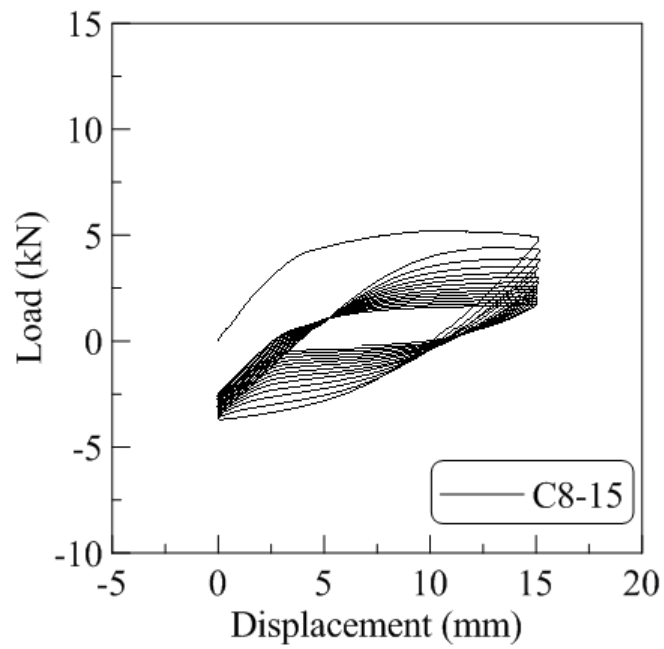
h) C8-15

Fig. A Load-displacement hysteresis loops

APPENDIX B: Crack propagation behaviors

Following figures are crack propagation behaviors at the side surface on the small-scale specimens corresponding to **Fig. 3.7** in Chapter 3.
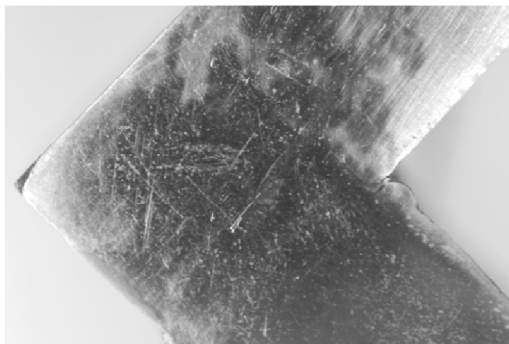
a) 450 cycles (0.87mm)
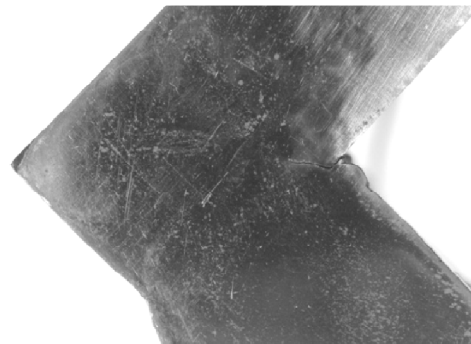
b) 900 cycles (3.24mm)
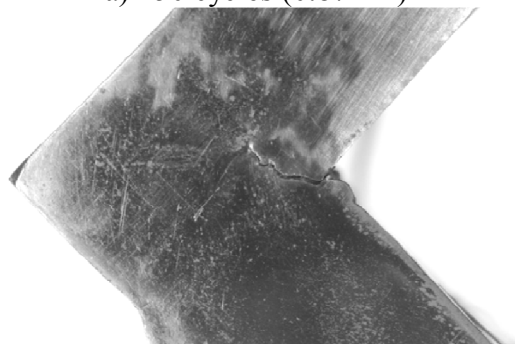
c) 1200 cycles (6.42mm)
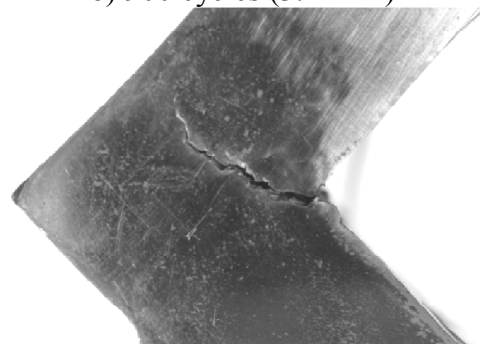
d) 1450 cycles (13.34mm)

a) C0-15
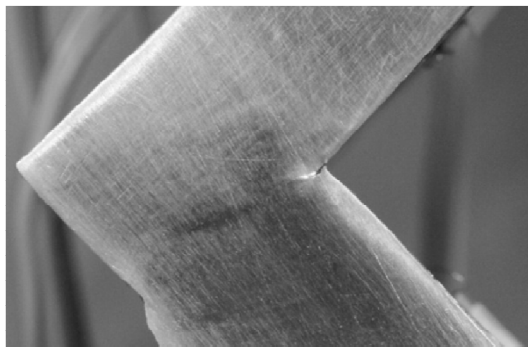
a) 80 cycles (0.84mm)
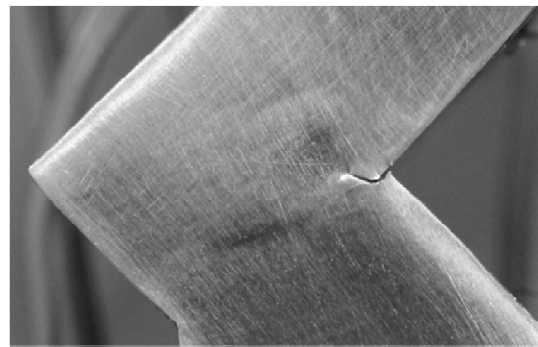
b) 150 cycles (2.29mm)
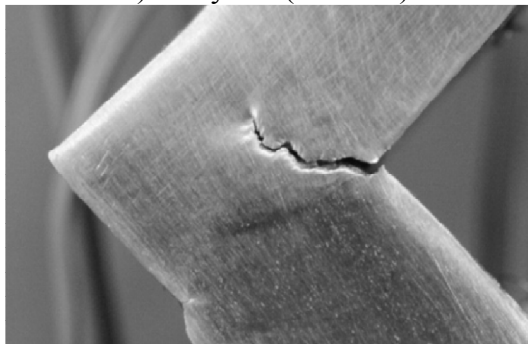
c) 270 cycles (10.74mm)
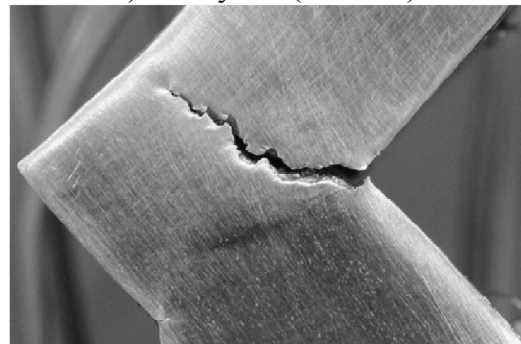
d) 340 cycles (15.6mm)

b) C0-18
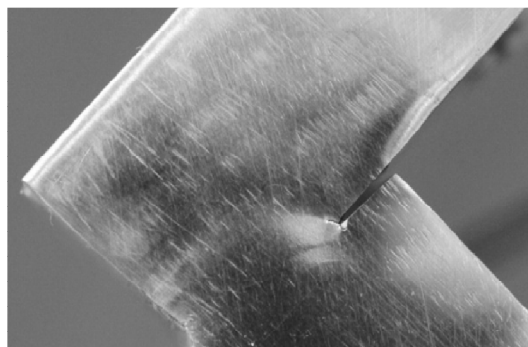
a) 90 cycles (0.72mm)
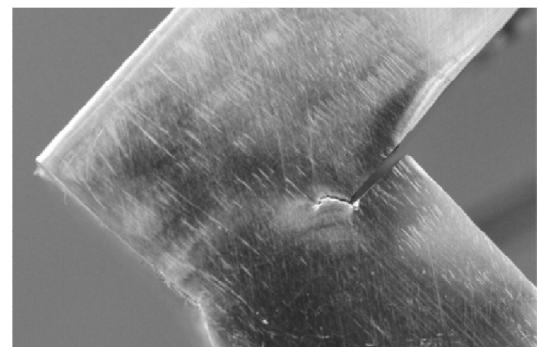
b) 130 cycles (2.30mm)
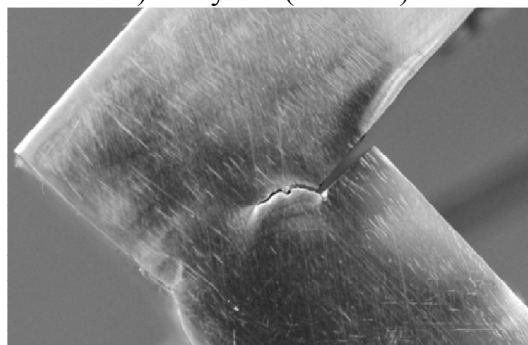
c) 160 cycles (4.70mm)
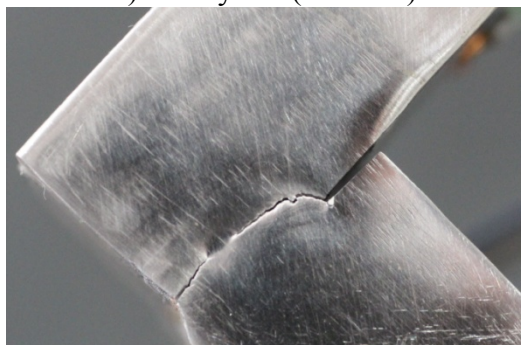
d) 220 cycles (6.87mm)

c) C4-12-3
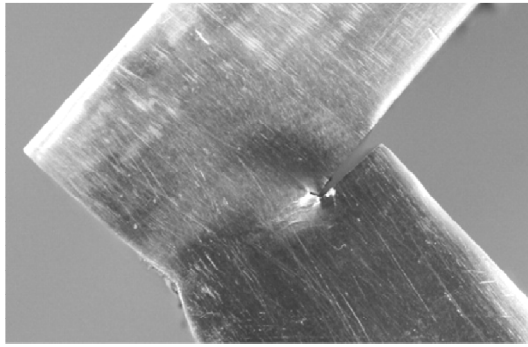
a) 30 cycles (0.67mm)
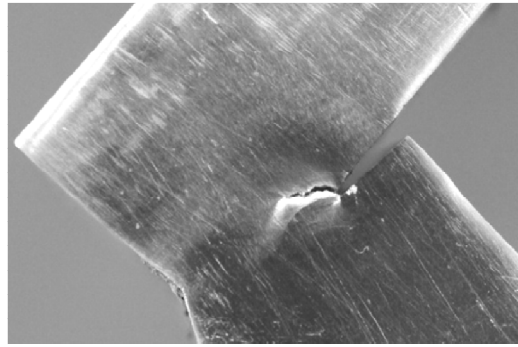
b) 55 cycles (3.40mm)
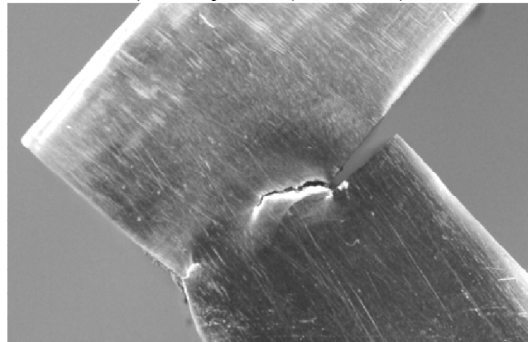
c) 75 cycles (5.22mm)
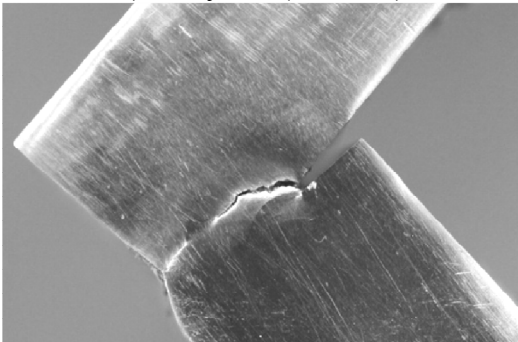
d) 100 cycles (6.97mm)

d) C4-12-6
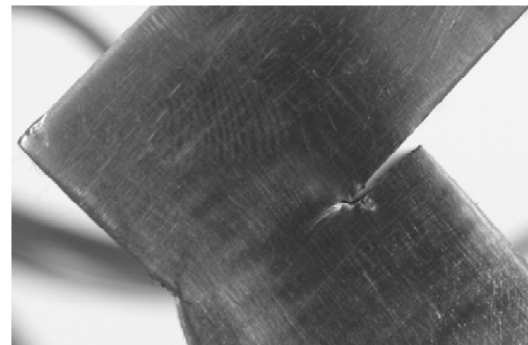
a) 15 cycles (0.71mm)

b) 30 cycles (4.01mm)
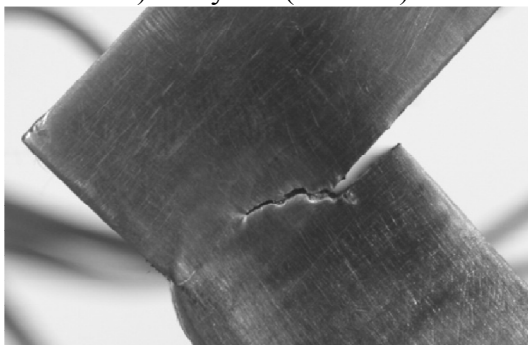
c) 45 cycles (6.35mm)
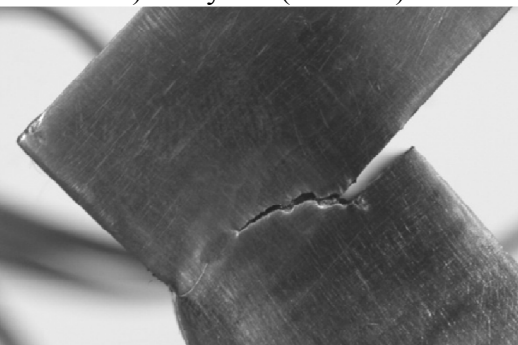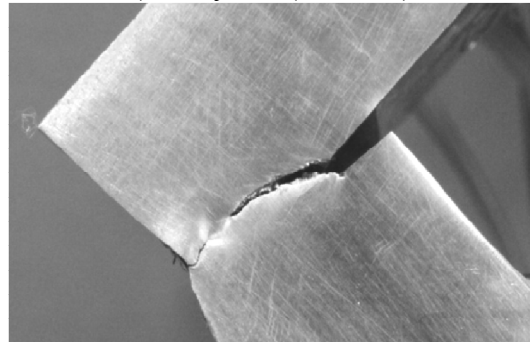
d) 60 cycles (7.45mm)
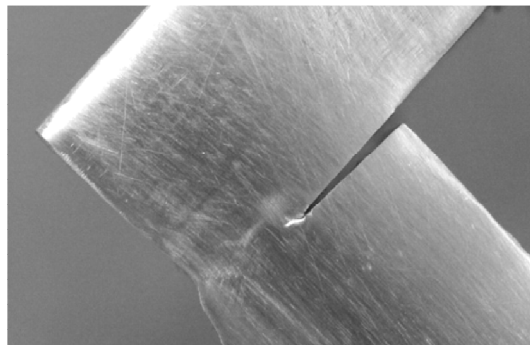
e) C4-15
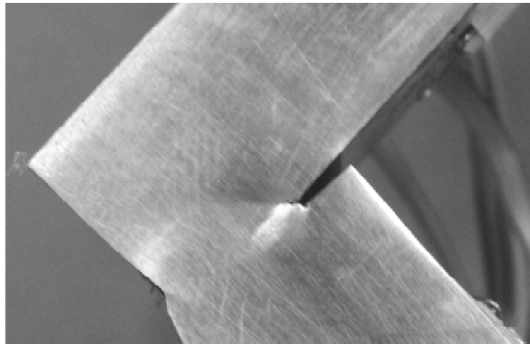
a) 5 cycles (0.98mm)
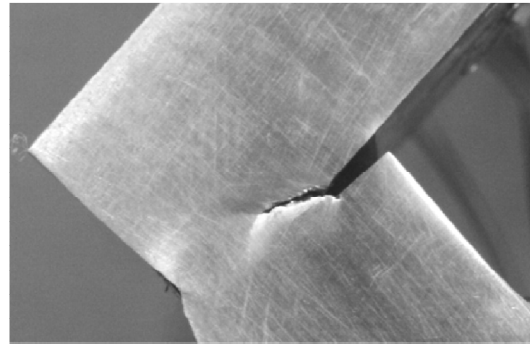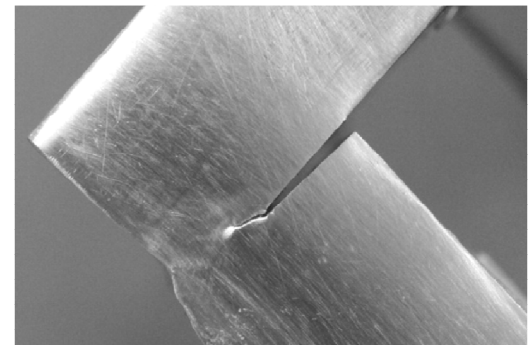
b) 12 cycles (4.50mm)
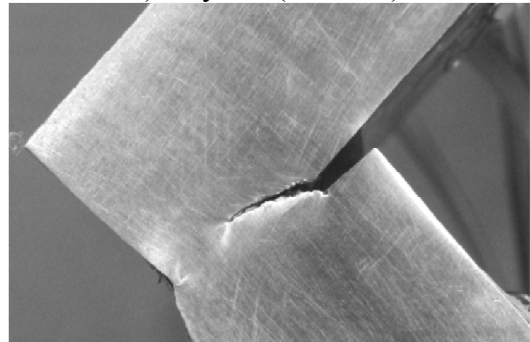
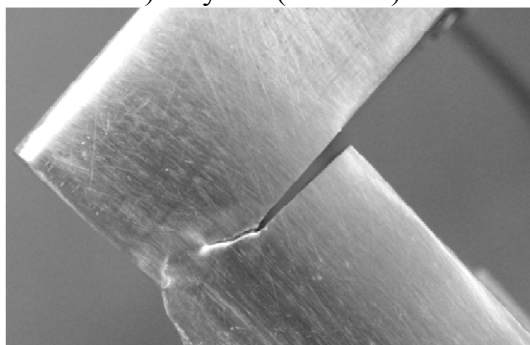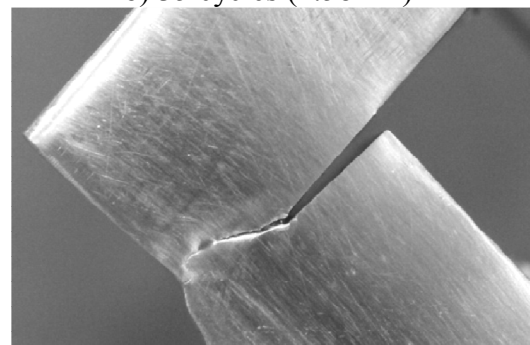c) 20 cycles (6.13mm)

d) 30 cycles (7.38mm)

f) C4-18

a) 9 cycles (0.75mm)

b) 35 cycles (2.58mm)

c) 65 cycles (3.79mm)

d) 100 cycles (4.95mm)

g) C8-12

a) 8 cycles (0.87mm)

b) 15 cycles (2.91mm)

c) 25 cycles (4.31mm)

d) 50 cycles (5.63mm)

h) C8-15

a) 5 cycles (0.86mm)

b) 10 cycles (3.13mm)

c) 18 cycles (4.73mm)

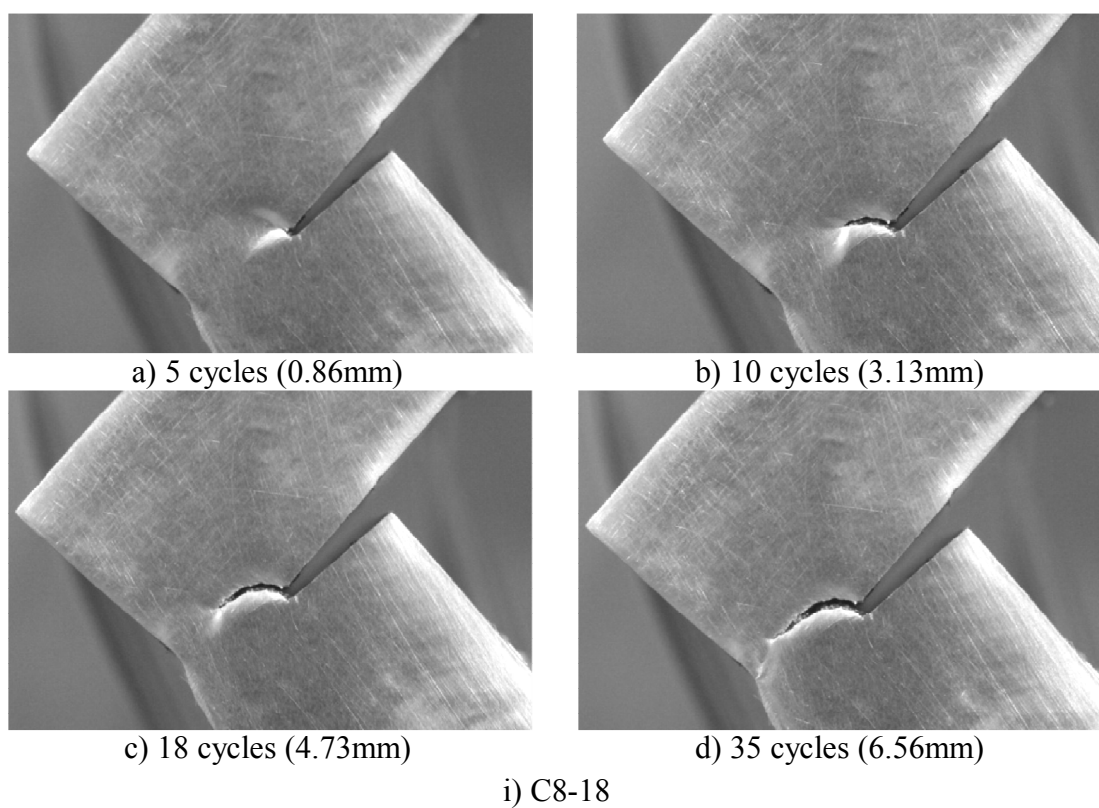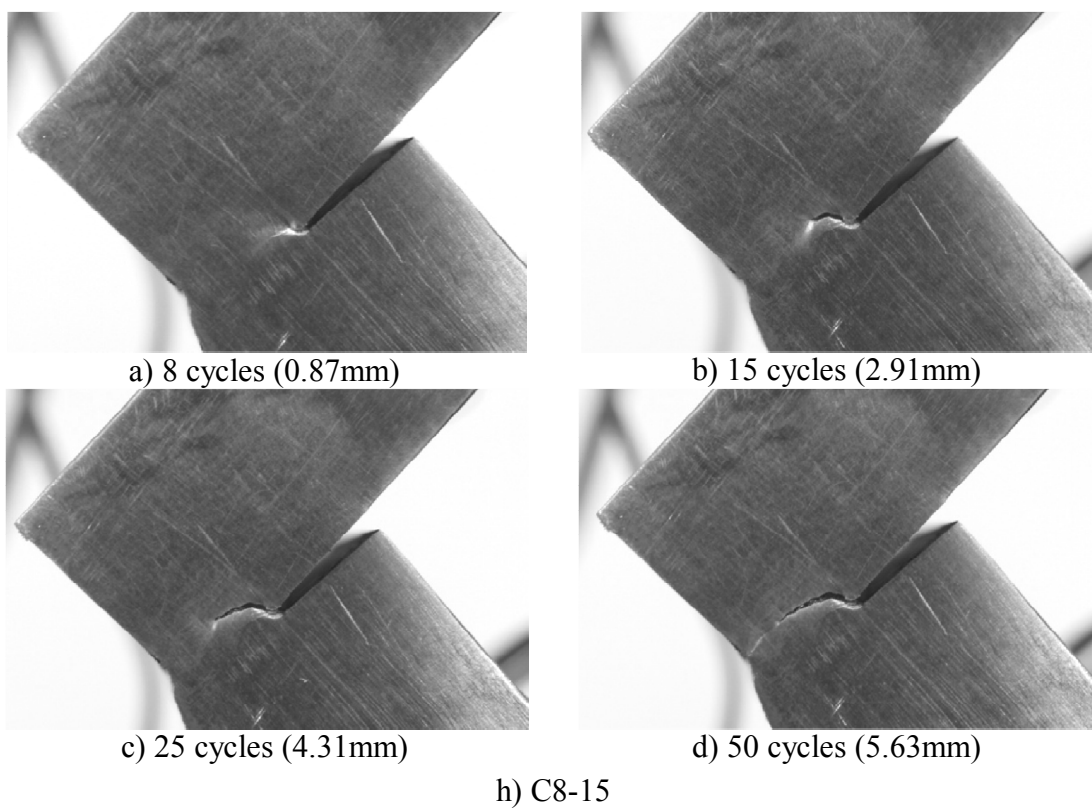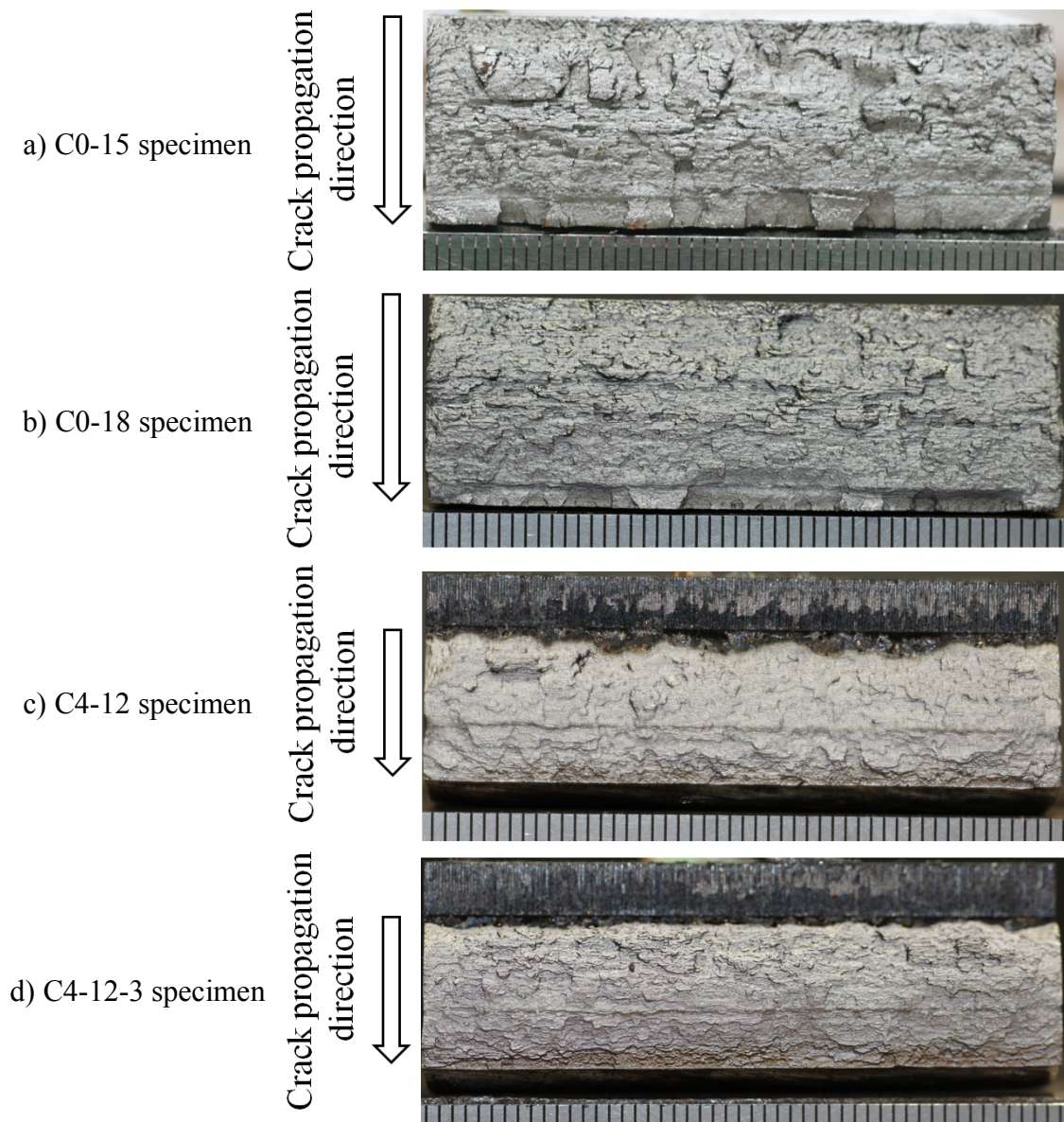d) 35 cycles (6.56mm)

i) C8-18

Fig. B Crack propagation behaviors at the side surface

APPENDIX C: Fracture surfaces

Following figures are fracture surfaces on the small-scale specimens corresponding to **Fig. 3.10** in Chapter 3.
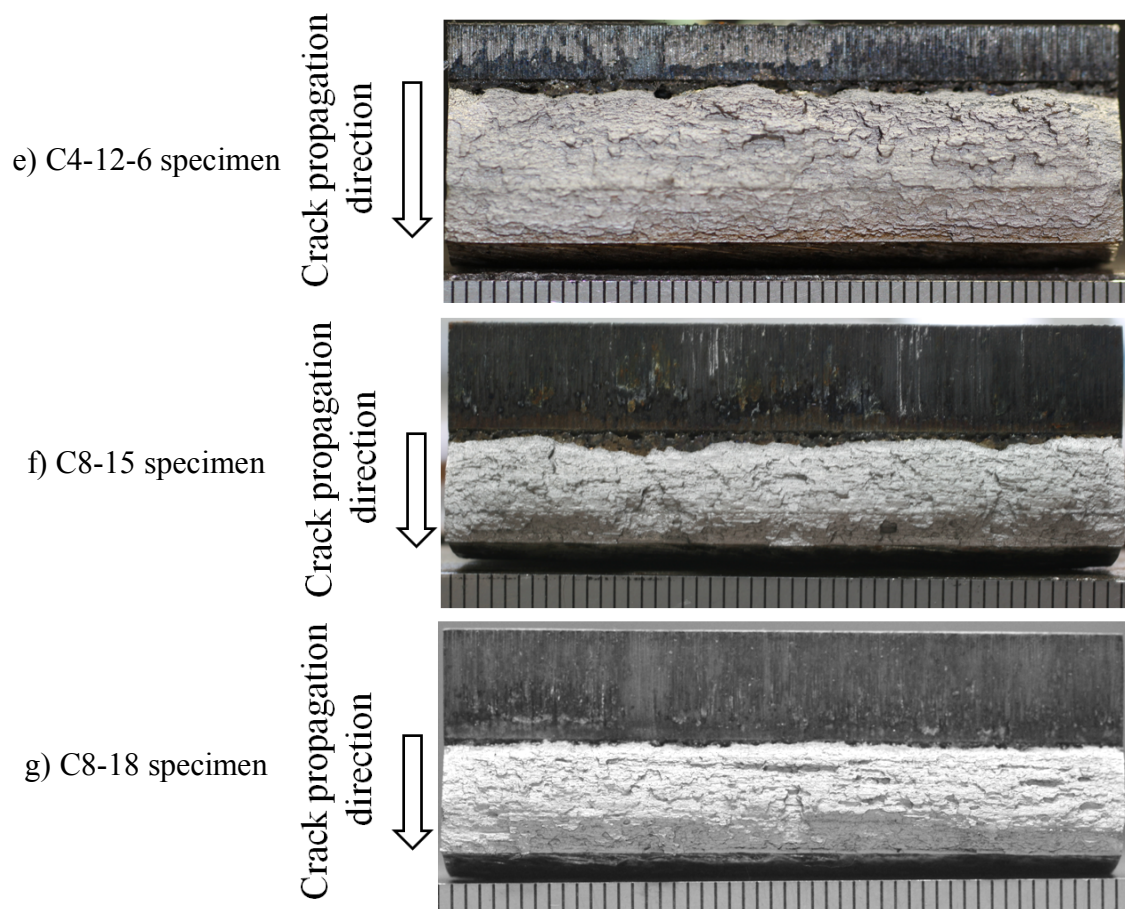

a) C0-15 specimen

b) C0-18 specimen

c) C4-12 specimen

d) C4-12-3 specimen

e) C4-12-6 specimen

Crack propagation direction

f) C8-15 specimen

Crack propagation direction

g) C8-18 specimen

Crack propagation direction

Fig. C Fracture surfaces